



Universiteit Gent
Faculteit Wetenschappen
Vakgroep Fysica en Sterrenkunde

² No title yet

³ No sub-title neither, obviously...

⁴ Alexis Fagot

5



Thesis to obtain the degree of
Doctor of Philosophy in Physics
Academic years 2012-2017





Universiteit Gent
Faculteit Wetenschappen
Vakgroep Fysica en Sterrenkunde

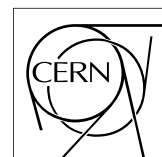
Promotoren: Dr. Michael Tytgat
Prof. Dr. Dirk Ryckbosch

Universiteit Gent
Faculteit Wetenschappen
Vakgroep Fysica en Sterrenkunde
Proeftuinstraat 86, B-9000 Gent, België
Tel.: +32 9 264.65.28
Fax.: +32 9 264.66.97

17



Thesis to obtain the degree of
Doctor of Philosophy in Physics
Academic years 2012-2017



Acknowledgements

¹⁹ Ici on remerciera tous les gens que j'ai pu croiser durant cette aventure et qui m'ont permis de passer
²⁰ un bon moment

²¹ *Gent, ici la super date de la mort qui tue de la fin d'écriture*
²² *Alexis Fagot*

Table of Contents

24	Acknowledgements	i
25	Nederlandse samenvatting	vii
26	English summary	ix
27	1 Introduction	1-1
28	1.1 A story of High Energy Physics	1-1
29	1.2 Organisation of this study	1-1
30	2 Investigating the TeV scale	2-1
31	2.1 The Standard Model of Particle Physics	2-2
32	2.1.1 A history of particle physics	2-2
33	2.1.2 Construction and test of the model	2-11
34	2.1.3 Investigating the TeV scale	2-12
35	2.2 The Large Hadron Collider & the Compact Muon Solenoid	2-14
36	2.2.1 LHC, the most powerful particle accelerator	2-14
37	2.2.1.1 Particle acceleration	2-15
38	2.2.2 CMS, a multipurpose experiment	2-19
39	2.2.3 High Luminosity LHC	2-26
40	2.3 Muon Phase-II Upgrade	2-28
41	2.3.1 Phase-II upgrade of the DT system	2-30
42	2.3.2 Phase-II upgrade of the CSC system	2-30
43	2.3.3 Phase-II upgrade of the RPC system	2-30
44	2.3.4 Phase-II upgrade of the Level-1 trigger	2-31
45	3 Physics of Resistive plate chambers	3-1
46	3.1 Principle	3-1
47	3.1.1 Electron drift velocity	3-4
48	3.2 Rate capability and time resolution of Resistive Plate Chambers	3-4
49	3.2.1 Operation modes	3-4
50	3.2.2 Detector designs and performance	3-6
51	3.2.2.1 Double-gap RPC	3-7
52	3.2.2.2 Multigap RPC (MRPC)	3-8
53	3.2.2.3 Charge distribution and performance limitations	3-9
54	3.3 Signal formation	3-12
55	3.4 Gas transport parameters	3-12

4 Longevity studies and Consolidation of the present CMS RPC subsystem	4-1
4.1 Resistive Plate Chambers at CMS	4-1
4.1.1 Overview	4-1
4.1.2 The present RPC system	4-2
4.1.3 Pulse processing of CMS RPCs	4-3
4.2 Testing detectors under extreme conditions	4-4
4.2.1 The Gamma Irradiation Facilities	4-7
4.2.1.1 GIF	4-7
4.2.1.2 GIF++	4-9
4.3 Preliminary tests at GIF	4-11
4.3.1 Resistive Plate Chamber test setup	4-11
4.3.2 Data Acquisition	4-13
4.3.3 Geometrical acceptance of the setup layout to cosmic muons	4-13
4.3.3.1 Description of the simulation layout	4-14
4.3.3.2 Simulation procedure	4-16
4.3.3.3 Results	4-17
4.3.4 Photon flux at GIF	4-17
4.3.4.1 Expectations from simulations	4-17
4.3.4.2 Dose measurements	4-22
4.3.5 Results and discussions	4-23
4.4 Longevity tests at GIF++	4-24
4.4.1 Description of the Data Acquisition	4-27
4.4.2 RPC current, environmental and operation parameter monitoring	4-28
4.4.3 Measurement procedure	4-29
4.4.4 Longevity studies results	4-29
5 Investigation on high rate RPCs	5-1
5.1 Rate limitations and ageing of RPCs	5-1
5.1.1 Low resistivity electrodes	5-1
5.1.2 Low noise front-end electronics	5-1
5.2 Construction of prototypes	5-1
5.3 Results and discussions	5-1
6 Conclusions and outlooks	6-1
6.1 Conclusions	6-1
6.2 Outlooks	6-1
A A data acquisition software for CAEN VME TDCs	A-1
A.1 GIF++ DAQ file tree	A-1
A.2 Usage of the DAQ	A-2
A.3 Description of the readout setup	A-3
A.4 Data read-out	A-3
A.4.1 V1190A TDCs	A-4
A.4.2 DataReader	A-6
A.4.3 Data quality flag	A-10
A.5 Communications	A-12
A.5.1 V1718 USB Bridge	A-13
A.5.2 Configuration file	A-13
A.5.3 WebDCS/DAQ intercommunication	A-17
A.5.4 Example of inter-process communication cycle	A-18

103	A.6 Software export	A-18
104	B Details on the offline analysis package	B-1
105	B.1 GIF++ Offline Analysis file tree	B-1
106	B.2 Usage of the Offline Analysis	B-2
107	B.2.1 Output of the offline tool	B-3
108	B.2.1.1 ROOT file	B-3
109	B.2.1.2 CSV files	B-5
110	B.3 Analysis inputs and information handling	B-6
111	B.3.1 Dimensions file and IniFile parser	B-6
112	B.3.2 TDC to RPC link file and Mapping	B-7
113	B.4 Description of GIF++ setup within the Offline Analysis tool	B-9
114	B.4.1 RPC objects	B-9
115	B.4.2 Trolley objects	B-10
116	B.4.3 Infrastructure object	B-11
117	B.5 Handeling of data	B-12
118	B.5.1 RPC hits	B-13
119	B.5.2 Clusters of hits	B-14
120	B.6 DAQ data Analysis	B-15
121	B.6.1 Determination of the run type	B-16
122	B.6.2 Beam time window calculation for efficiency runs	B-17
123	B.6.3 Data loop and histogram filling	B-18
124	B.6.4 Results calculation	B-19
125	B.6.4.1 Rate normalisation	B-19
126	B.6.4.2 Rate and activity	B-21
127	B.6.4.3 Strip masking tool	B-23
128	B.6.4.4 Output CSV files filling	B-25
129	B.7 Current data Analysis	B-29

¹³⁰

Nederlandse samenvatting –Summary in Dutch–

¹³² Le resume en Neerlandais (j'aurais peut-être pu apprendre la langue juste pour ça...).

¹³¹

English summary

¹³⁴ Le meme résume mais en Anglais (on commencera par la hein!).

List of Figures

135

136	2.1	Through the gold foil experiment Rutherford could show that most of the mass of atoms was contained in a positively charged nucleus and could then propose a more accurate atomic model than that of Thomson.	2-3
137	2.2	Figure 2.2a: Meson octet. Figure 2.2b: Baryon octet. Figure 2.2c: Baryon decuplet. .	2-8
138	2.3	2.3 The elementary particles of the Standard Model are showed along with their names and properties. Their interactions with the strong, weak and electromagnetic forces have been explicated using color squares. In the left column, the scalar higgs boson is depicted, while the central is focused on the matter particles, the fermions, and the right on the force carriers, the gauge bosons. The role of the Higgs boson in electroweak symmetry breaking is highlighted, and the corresponding way properties of the various particles differ in the (high-energy) symmetric phase (top) and the (low-energy) broken-symmetry phase (bottom) are showed.	2-11
139	2.4	CERN accelerator complex.	2-15
140	2.5	2.5 Pictures of the different accelerators. From top to bottom: first the LINAC 2 and the <i>Pb</i> source of LINAC 3. Then the Booster and the LEIR. Finally, the PS, the SPS and the LHC.	2-17
141	2.6	2.6 Figure 2.6a: schematics of the LHC cryodipoles. 1: Superconducting Coils, 2: Beam pipe, 3: Heat exchanger Pipe, 4: Helium-II Vessel, 5: Superconducting Bus-bar, 6: Iron Yoke, 7: Non-Magnetic Collars, 8: Vacuum Vessel, 9: Radiation Screen, 10: Thermal Shield, 11: Auxiliary Bus-bar Tube, 12: Instrumentation Feed Throughs, 13: Protection Diode, 14: Quadrupole Bus-bars, 15: Spool Piece Bus-bars. Figure 2.6b: magnetic field and resulting motion force applied on the beam particles. . .	2-18
142	2.7	2.7 Figure 2.7a: picture of the LHC quadrupoles. Figure 2.7b: magnetic fields and resulting focussing force applied on the beam by 2 consecutive quadrupoles.	2-19
143	2.8	2.8 Picture of the CMS barrel. The red outer layer is the muon system hosted into the red iron return yokes. The calorimeters are the blue cylinder inside in magnet solenoid and the tracker is the inner yellow cylinder built around the beam pipe.	2-20
144	2.9	2.9 View of the CMS apparatus and of its different components.	2-20
145	2.10	2.10 Slice showing CMS sub-detectors and how particles interact with them.	2-21
146	2.11	2.11 CMS tracker.	2-21
147	2.12	2.12 Figure 2.12a: picture of the ECAL. Figure 2.12b: picture of the lead tungstate crystals composing the ECAL.	2-22
148	2.13	2.13 CMS hadron calorimeter barrel.	2-22
149	2.14	2.14 A quadrant of the muon system, showing DTs (yellow), RPCs (blue), and CSCs (green).	2-23
150	2.15	2.15 Figure 2.15a: Barrel wheel with its detector rings and return yokes. Figure 2.15b: CSC endcap disk with the 2 CSC stations. The outer station is made of 10 deg detectors while the inner station is made of 20 deg detectors. Figure 2.15c: RPC endcap disk. The inner station is not equipped and the inner CSC station can be seen.	2-24
151			
152			
153			
154			
155			
156			
157			
158			
159			
160			
161			
162			
163			
164			
165			
166			
167			
168			
169			
170			
171			
172			
173			
174			

- 175 2.16 Figure 2.16a: Cross section of a DT module showing the two superlayers measur-
 176 ing the ϕ coordinate, perpendicular to the cross section plane, and the superlayer
 177 measuring the η coordinate, placed in between the two others with honeycomb and
 178 parallel to the cross section plane. The DT detector is sandwiched in between 2
 179 RPCs whose readout strips are perpendicular to the cross section plane, measuring
 180 the ϕ coordinate. Figure 2.16b: A DT cell is shown together with its electric field.
 181 The path of a muon through a superlayer is shown. 2-24
- 182 2.17 Figure 2.17a: cathode strips and anode wire layout of a CSC panel. Figure 2.17b
 183 avalanche development and charge collection by anode wires and induction on cath-
 184 ode strips inside of a CSC panel. 2-25
- 185 2.18 Muon track reconstruction through the 6 panels of a CMS CSC using the infor-
 186 mation of anode wire groups and cathode strip charge distribution combined with
 187 comparator bits to decide on which half strip the muon is more likely to have passed. 2-25
- 188 2.19 Double gap layout of CMS RPCs. Muons passing through the gas volumes will cre-
 189 ate electron-ions pairs by ionising the gas. this ionisation will immediately translate
 190 into a developing avalanche. 2-26
- 191 2.20 Detailed timeline of for LHC and HL-LHC operation until 2028 and operation pro-
 192 jection until 2038. This timeline only describes the operation plans after LS1. 2-27
- 193 2.21 Absorbed dose in the CMS cavern after an integrated luminosity of 3000 fb. R is the
 194 transverse distance from the beamline and Z is the distance along the beamline from
 195 the Interaction Point at Z=0. 2-28
- 196 2.22 A quadrant of the muon system, showing DTs (yellow), RPCs (blue), and CSCs
 197 (green). The locations of new forward muon detectors for Phase-II are contained
 198 within the dashed box and indicated in red for GEM stations (ME0, GE1/1, and
 199 GE2/1) and dark blue for improved RPC (iRPC) stations (RE3/1 and RE4/1). 2-29
- 200 2.23 RMS of the multiple scattering displacement as a function of muon p_T for the pro-
 201 posed forward muon stations. All of the electromagnetic processes such as bremsstrahlung
 202 and magnetic field effect are included in the simulation. 2-31
- 203 3.1 Different phases of the avalanche development in the RPC gas volume subjected to
 204 a constant electric field E_0 . a) An avalanche is initiated by the primary ionisation
 205 caused by the passage of a charged particle through the gas volume. b) Due to
 206 its growing size, the avalanche starts to locally influence the electric field. c) The
 207 electrons, lighter than the cations reach the anode first. d) The ions reach the cathode.
 208 While the charges have not recombined, the electric field in the small region around
 209 the avalanche stays affected and locally blind the detector. 3-2
- 210 3.2 Efficiency (circles and stars with 30 mV and 100 mV thresholds respectively) and
 211 streamer probability (opened circles) as function of the operating voltage of a 2 mm
 212 single gap HPL RPC flushed with a gas mixture containing (a) 5%, (b) 2%, (c) 1%
 213 and (d) no SF_6 [33]. 3-3
- 214 3.3 Movement of the charge carriers in an RPC. Figure 3.3a: Voltage across an RPC
 215 whose electrode have a relative permittivity of 5 at the moment the tension s applied.
 216 Figure 3.3b: After the charge carriers moved, the electrodes are charged and there
 217 is no voltage drop over the electrodes anymore. The full potential is applied on the
 218 gas gap only. Figure 3.3c: The streamer discharge initiated by a charged particle
 219 transports electrons and cations towards the anode and cathode respectively. 3-5
- 220 3.4 Typical oscilloscope pulses in streamer mode (Figure 3.4a) and avalanche mode(Figure 3.4b).
 221 In the case of streamer mode, the very small avalanche signal is visible. 3-5

222	3.5	Rate capability comparison for the streamer and avalanche mode of operation. An order of magnitude in rate capability for a maximal efficiency drop of 10% is gained by using the avalanche mode over the streamer mode.	3-6
223			
224			
225	3.6	Possible double-gap RPC layouts: a) "standard" 1D double-gap RPC, as used in CMS experiment, where the anodes are facing each other and a 1D read-out plane is sandwiched in between them, b) double read-out double-gap RPC as used in AT- LAS experiment, where the cathodes are facing each other and 2 read-out planes are used on the outer surfaces. This last layout can offer the possibility to use a 2D reconstruction by using orthogonal read-out planes.	3-7
226			
227			
228			
229			
230			
231	3.7	Comparison of performance of CMS double and single gap RPCs using cosmic muons [44]. Figure 3.7a: Comparison of efficiency sigmoids. Figure 3.7b: Volt- age distribution at 95% of maximum efficiency. Figure 3.7c: $\Delta_{10\%}^{90\%}$ distribution. . . .	3-7
232			
233			
234	3.8	Presentation of ALICE MRPC using 250 μm gas gaps, 620 μm outer glass electrodes and 550 μm inner floating electrodes. More details on the labels are given in [45]. . . .	3-8
235			
236	3.9	Particle identification applied to electrons in the STAR experiment. The identifica- tion is performed combining ToF and dE/dx measurements [50].	3-9
237			
238	3.10	Comparison of the detector performance of ALICE ToF MRPC [51] at fixed applied voltage (in blue) and at fixed effective voltage (in red). The effective voltage is kept fixed by increasing the applied voltage accordingly to the current drawn by the detector.	3-9
239			
240			
241	3.11	Ratio between total induced and drifting charge have been simulated for single gap, double-gap and multigap layouts [52]. The total induced charge for a double-gap RPC is a factor 2 higher than for a multigap.	3-10
242			
243			
244	3.12	Charge spectra have been simulated for single gap, double-gap and multigap lay- outs [52]. It appears that when single gap shows a decreasing spectrum, double and multigap layouts exhibit a spectrum whose peak is detached from the origin. The detachment gets stronger as the number of gaps increases.	3-11
245			
246			
247			
248	3.13	The maximal theoretical efficiency is simulated for single gap, double-gap and multi- gap layouts [52] at a constant gap thickness of 2 mm and using an effective Townsend coefficient of 9 mm^{-1}	3-11
249			
250			
251	4.1	Signals from the RPC strips are shaped by the FEE described on Figure 4.1a. Out- put LVDS signals are then read-out by a TDC module connected to a computer or converted into NIM and sent to scalers. Figure 4.1b describes how these converted signals are put in coincidence with the trigger.	4-3
252			
253			
254			
255	4.2	Description of the principle of a CFD. A comparison of threshold triggering (left) and constant fraction triggering (right) is shown in Figure 4.2a. Constant fraction triggering is obtained thanks to zero-crossing technique as explained in Figure 4.2b. The signal arriving at the input of the CFD is split into three components. A first one is delayed and connected to the inverting input of a first comparator. A sec- ond component is connected to the noninverting input of this first comparator. A third component is connected to the noninverting input of another comparator along with a threshold value connected to the inverting input. Finally, the output of both comparators is fed through an AND gate.	4-4
256			
257			
258			
259			
260			
261			
262			
263			
264	4.3	(4.3a) Extrapolation from 2016 data of single hit rate per unit area in the barrel region. (4.3b) Extrapolation from 2016 data of single hit rate per unit area in the endcap region.	4-6
265			
266			
267	4.4	Background Fluka simulation compared to 2016 Data at $L = 10^{34} \text{cm}^{-2} \cdot \text{s}^{-1}$ in the fourth endcap disk region. A mismatch in between simulation and data can be observed. [To be understood.]	4-7
268			
269			

270	4.5	Layout of the test beam zone called X5c GIF at CERN. Photons from the radioactive source produce a sustained high rate of random hits over the whole area. The zone is surrounded by 8 m high and 80 cm thick concrete walls. Access is possible through three entry points. Two access doors for personnel and one large gate for material. A crane allows installation of heavy equipment in the area.	4-8
271			
272			
273			
274			
275	4.6	^{137}Cs decays by β^- emission to the ground state of ^{137}Ba (BR = 5.64%) and via the 662 keV isomeric level of ^{137}Ba (BR = 94.36%) whose half-life is 2.55 min.	4-9
276			
277	4.7	Floor plan of the GIF++ facility. When the facility downstream of the GIF++ takes electron beam, a beam pipe is installed along the beam line (z-axis). The irradiator can be displaced laterally (its center moves from $x = 0.65$ m to 2.15 m), to increase the distance to the beam pipe.	4-9
278			
279			
280			
281	4.8	Simulated unattenuated current of photons in the xz plane (Figure 4.8a) and yz plane (Figure 4.8b) through the source at $x = 0.65$ m and $y = 0$ m. With angular correction filters, the current of 662 keV photons is made uniform in xy planes.	4-10
282			
283			
284	4.9	Description of the RPC setup. Dimensions are given in mm. A tent containing RPCs is placed at 1720 mm from the source container. The source is situated in the center of the container. RE-4-2-BARC-161 chamber is 160 mm inside the tent. This way, the distance between the source and the chambers plan is 2060 mm. Figure 4.9a provides a side view of the setup in the xz plane while Figure 4.9b shows a top view in the yz plane.	4-11
285			
286			
287			
288			
289			
290	4.10	RE-4-2-BARC-161 chamber is inside the tent as described in Figure 4.9. In the top right, the two scintillators used as trigger can be seen. This trigger system has an inclination of 10° relative to horizontal and is placed above half-partition B2 of the RPCs. PMT electronics are shielded thanks to lead blocks placed in order to protect them without stopping photons from going through the scintillators and the chamber.	4-12
291			
292			
293			
294			
295	4.11	Hit distributions over all 3 partitions of RE-4-2-BARC-161 chamber is showed on these plots. Top, middle and bottom figures respectively correspond to partitions A, B, and C. These plots show that some events still occur in other half-partitions than B2, which corresponds to strips 49 to 64, in front of which the trigger is placed, contributing to the inefficiency of detection of cosmic muons. In the case of partitions A and C, the very low amount of data can be interpreted as noise. On the other hand, it is clear that a little portion of muons reach the half-partition B1, corresponding to strips 33 to 48.	4-13
296			
297			
298			
299			
300			
301			
302			
303	4.12	Results are derived from data taken on half-partition B2 only. On the 18 th of June 2014, data has been taken on chamber RE-2-BARC-161 at building 904 (Prevessin Site) with cosmic muons providing us a reference efficiency plateau of $(97.54 \pm 0.15)\%$ represented by a black curve. A similar measurement has been done at GIF on the 21 st of July with the same chamber giving a plateau of $(78.52 \pm 0.94)\%$ represented by a red curve.	4-14
304			
305			
306			
307			
308			
309	4.13	Representation of the layout used for the simulations of the test setup. The RPC is represented as a yellow trapezoid while the two scintillators as blue cuboids looking at the sky. A green plane corresponds to the muon generation plane within the simulation. Figure 4.9a shows a global view of the simulated setup. Figure 4.9b shows a zommed view that allows to see the 2 scintillators as well as the full RPC plane.	4-15
310			
311			
312			
313			
314	4.14	γ flux $F(D)$ is plot using values from table 4.1. As expected, the plot shows similar attenuation behaviours with increasing distance for each absorption factors.	4-18
315			

316	4.15	Figure 4.15a shows the linear approximation fit done via formulae 4.7 on data from table 4.2. Figure 4.15b shows a comparison of this model with the simulated flux using a and b given in figure 4.15a in formulae 4.4 and the reference value $D_0 =$ 50cm and the associated flux for each absorption factor F_0^{ABS} from table 4.1	4-20
320	4.16	Dose measurements has been done in a plane corresponding to the tents front side. This plan is 1900 mm away from the source. As explained in the first chapter, a lens-shaped lead filter provides a uniform photon flux in the vertical plan orthogonal to the beam direction. If the second line of measured fluxes is not taken into account because of lower values due to experimental equipments in the way between the source and the tent, the uniformity of the flux is well showed by the results.	4-22
326	4.17	4-23
327	4.18	Evolution of the maximum efficiency for RE2 (4.18a) and RE4 (4.18b) chambers with increasing extrapolated γ rate per unit area at working point. Both irradiated (blue) and non irradiated (red) chambers are shown.	4-25
330	4.19	Evolution of the working point for RE2 (4.19a) and RE4 (4.19b) with increasing extrapolated γ rate per unit area at working point. Both irradiated (blue) and non irradiated (red) chambers are shown.	4-25
333	4.20	Evolution of the maximum efficiency at HL-LHC conditions, i.e. a background hit rate per unit area of 300 Hz/cm^2 , with increasing integrated charge for RE2 (4.20a) and RE4 (4.20b) detectors. Both irradiated (blue) and non irradiated (red) chambers are shown. The integrated charge for non irradiated detectors is recorded during test beam periods and stays small with respect to the charge accumulated in irradiated chambers.	4-26
339	4.21	Comparison of the efficiency sigmoid before (triangles) and after (circles) irradiation for RE2 (4.21a) and RE4 (4.21b) detectors. Both irradiated (blue) and non irradiated (red) chambers are shown.	4-26
342	4.22	Evolution of the Bakelite resistivity for RE2 (4.22a) and RE4 (4.22b) detectors. Both irradiated (blue) and non irradiated (red) chambers are shown.	4-27
344	4.23	Evolution of the noise rate per unit area for the irradiated chamber RE2-2-BARC-9 only.	4-27
346	A.1	(A.1a) View of the front panel of a V1190A TDC module [58]. (A.1b) View of the front panel of a V1718 Bridge module [59]. (A.1c) View of the front panel of a 6U 6021 VME crate [60].	A-3
349	A.2	Module V1190A <i>Trigger Matching Mode</i> timing diagram [58].	A-4
351	A.3	Structure of the ROOT output file generated by the DAQ. The 5 branches (<code>EventNumber</code> , <code>number_of_hits</code> , <code>Quality_flag</code> , <code>TDC_channel</code> and <code>TDC_TimeStamp</code>) are visible on the left panel of the ROOT browser. On the right panel is visible the histogram cor- responding to the variable <code>nHits</code> . In this specific example, there were approximately 50k events recorded to measure the gamma irradiation rate on the detectors. Each event is stored as a single entry in the <code>TTree</code>	A-10
356	A.4	The effect of the quality flag is explained by presenting the content of <code>TBranch</code> <code>number_of_hits</code> of a data file without <code>Quality_flag</code> in Figure A.4a and the con- tent of the same <code>TBranch</code> for data corresponding to a <code>Quality_flag</code> where all TDCs were labelled as <code>GOOD</code> in Figure A.4b taken with similar conditions. It can be noted that the number of entries in Figure A.4b is slightly lower then in Figure A.4a due to the excluded events.	A-12

362	A.5	Using the same data as previously showed in Figure A.4, the effect of the quality flag is explained by presenting the reconstructed hit multiplicity of a data file without <code>Quality_flag</code> in Figure A.5a and the reconstructed content of the same RPC partition for data corresponding to a <code>Quality_flag</code> where all TDCs were labelled as <code>GOOD</code> in Figure A.5b taken with similar conditions. The artificial high content of bin 0 is completely suppressed.	A-12
363			
364	A.6	WebDCS DAQ scan page. On this page, shifters need to choose the type of scan (Rate, Efficiency or Noise Reference scan), the gamma source configuration at the moment of data taking, the beam configuration, and the trigger mode. These information will be stored in the DAQ ROOT output. Are also given the minimal measurement time and waiting time after ramping up of the detectors is over before starting the data acquisition. Then, the list of HV points to scan and the number of triggers for each run of the scan are given in the table underneath.	A-14
365			
366			
367			
368	B.1	Example of expected hit time distributions in the cases of efficiency (Figure B.1a) and noise/gamma rate per unit area (Figure B.1b) measurements as extracted from the raw ROOT files. The unit along the x-axis corresponds to ns. The fact that "the" muon peak is not well defined in Figure B.1a is due to the contribution of all the RPCs being tested at the same time that don't necessarily have the same signal arrival time. Each individual peak can have an offset with the ones of other detectors. The inconsistancy in the first 100 ns of both time distributions is an artefact of the TDCs and are systematically rejected during the analysis.	B-16
369			
370			
371			
372	B.2	The effect of the quality flag is explained by presenting the reconstructed hit multiplicity of a data file without <code>Quality_flag</code> . The artificial high content of bin 0 is the effect of corrupted data.	B-19
373			
374			
375	B.3	Display of the masking tool page on the webDCS. The window on the left allows the shifter to edit <code>ChannelsMapping.csv</code> . To mask a channel, it only is needed to set the 3rd field corresponding to the strip to mask to 0. It is not necessary for older mapping file formats to add a 1 for each strip that is not masked as the code is versatile and the default behaviour is to consider missing mask fields as active strips. The effect of the mask is directly visible for noisy channels as the corresponding bin turns red. The global effect of masking strips will be an update of the rate value showed on the histogram that will take into consideration the rejected channels.	B-24
376			
377			
378			
379			
380			
381			
382			
383			
384			
385			
386			
387			
388			
389			
390			
391			
392			
393			

List of Tables

394

395	3.1 Properties of the most used electrode materials for RPCs.	3-4
396	4.1 Total photon flux ($E\gamma \leq 662$ keV) with statistical error predicted considering a	
397	^{137}Cs activity of 740 GBq at different values of the distance D to the source along	
398	the x-axis of irradiation field [55].	4-17
399	4.2 Correction factor c is computed thanks to formulae 4.5 taking as reference $D_0 =$	
400	50 cm and the associated flux F_0^{ABS} for each absorption factor available in table 4.1. .	4-19
401	4.3 The data at D_0 in 1997 is taken from [55]. In a second step, using Equations 4.8	
402	and 4.9, the flux at D can be estimated in 1997. Then, taking into account the	
403	attenuation of the source activity, the flux at D can be estimated at the time of the	
404	tests in GIF in 2014. Finally, assuming a sensitivity of the RPC to γ $s = 2 \cdot 10^{-3}$,	
405	an estimation of the hit rate per unit area is obtained.	4-21
406	A.1 Inter-process communication cycles in between the webDCS and the DAQ through	
407	file string signals.	A-19

List of Acronyms

List of Acronyms

A

414 AFL Almost Full Level

B

419 BARC Bhabha Atomic Research Centre
420 BLT Block Transfer
421 BNL Brookhaven National Laboratory
422 BR Branching Ratio

C

427 CAEN Costruzioni Apparecchiature Elettroniche Nucleari S.p.A.
428 CERN European Organization for Nuclear Research
429 CFD Constant Fraction Discriminator
430 CMB Cosmic Microwave Background
431 CMS Compact Muon Solenoid
432 CSC Cathode Strip Chamber

D

437 DAQ Data Acquisition
438 DCS Detector Control Software
439 DQM Data Quality Monitoring
440 DT Drift Tube

E

445	ECAL	electromagnetic calorimeter
446		
447		
448	F	
449		
450	FCC	Future Circular Collider
451	FEE	Front-End Electronics
452	FEB	Front-End Board
453		
454		
455	G	
456		
457	GE-/-	Find a good description
458	GE1/1	Find a good description
459	GE2/1	Find a good description
460	GEANT	GEometry ANd Tracking - a series of software toolkit platforms developed by CERN
461		
462	GEM	Gas Electron Multiplier
463	GIF	Gamma Irradiation Facility
464	GIF++	new Gamma Irradiation Facility
465		
466		
467	H	
468		
469	HCAL	hadron calorimeter
470	HL-LHC	High Luminosity LHC
471	HPL	High-pressure laminate
472	HV	High Voltage
473		
474		
475	I	
476		
477	iRPC	improved RPC
478	IRQ	Interrupt Request
479	ISR	Intersecting Storage Rings
480		
481		
482	L	
483		
484	LEIR	Low Energy Ion Ring
485	LEP	Large Electron-Positron
486	LHC	Large Hadron Collider
487	LS1	First Long Shutdown

488	LS2	Second Long Shutdown
489	LS3	Third Long Shutdown
490	LV	Low Voltage
491	LVDS	Low-Voltage Differential Signaling

492

493

M

495

496	MC	Monte Carlo
497	MCNP	Monte Carlo N-Particle
498	ME-/	Find good description
499	ME0	Find good description
500	MRPC	Multigap RPC

501

502

N

504

505	NIM	Nuclear Instrumentation Module logic signals
-----	-----	--

506

507

P

509

510	PMT	PhotoMultiplier Tube
511	PS	Proton Synchrotron
512	PU	pile-up

513

514

Q

516

517	QCD	Quantum Chromodynamics
518	QED	Quantum Electrodynamics

519

520

R

521

523	RE-/	Find a good description
524	RE2/2	Find a good description
525	RE3/1	Find a good description
526	RE3/2	Find a good description
527	RE4/1	Find a good description
528	RE4/2	Find a good description
529	RE4/3	Find a good description
530	RMS	Root Mean Square

531 ROOT a framework for data processing born at CERN
532 RPC Resistive Plate Chamber

533

534

S

536

537 SC Synchrocyclotron
538 SLAC Stanford Linear Accelerator Center
539 SM Standard Model
540 SPS Super Proton Synchrotron
541 SUSY supersymmetry

542

543

T

544

546 TDC Time-to-Digital Converter
547 TDR Technical Design Report
548 ToF Time-of-flight

549

550

W

551

553 webDCS Web Detector Control System

554

555

Y

556

558 YETS Year End Technical Stop

1

Introduction

559

560

⁵⁶¹ **1.1 A story of High Energy Physics**

⁵⁶² **1.2 Organisation of this study**

2

563

564

Investigating the TeV scale

565 „We may regard the present state of the universe as the effect of the
566 past and the cause of the future. An intellect which at any given mo-
567 ment knew all of the forces that animate nature and the mutual posi-
568 tions of the beings that compose it, if this intellect were vast enough
569 to submit the data to analysis, could condense into a single formula
570 the movement of the greatest bodies of the universe and that of the
571 lightest atom; for such an intellect nothing could be uncertain and
572 the future just like the past would be present before its eyes.”

573

574 - Pierre Simon de Laplace, *A Philosophical Essay on Probabilities*, 1814

Throughout history, physics experiment became more and more powerful in order to investigate finer details of nature and helped understanding the elementary blocks of matter and the fundamental interactions that bond them in the microscopic world. Nowadays, the Standard Model (SM) of particle physics is the most accurate theory designed to explain the behaviour of particles and was able to make very precise predictions that are constantly verified, although some hints of new physics are visible as bricks are still missing to have a global comprehension of the Universe.

To highlight the limits of the SM and test the different alternative theories, ever more powerful machines are needed. This is in this context that the Large Hadron Collider (LHC) has been thought and built to accelerate and collide particles at energies exceeding anything that had been done before. Higher collision energies and high pile-up imply the use of enormous detectors to measure the properties of the interaction products. The Compact Muon Solenoid (CMS) is a multipurpose experiment that have been designed to study the proton-proton collisions of the LHC and give answers on various high energy physics scenari. Nevertheless, the luminosity delivered by the collider will in the future be increased to levels beyond the original plans to improve its discovery potential giving no choice to experiments such as CMS to upgrade their technologies to cope with the increased radiation levels and detection rates.

2.1 The Standard Model of Particle Physics

In this early 21st century it is now widely accepted that matter is made of elementary blocks referred to as *elementary particles*. The physics theory that classifies and describes the best the behaviour and interaction of such elementary particles is the so called Standard Model that formalizes 3 of the 4 fundamental interactions (electromagnetic, weak and strong interactions). It's development took place during the 20th century thanks to a strong collaboration in between the theoretical and experimental physicists.

2.1.1 A history of particle physics

The idea that nature is composed of elementary bricks, called *atomism*, is not contemporary as it was already discussed by Indian or Greek philosophers during antiquity. In Greece, atomism has been rejected by Aristotelianism as the existance of *atoms* would imply the existance of a void that would violate the physical principles of Aristotle philosophy. Aristotelianism has been considered as a reference in the european area until the 15th century and the italian *Rinascimento* where antic text and history started to be more deeply studied. The re-discovery of Platon's philosophy would allow to open the door to alternative theories and give a new approach to natural sciences where experimentation would become central. A new era of knowledge was starting. By the begining of the 17th century, atomism was re-discovered by philosophers and the very first attempt to estimate an *atom* size would be provided by Magnetus in 1646. Although his *atoms* correspond to what would nowadays be called *molecules*, Magnetus achieved feats by calculating that the number of molecules in a grain of incense would be of the order of 10^{18} simply by considering the time necessary to smell it everywhere in a large church after the stick was lit on. It is now known that this number only falls short by 1 order of magnitude.

An alternative philosophy to atomism popularized by Descartes was corpuscularianism. Built on ever divisible corpuscles, contrary to atoms, it's principles would be mainly used by alchemists like Newton who would later develop a corpuscular theory of light. Boyle would combine together ideas of both atomism or corpuscularianism leading to mechanical philosophy. The 18th century have

seen the development of engineering providing philosophical thought experiments with repeatable demonstration and a new point of view to explain the composition of matter and Lavoisier would greatly contribute to chemistry and atomism by publishing in 1789 a list of 33 chemical elements corresponding to what is now called *atoms*. In the early 19th century Dalton would summarize the knowledge on composition of matter and Fraunhofer would invent the spectrometer and discover the spectral lines. The rise of atomic physics, chemistry and mathematical formalism would unravel the different atomic elements and ultimately, the 20th century would see the very first sub-atomic particles.

Discovery of the inner structure of the atom

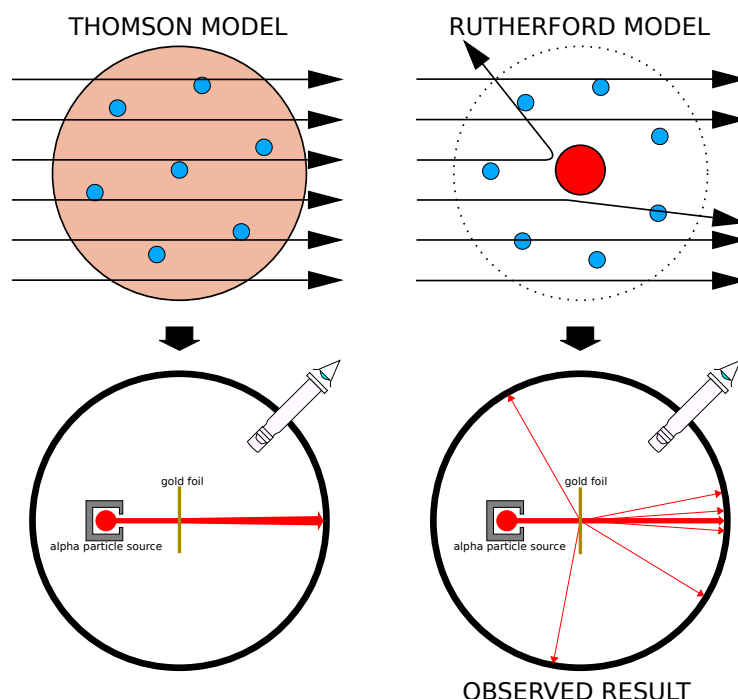


Figure 2.1: Through the gold foil experiment Rutherford could show that most of the mass of atoms was contained in a positively charged nucleus and could then propose a more accurate atomic model than that of Thomson.

The negative *electron* would be the first to be discovered in 1897 by Thomson after 3 decades of research on cathode rays by proving that the electrification observed in an electroscope, as reported by Perrin, was due to the rays themselves and that they had to be composed of electrically charged particles. In 1900, Becquerel would show the *beta rays* emitted by radium had the same charge over mass ratio than what measured by Thomson for cathode rays, pointing to electrons as a constituent of atoms. In 1907, Rutherford and Royds showed that *alpha* particles, once captured in a tube and subjected to an electric spark causing an electron avalanche, where helium ions as they could combine with 2 electrons to form a ${}^4\text{He}$. This discovery was directly followed by the constraint of the atom structure in 1909 through the gold foil experiment in which the deflection angle of alpha particles fired at a very thin gold foil was measured and highlighted atoms where mainly empty with

636 nearly all its mass contained into a tiny positively charged *nucleus*. With these two observations,
 637 he could formulate the Rutherford model of the atom in 1911, shown together with the Thomson
 638 plum pudding model in Figure 2.1. The link in between atomic number and number of positive and
 639 negative charges contained into the atoms would fast be understood and the different kind of element
 640 transmutation appeared to be purely nuclear processes making clear that the electromagnetic nature
 641 of chemical transformation could not possibly change nuclei. Thus a new branch in physics appeared
 642 to study nuclei exclusively: the nuclear physics.

643 Moreover, in 1913 quantum physics would be introduced into the atomic model by Bohr based
 644 on the assumptions of Plank to explain spectral lines, and other observed quantum effects. The same
 645 year, Moseley would confirm Borh's model and Debye would extend it by introducing elliptical
 646 orbits.

647 By studying alpha emission and the product of their interaction with nitrogen gas, Rutherford
 648 reported in 1919 the very first nuclear reaction leading to the discovery that the hydrogen nucleus was
 649 composed of a single positively charged particle that was later baptised *proton*. This idea came from
 650 1815 Prout's hypothesis proposing that all atoms are composed of "*protyles*" (i.e. hydrogen atoms).
 651 By using scintillation detectors, Rutherford could highlight typical hydrogen nuclei signature and
 652 understand that the impact of alpha particles with nitrogen would knock out an hydrogen nucleus
 653 and produce an oxygen 17, as explicated in Formula 2.1 and would then postulate that protons are
 654 building bricks of all elements.



655 With this assumption and the discovery of isotopes together with Aston, elements with identical
 656 atomic number but different masses, Rutherford would propose that all elements' nuclei but hydrogen's are composed of both charged particles, protons, and of chargeless particles, which he called
 657 *neutrons*, and that these neutral particles would help maintaining nuclei as one, as charged protons
 658 were likely to electrostatically repulse each other, and introduced the idea of a new force, a *nuclear*
 659 force. Though the first idea concerning neutrons was a bond state of protons and electrons as it was
 660 known that the beta decay, emitting electrons, was taking place in the nucleus, it was then showed
 661 that such a model would hardly be possible due to Heisenberg's uncertainty principle and by the
 662 recently measured *spin* of both protons and electrons. The spin, discovered through the study of
 663 the emission spectrum of alkali metals, would be understood as a "two-valued quantum degree of
 664 freedom" and formalized by Pauli and extended by Dirac, to take the relativist case into account.
 665 Measured to be $\frac{1}{2}\hbar$ for both, it was impossible to arrange an odd number of half integer spins and
 666 obtain a global nucleus spin that would be integer. Finally, in 1932, following the discovery of a new
 667 neutral radiation, Chadwick could discover the neutron as an uncharged particle with a mass similar
 668 to that of the proton whose half integer spin would reveal to be the solution to explain the nuclear
 669 spin.
 670

671 Development of the Quantum Electrodynamics

672 Historically, the development of the quantum theory revolved around the question of emission and
 673 absorption of discrete amount of energy through light. Einstein used the initial intuition of Plank
 674 about the black-body radiation to develop in 1905 a model to explain the photoelectric effect in
 675 which light was described by discrete quanta now called *photons*. For this model, Einstein introduced
 676 the concept of wave-particle duality as classical theory was not able to describe the phenomenon.
 677 With the new understanding of atoms and of their structure, classical theories also proved unable

678 to explain atoms stability. Indeed, using classical mechanics, electrons orbiting around a nucleus
 679 should radiate an energy proportional to their angular momentum and thus lose energy through
 680 time and the spectrum of energy emission should then be continuous, but it was known since the
 681 19th century and the discovery of spectral lines that the emission spectrum of material was discrete.

682 This was Bohr who first suggested that a quantum description of the atom was necessary in 1913.
 683 Using the correspondence principle stating that at large enough numbers the quantum calculations
 684 should give the same results than the classical theory, he proposed the very first quantum model
 685 of the hydrogen atom explaining the line spectrum by introducing the principal quantum number
 686 n describing the electron shell. This model would then be improved by Sommerfeld that would
 687 quantize the z-component of the angular momentum, leading to the second and third quantum
 688 numbers, or azimuthal and magnetic quantum number, l and m defining for the second the orbital
 689 angular momentum of the electrons on their shells and thus, the shape of the orbital, and for the third
 690 the available orbital on the subshell for each electron. Nevertheless, although the model was not only
 691 limited to spherical orbitals anymore, making the atom more realistic, the Zeeman effect couldn't be
 692 completely explained by just using n , l and m . A solution would be brought after the discovery of
 693 Pauli in 1924, as Uhlenbeck, Goudsmit, and Kramers proposed in 1925 the idea of intrinsic rotation
 694 of the electron, introducing a new angular momentum vector associated to the particle itself, and
 695 not to the orbital, and associated to a new quantic number s , the *spin* projection quantum number
 696 explaining the lift of degeneracy to an even number of energy levels.

697 The introduction of the *spin* happened 1 year after another attempt of improvement of the theory
 698 was made by De Broglie in his PhD thesis. The original formulation of the quantum theory only
 699 considered photons as energy quanta behaving as both waves and particles. De Broglie proposed
 700 that all matter are described by waves and that their momentum is proportional to the oscillation of
 701 quantized electromagnetic field oscillators. This interpretation was able to reproduce the previous
 702 version of the quantum energy levels by showing that the quantum condition involves an integer
 703 multiple of 2π , as shown by Formula 2.2.

$$p = \hbar k \Leftrightarrow \int pdx = \hbar \int kdx = 2\pi\hbar n \quad (2.2)$$

704 Although the intuition of De Broglie about the wave-particle duality of all matter, his interpretation
 705 was semiclassical and it's in 1926 that the first fully quantum mechanical wave-equation would
 706 be introduced by Schrödinger to describe electron-like particles, reproducing the previous semiclassical
 707 formulation without inconsistencies. This complexe equation describes the evolution of the
 708 wave function Ψ of the quantum system, defined by its position vector \mathbf{r} and time t as an energy
 709 conservation law, in which the hamiltonian of the system \hat{H} is explicit, by solving the Equation 2.3.

$$i\hbar \frac{\partial}{\partial t} |\Psi(\mathbf{r}, t)\rangle = \hat{H} |\Psi(\mathbf{r}, t)\rangle \quad (2.3)$$

710 In 1927, Dirac would go further in his paper about emission and absorption of radiation by
 711 proposing a second quantization not only of the physical process at play but also of the electromagnetic
 712 field, providing the ingredients to the first formulation of *Quantum Electrodynamics (QED)*
 713 and the description of photon emission by electrons dropping into a lower energy state in which the
 714 final number of particles is different than the initial one. To complete this model to the many-body
 715 wave functions of identical particles, Jordan included creation and annihilation operators for fields
 716 obeying Fermi-Dirac statistics leading to a model describing particles that would be referred to as
 717 *fermions*. Nevertheless, in order to properly treat electromagnetism, the incorporation of the relativ-

ity theory developed by Einstein. Including gravity into quantum physics still is a challenge nowadays, but in 1928 Pauli and Jordan would show that special relativity's coordinate transformations could be applied to quantum fields as the field commutators were Lorentz invariant. Finally derived the same year, the Dirac equation, shown as Equation 2.4, similarly to Schrödinger's equation, is a single-particle equation but it incorporates special relativity in addition to quantum mechanics rules. It features the 4×4 gamma matrices γ^μ built using 2×2 Pauli matrices and unitary matrix, the 4-gradient ∂_μ , the rest mass m of any half integer spin massive particle described by the wave function $\psi(x, t)$, also called a Dirac spinor, and the speed of light c . In addition to perfectly reproduce the results obtained with quantum mechanics so far, it also provided with *negative-energy solutions* that would later be interpreted as a new form of matter, *antimatter* and give a theoretical justification to the Pauli equation that was phenomenologically constructed to account for the spin as in the non-relativistic limit, the Dirac equation is similar.

$$i\hbar\gamma^\mu\partial_\mu\psi - mc\psi = 0 \quad (2.4)$$

The successes of the QED was soon followed with theoretical problems as computations of any physical process involving photons and charged particles were showed to be only reliable at the first order of perturbation theory. At higher order of the theory, divergent contributions were appearing giving nonsensical results. Only two effects were contributing to these infinities.

- The self-energy of the electron (or positron), the energy that the particle has due its own interaction with its environment.
- The vacuum polarization, virtual electron–positron pairs produced by a background electromagnetic field in the vacuum which is not an "empty" space. These virtual pairs affect the charge and current distributions generated by the original electromagnetic field.

Solving this apparent problem was done by carefully defining the concepts of each observables, for example mass or charge, as these quantities are understood within the context of a non-interacting field equation, and that from the experiment point of view, they are abstractions as what is measured are "renormalized observables" shifted from there "bare" value by the interaction taking place in the measuring process. The infinities needed to be connected to corrections of mass and charge as those are fixed to finite values by experiment. This was the intuition of Bethe in 1947 who successfully computed the effect of such *renormalization* in the non-relativist case. Fully covariant formulations of QED including renormalization was achieved by 1949 by Tomonaga, Schwinger, Feynman and Dyson and Feynman is now famous for his association of diagrams to the term of the scattering matrix, greatly simplifying the representation and computation of interactions as the diagrams directly corresponded the measurable physical processes and would then be used in every quantum field theories. With the resolution of infinities, QED had mostly reached its final form, being still today the most accurate physical theory and would serve as a model to build all other quantum field theories.

Development of the quark model and Quantum Chromodynamics

To explain the nuclear force that holds *nucleons* (protons and neutrons) together, Yukawa theoretically proposed in 1934 the existence of a force carrier called *meson* due to it's predicted mass in the range in between the electron and nucleon masses. Discovered in 1936 by Anderson and Neddermeyer, and confirmed using bubble chambers in 1937 by Street and Stevenson, a first meson

758 candidate was observed in the decay products of cosmic rays. Assuming it had the same electric
 759 charge than electrons and protons, this particle was observed to have a curvature due to magnetic
 760 field that was sharper than protons but smoother than electrons resulting in a mass in between that
 761 of electrons and protons. But its properties were not compatible with Yukawa's theory, which was
 762 emphasized by the discovery of a new candidate in 1947, again in cosmic ray products using photo-
 763 graphic emulsions.

764 This new candidate, although it had a similar mass than the already believed *meson*, would rather
 765 decay into it. For distinction, the first candidate would then be renamed "*mu meson*" when the second
 766 would be the "*pi meson*". The *mu meson* was behaving like a heavy electron and didn't participate
 767 in the strong interaction whereas the pion was believed to be the carrier of the nuclear interaction.
 768 This lead to classify the *mu* in a new category of particles called *leptons* together with the electron
 769 that shared similar properties and *the neutrino*, and be renamed *muon*. The *pi meson* was finally
 770 found to be a triplet of particles: a positively charged, a negatively charged, and a neutral particle.
 771 The neutral *pi meson* has been more difficult to identify as it wouldn't leave tracks on emulsions nor
 772 on bubble chambers and needed to be studied via it's decay products. It was ultimately identified in
 773 University of California's cyclotron in 1950 through the observation of its decay into 2 photons.

774 Also discovered in 1947 but in cloud chamber photographs, the *K meson* as also been an im-
 775 portant step towards the establishment of the Standard Model. A triplet of particle, 2 charged and a
 776 neutral, with a mass roughly half that of a proton, were reported. These particles were baptised *K*
 777 *meson* in contrast to the "light" *pi* and *mu* "L-mesons". The particularity of the *K* were there very
 778 slow decays with a typical lifetime of the order of 10^{-10} s much greater than the 10^{-23} s of *pi*-proton
 779 reactions. The concept of *strangeness*, a new quantum number was then introduced by Pais as an
 780 attempt to explain this phenomenon as *strange* particles appeared as a pair production of a strange
 781 and anti-strange particle.

782 With the development of synchrotrons, the particle *zoo* would grow to several dozens during the
 783 1950s as higher energies were reachable through acceleration. In 1961, a first classification system,
 784 called Eightfold Way, was proposed by Gell-Mann and finding its roots in the Gell-Mann–Nishijima
 785 formula, which relates the electric charge Q , the third component of the isospin I_3 , the *baryon*
 786 number B and the strangeness S , as explicitated in Formula 2.5. The isospin was a quantum number
 787 introduced in 1932 to explain symmetries of the newly discovered neutron using representation
 788 theory of SU(2). The baryon number, was introduced by Nishijima as a quantum number for baryons,
 789 i.e. particles of the same family as nucleons. The mesons were classified in an octet and baryons of
 790 spin $\pm \frac{1}{2}$ and $\pm \frac{3}{2}$ were respectively classified into an octet and a decuplet, as shown in Figure 2.2. To
 791 complete the baryon decuplet, Gell-Mann predicted the existance of baryon Ω^- which would later
 792 be discovered in 1964.

$$Q = I_3 + \frac{1}{2}(B + S) \quad (2.5)$$

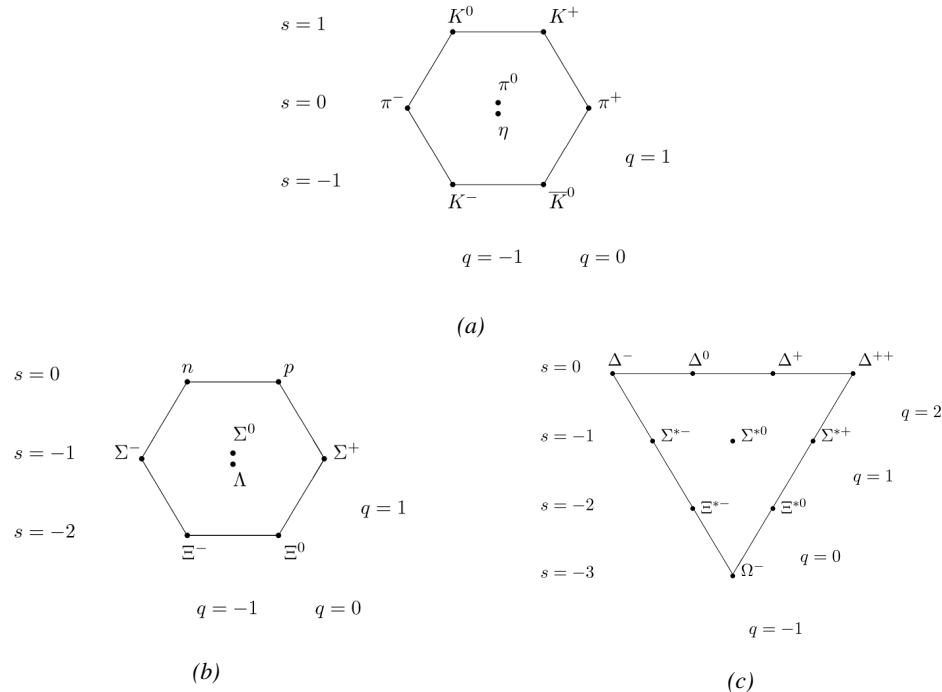


Figure 2.2: Figure 2.2a: Meson octet. Figure 2.2b: Baryon octet. Figure 2.2c: Baryon decuplet.

Strong of this classification using an SU(3) flavor symmetry, Gell-Mann, and independently Zweig, would propose a full theoretical model in which *hadrons* (strongly interacting particles, i.e. mesons and baryons) were not elementary particles anymore. They would rather be composed with 3 flavors of particles called *quarks* and there anti-particles. The 3 flavors were called *up*, *down* and *strange*. *Up* and *down* would be used to explain the nucleons and non-strange mesons, while *strange* would come into the composition of hadrons showing strangeness. *Up* and *down* flavors would be discovered in 1968 thanks to the deep inelastic scattering experiments conducted at the Stanford Linear Accelerator Center (SLAC), and *strange* could only be indirectly validated even though it provided a robust explanation to *kaon* (K) and *pion* (π). However, in the decade following the Gell-Mann-Zweig quark model proposition, several improvement to the model were brought, first by Glashow and Bjorken the same year that predicted the existence of a fourth quark flavor, the *charm*, that would equalize the then known number of quarks and leptons and finally in 1973 by Kobayashi and Maskawa that would increase the number of quarks to 6 to explain the experimental observation of CP violation. These two quarks would be referred to as *top* and *bottom* for the first time in 1975. It's only after these additions to the quark model that finally the *charm* would be discovered in 1974 at both SLAC and Brookhaven National Laboratory (BNL). A meson where the *charm* was bound with an *anti-charm*, called J/ψ , would help convince the physics community of the validity of the model. The *top* would be discovered soon after in 1977 in Fermilab and indicate the existence of the *bottom* that would resist to discovery until Fermilab's experiments CDF and D \emptyset in 1995 due to its very large mass and the energy needed to produce it.

As remarked by Struminsky, the original quark model proposal composed of 3 quarks should possess an additional quantum number due to mesons such as Ω^- or Δ^{++} . Indeed, these mesons are composed of 3 identical quarks, respectively 3 *strange* and *up* quark, with parallel spins, which

should be forbidden by the exclusion principle. Independentle, Greenberg and Han-Nambu proposed an additional SU(3) degree of freedom possessed by the quarks, that would later be refered to as *color charge gauge*, that could interact through *gluons*, the gauge boson octet corresponding to this degree of freedom. Nevertheless, as observing free quarks proved to be impossible, two visions of the quarks were argued mainly due to the failures to observe these particles free to prove their existence. On one side, Gell-Mann proposed to see quarks as mathematical construct instead of real particles, as they are always confined, implying that quantum field theory would not describe entirely the strong interaction. Opposed to this vision, Feynman on the contrary argued that quarks were real particles, that he would call *partons*, that should be described as all other particles by a distribution of position and momentum. The implications of quarks as point-like particles would be verified at SLAC and the concept of *color* would be added to the quark model in 1973 by Fritzsch and Leutwyler together with Gell-Mann to propose a description of the strong interaction through the theory of Quantum Chromodynamics (QCD). The discovery the same year of asymptotic freedom within the QCD by Groos, Politzer and Wilczek, allowed for very precise predictions thanks to the perturbation theory. Nowadays, the confinement of quarks is studied in experiments such as ALICE, through exploration of the quark-gluon plasma.

The Weak interaction, spontaneous symmetry breaking, the Higgs mechanism and the Electroweak unification

The weak interaction is the process that causes radioactive decays. Thanks to the neutron discovery, Fermi could explain in 1934 the beta radiations through the beta decay process in which the neutron decays into a proton by emitting an electron. Though the missing energy observed during this process triggered a huge debate about the apparent non conservation of energy, momentum and spin of the process, Fermi, as Pauli before him, proposed that the missing energy was due to a neutral not yet discovered particle that would then be baptised *neutrino*. The impossibility to detect such a particle would leave some members of the scientific community sceptical, but hints of energy conservation and of the existence of the neutrino were provided by measuring the energy spectrum of electrons emitted through beta decay, as there was a strict limit on their energy. It's only 30 years later in 1953 that it would be discovered by the team of Cowan and Reines using the principle of inverse beta decay described through Formula 2.6. The experiment consisted in placing water tanks sandwiched in between liquid scintillators near a nuclear reactor with an estimated neutrino flux of $5 \times 10^{13} \text{ s}^{-1} \text{ cm}^{-2}$. However, in order to explain the absence of some reactions in the experiment of Cowan and Reines, and constraint the beta decay theory of Fermi and extend it to the case of the muon, Konopinski and Mahmoud proposed in 1953 that the muon decay would eject a particle similar to the neutrino and thus predicted the existence of a muon neutrino that would be different than the one involved in the beta decay, related to the electron. With this, the idea of lepton number would arise. The muon neutrino would successfully be detected in 1962 by Lederman, Schwartz and Steinberger.

$$\bar{\nu} + p \rightarrow n + e^+ \quad (2.6)$$

The theory could not be valid though as the probability of interaction, called cross-section, would have been increasing without bond with the square of the energy. Fermi assumed in a two vector current coupling but Lee and Yang noted that an axial current could appear and would violate parity. The experiment of Wu in 1956 would confirm the parity violation and Gamow and Teller would try to account for it by describing Fermi's interaction through allowed (parity-violating) and superallowed

858 (parity-conserving) decays. But the success of QED as a quantum field theory would spark the
859 development of such a theory to describe the weak interaction.

860 As previously discussed, the great success of QED was built on an underlying symmetry, interpreted
861 as a gauge invariance so that the effect of the force is the same in all space-time coordinates,
862 and of the possibility to renormalize it in order to absorb the infinities. Independently in 1958,
863 Glashow, and Salam and Ward used 1957 Schwinger ideas about vector intermediary for the decay
864 processes, could find a way to unite both the electromagnetic and weak interaction into a gauge
865 theory involving 4 gauge bosons, 3 of which were massive and carried out the weak interaction and
866 a massless boson carrying the electromagnetic interaction. Among the 3 massive bosons, 2 were
867 charged and 1 was neutral, similarly to the previously theorized *pi meson* vector of the Yukawa
868 model and all have a mass much greater than nucleons and thus a very short life time implying a
869 finite very short range contrary to the contact interaction originally proposed by Fermi.

870 Breakthrough in other fields of physics contributed in giving theoretical support and interpretation
871 to the unified electroweak theory. The stepping stone would be the use of spontaneous symmetry
872 breaking that was inspired to Nambu at the end of the 1950s following the development of the BCS
873 superconductivity mechanism in 1957. Cooper had shown that BCS pairs, pairs of electrons bound
874 together at low temperature, could have lower energy than the Fermi energy and where responsible
875 for superconductivity. This lead to the discovery of Goldstone-Nambu bosons as a result of the
876 spontaneous breaking of the chiral symmetry in a theory describing nucleons and mesons developed
877 by Nambu and Jona-Lasinio in 1961, and now understood as a low-energy approximation of
878 QCD. Similarly to mechanism of energy gap appearance in superconductivity, the nucleon mass
879 is suggested to the result of a self-energy of a fermion field and is studied through a four-fermion
880 interaction in which, as a consequence of the symmetry, bound states of nucleon-antinucleon pairs
881 appear and can be regarded as virtual pions. Though the symmetry is maintained in the equations,
882 the ground state is not preserved. Goldstone would later the same year show that the bound states
883 corresponds to spinless bosons with zero mass.

884 Although the model in itself didn't revolutionize particle physics, spontaneous symmetry breaking
885 would be generalized to quantum field theories. As all fundamental interactions are described
886 using gauge theories based on underlying symmetries, processes such as the chiral symmetry breaking
887 would be introduced soon after the publication of Nambu and Jona-Lasinio. In 1962, Anderson,
888 following an idea of Schwinger who suggested that zero-mass vector bosons were not necessarily
889 required to describe the conservation of baryons contrary to the bosons emerging from chiral symmetry
890 breaking, discussed the implications of spontaneous symmetry breaking in particles physics.
891 A model was finally independently built in 1964 by Brout and Englert, Higgs, and Guralnik, Hagen,
892 and Kibble, who discovered that combining an additional field into a gauge theory in order to break
893 the symmetry, the resulting gauge bosons acquire a nonzero mass. Moreover, Higgs stated that this
894 implied the existence of at least one new massive, i.e. self-interacting, scalar boson, that are now
895 known as *Higgs bosons* corresponding to this additional field. The Higgs mechanism today specifically
896 refers to the process through which the gauge bosons of the weak interaction acquire mass. In
897 1968, Weinberg could point to the Higgs mechanism to integrate a Higgs field into a new version
898 of the electroweak theory in which the spontaneous symmetry breaking mechanism of the Higgs
899 field would explicitly explain the masses of the weak interaction gauge bosons and the zero-mass
900 of photons.

2.1.2 Construction and test of the model

The Standard Model of particle physics was built in the middle of the 1970s after the experimental confirmation of the existence of quarks. It is based on the assembly of the models previously introduced and describing the fundamental interactions, except for gravitation, and their gauge bosons as well as the way elementary "matter" particles interact with the fields associated with these force carriers. In this sense, the development of QED and the unification of the electroweak interaction, of the Yukawa interaction and of QCD, and of the Higgs mechanism made it possible to explain most of contemporary physics.

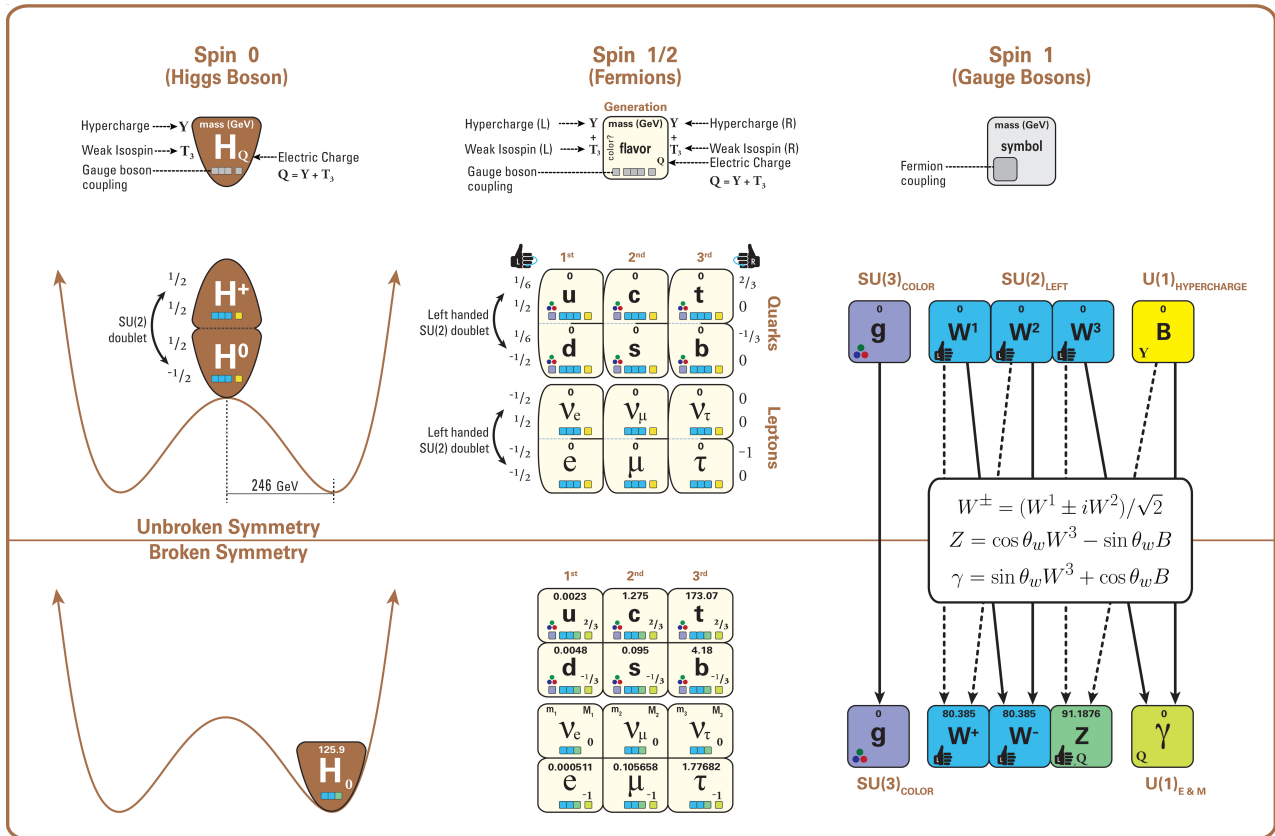


Figure 2.3: The elementary particles of the Standard Model are showed along with their names and properties. Their interactions with the strong, weak and electromagnetic forces have been explicited using color squares. In the left column, the scalar higgs boson is depicted, while the central is focused on the matter particles, the fermions, and the right on the force carriers, the gauge bosons. The role of the Higgs boson in electroweak symmetry breaking is highlighted, and the corresponding way properties of the various particles differ in the (high-energy) symmetric phase (top) and the (low-energy) broken-symmetry phase (bottom) are showed.

In the SM, "matter" particles, are described by 12 fermion fields of spin $\frac{1}{2}$ obeying the Fermi-Dirac statistics, i.e. subjected to the Pauli exclusion principle. To each fermion is associated its corresponding antiparticle. The fermions are classified according to the way they interact and, thus, according to the charges they carry. 6 of them are classified as quarks (u , d , c , s , t , and b) and are subjected to all interactions and the 6 others as leptons (e^- , μ^- , τ^- , ν_e , ν_μ , and ν_τ). Leptons

914 are not subjected to the strong interaction and among them, the 3 neutrinos only interact weakly as
 915 they are neutral particles, which explains why they are so difficult to detect. The gauge boson fields
 916 are the gluons g for the strong interaction, the photon γ for the electromagnetic interaction and the
 917 weak bosons W^+ , W^- , and Z^0 for the weak interaction. Finally, the Higgs field H^0 is responsible,
 918 through the spontaneous symmetry breaking, of the mixing of the massless electroweak boson fields
 919 W_1 , W_2 , W_3 , and B leading to the observable states γ , W^+ , W^- , and Z^0 that can gain mass while
 920 interacting with the Higgs field. This picture of the SM is summarized through Figure 2.3 where the
 921 antifermions are not showed.

922 When the model was first finalized, the existence of the weak gauge bosons, of the charm, of the
 923 third quark generation composed of top and bottom quarks to explain the observed CP violation was
 924 not proven but the predictions were measured with good precision in the years following. First, the
 925 charm quark would be discovered in 1974, followed by the bottom quark in 1977. The weak bosons
 926 would be discovered during the next decade in 1983. The top quark would resist until 1995 due to
 927 its very large mass but would offer the last piece of the elementary QCD particles. The very last
 928 predicted elementary particle of the model that was not observed yet would prove to be very difficult
 929 to observe. the Higgs boson needed the start of the LHC to finally be observed in 2012. A few years
 930 more of tests were necessary to measure its properties to confirm the observation of a scalar boson
 931 compatible with the predicted Higgs boson H^0 . Eventhough only quark-antiquark (mesons) and 3
 932 quark states (baryons) were observed, exotic hadrons were not forbidden by QCD and no limit of
 933 quark is imposed by the theory. Moreover, gluons could form bond states by themselves and with
 934 quarks. These two types of states are called *glueballs* and *hybrid hadrons*. For decades, experi-
 935 ments have been conducted without confirmation of such possible states existing. Nevertheless, in
 936 2014, tetraquarks were observed by LHCb, one of LHC's main experiments, and in 2015, the same
 937 experiment reported the discovery of pentaquarks making the SM one of the best tested theories of
 938 physics.

939 2.1.3 Investigating the TeV scale

940 Even though the SM is a well tested theory, several hints of physics going beyond its scope have
 941 been observed. First of all, gravity is not explained through this model and huge difficulties are en-
 942 countered when trying to include gravitation. The strength of gravitational interaction is expected to
 943 be negligible at the scale of elementary particles, nevertheless, adding gravitation in the perspective
 944 of developing a "theory of everything" leads to divergent integrals that could not be fixed through
 945 renormalization.

946 Moreover, the SM considers neutrinos to be massless but it was shown in the late 1960s by the
 947 Homestake experiment that the flux of solar neutrinos (i.e. ν_e) measured didn't match the predicted
 948 values due to neutrino oscillations, confirmed in the early 2000s by the Sudbury Neutrino Obser-
 949 vatory. This oscillation implies that neutrinos that can be observed are a superposition of massive
 950 neutrino states. The research on neutrino oscillation is already quite advanced with experiments
 951 looking at atmospheric, reactor or beam neutrinos in order to determine the elements of the mixing
 952 matrix similar to the CKM matrix describing the mixing of quarks. Nevertheless, no answer to the
 953 origin of neutrino mass is provided.

954 Another intriguing fact is that the universe is dominated by matter. However, the SM predicted
 955 that matter and antimatter should have been created in equal amounts and no mechanism is able to
 956 explain this matter-antimatter asymmetry. Although this asymmetry is seen from the visible uni-
 957 verse, it may be possible that other unknown regions of the Universe are dominated by antimatter.

958 Another possibility to explain the apparent asymmetry would be the existence of a electric dipole
959 in any fundamental particle that would permit matter and antimatter particles to decay at different
960 rates.

961 The discrepancy of velocity dispersion of stars in galaxies with respect to the visible mass they
962 contain is known since the end of the 19th century where Kelvin proposed that this problem could
963 be solved if a "*great majority of [the stars] would be dark bodies*". Throughout the 20th century,
964 physicists like Kapteyn, Zwicky, showed the first hints of a "*dark matter*" by studying star veloc-
965 ities and galactic clusters, followed by robust measurements of galaxy rotation curves by Babcock
966 which suggested that the mass-to-luminosity ratio was different from what would be expected from
967 watching the visible light. Later in the 1970s, Rubin and Ford from direct light observations and
968 Rogstad and Shostak from radio measurements showed that the radial velocity of visible objects in
969 galaxies was increasing with increasing distance to the center of the galaxy. Finally observation of
970 lensing effect by galaxy clusters, temperature distribution of hot gas in galaxies and clusters, and
971 the anisotropies in the Cosmic Microwave Background (CMB) kept on pointing to a "*dark matter*".
972 From all the data accumulated, the visible matter would only account to no more than 5% of the total
973 content on the visible universe. Alternative theories have tried to investigate modified versions of
974 the General Relativity as this theory is only well tested at the scale of the solar system but is not suf-
975 ficiently tested on wider ranges or even theories in which gravitation is not a fundamental force but
976 rather an emergent one, but so far, such theories have difficulties to reproduce all the experimental
977 observations as easily as through dark matter.

978 A possible theory to offer dark matter candidates would be supersymmetry (SUSY) which pro-
979 poses a relationship in between bosons and fermions. In this model, each elementary particle,
980 through a spontaneous spacetime symmetry breaking mechanism would have a *super partner* from
981 the other family of particles. On top of providing heavy dark matter candidates, supersymmetry
982 could also help solving the *Hierarchy problem*, the very large scale difference in between the weak
983 interaction and gravity, although, as mentioned before, in the case gravity is found not to be a funda-
984 mental force, this problem would automatically fade.

985

986 All these different aspects of physics beyond the Standard Model of particle physics and the
987 Standard model itself can be tested through the use of very energetic and intense hadron and ion col-
988 liders. The LHC at CERN is a perfect tool to seek answers to these open questions except maybe for
989 the gravity as gravity is extremely weak at particles level. For example, one of LHCb experiment's
990 goal is to investigate CP-violation and thus baryonic asymmetry. In 2017, the collaboration has an-
991 nounced to have so far a 3.3σ statistical significance over a CP-violation through the study of the
992 decays of Λ_b^0 and $\overline{\Lambda}_b^0$ into a proton (or antiproton) and 3 pions. Many analysis teams are also working
993 hard on supersymmetry both in ATLAS and CMS collaborations, the two multipurpose experiments
994 of LHC, even though no evidence of a supersymmetrical theory was seen, the few hint having the
995 tendency to confirm the standard model. These experiments also have the possibility to investigate
996 ways to explain Majorana neutrino mass through Yukawa interactions of scalar particles.

997 The higher the center-of-mass energy, the smaller details the experiments will be able to see, the
998 heavier the potential particle creation barrier will be, the stronger the cross-section of certain rare
999 decay channels will be. As a comparison, with collisions happening at 14 TeV, the LHC is approxi-
1000 mately 2 orders of magnitude more sensitive to the Higgs than the Tevatron was with its already very
1001 powerful 2 TeV. All these advantages eventually lead to new discoveries and deeper understanding
1002 of the models describing our Universe. But the LHC only is a step forward to gather more precise
1003 tests of the Standard Model and new knowledge about the physics beyond it. A successful physics

1004 campaign will probably serve to justify the building of new accelerators with even greater discovery
 1005 potential like for example the Future Circular Collider (FCC) that would push even further the study
 1006 of the unanswered questions of contemporary physics.

1007 2.2 The Large Hadron Collider & the Compact Muon Solenoid

1008 Throughout its history, CERN has played a leading role in high energy particle physics. Large re-
 1009 gional facilities such as CERN were thought after the second world war in an attempt to increase
 1010 international scientific collaboration and allows scientists to share the forever increasing costs of
 1011 experiment facilities required due to the need for increasing the energy in the center of mass to
 1012 deeper probe matter. The construction of the first accelerators at the end of the 50s, the Synchro-
 1013 cyclotron (SC) and the Proton Synchrotron (PS), was directly followed by the first observation of
 1014 antinuclei in 1965 [1]. Strong from the experience of the Intersecting Storage Rings (ISR), the very
 1015 first proton-proton collider that showed hints that protons are not elementary particles, the Super
 1016 Proton Synchrotron (SPS) was built in the 70s to investigate the structure of protons, the preference
 1017 for matter over antimatter, the state of matter in the early universe or exotic particles, and lead to
 1018 the discovery in 1983 of the W and Z bosons [2–5]. These newly discovered particles and the elec-
 1019 troweak interaction would then be studied in details by the Large Electron-Positron (LEP) collider
 1020 that will help to prove in 1989 that there only are three generations of elementary particles [6]. The
 1021 LEP would then be dismantled in 2000 to allow for the LHC to be constructed in the existing tunnel.

1022 2.2.1 LHC, the most powerful particle accelerator

1023 The LHC has always been considered as an option to the future of CERN. At the moment of the
 1024 construction of the LEP beneath the border between France and Switzerland, the tunnel was built in
 1025 order to accomodate what would be a Large Hadron Collider with a dipole field of 10 T and a beam
 1026 energy in between 8 and 9 TeV [7] directly followed in 1985 with the creation of a 'Working Group
 1027 on the Scientific and Technological Future of CERN' to investigate such a collider [8]. The decision
 1028 was finally taken almost 10 years later, in 1994, to construct the LHC in the LEP tunnel [9] and the
 1029 approval of the 4 main experiments that would take place at the 4 interaction points would come in
 1030 1997 [10] and 1998 [11]:

- 1031 • ALICE [12] has been designed in the purpose of studying quark-gluon plasma that is believed
 1032 to have been a state of matter that existed in the very first moment of the universe.
- 1033 • ATLAS [13] and CMS [14] are general purpose experiments that have been designed with
 1034 the goal of continuing the exploration of the Standard Model and investigate new physics.
- 1035 • LHCb [15] has been designed to investigate the preference of matter over antimatter in the
 1036 universe through the CP violation.

1037 These large scale experiments, as well as the full CERN accelerator complex, are displayed on
 1038 Figure 2.4. The LHC is a 27 km long hadron collider and the most powerful accelerator used for
 1039 particle physics since 2008 [16]. The LHC was originally designed to collide protons at a center-
 1040 of-mass energy of 14 TeV and luminosity of $10^{34} \text{ cm}^{-2}\text{s}^{-1}$, as well as Pb ions at a center-of-mass
 1041 energy of 2.8 TeV/A with a peak luminosity of $10^{27} \text{ cm}^{-2}\text{s}^{-1}$. Run 1 of LHC, when the center-of-
 1042 mass energy only was half of the nominal LHC energy, was enough for both CMS and ATLAS to

discover the Higgs boson [17] and for LHCb to discover pentaquarks [18] and confirm the existance of tetraquarks [19]. Nevertheless, after the Third Long Shutdown (LS3) (2024-2026), the accelerator will be in the so called High Luminosity LHC (HL-LHC) configuration [20], increasing its instantaneous luminosity to $10^{35} \text{ cm}^{-2}\text{s}^{-1}$ for pp collisions and to $4.5 \times 10^{27} \text{ cm}^{-2}\text{s}^{-1}$, boosting the discovery potential of the LHC. The HL-LHC phase should last at least another 10 years depending on the breakthrough this machine would lead to. Already a new accelerating device, the FCC, as been proposed to prepare the future of high energy physics after the LHC.

CERN's Accelerator Complex

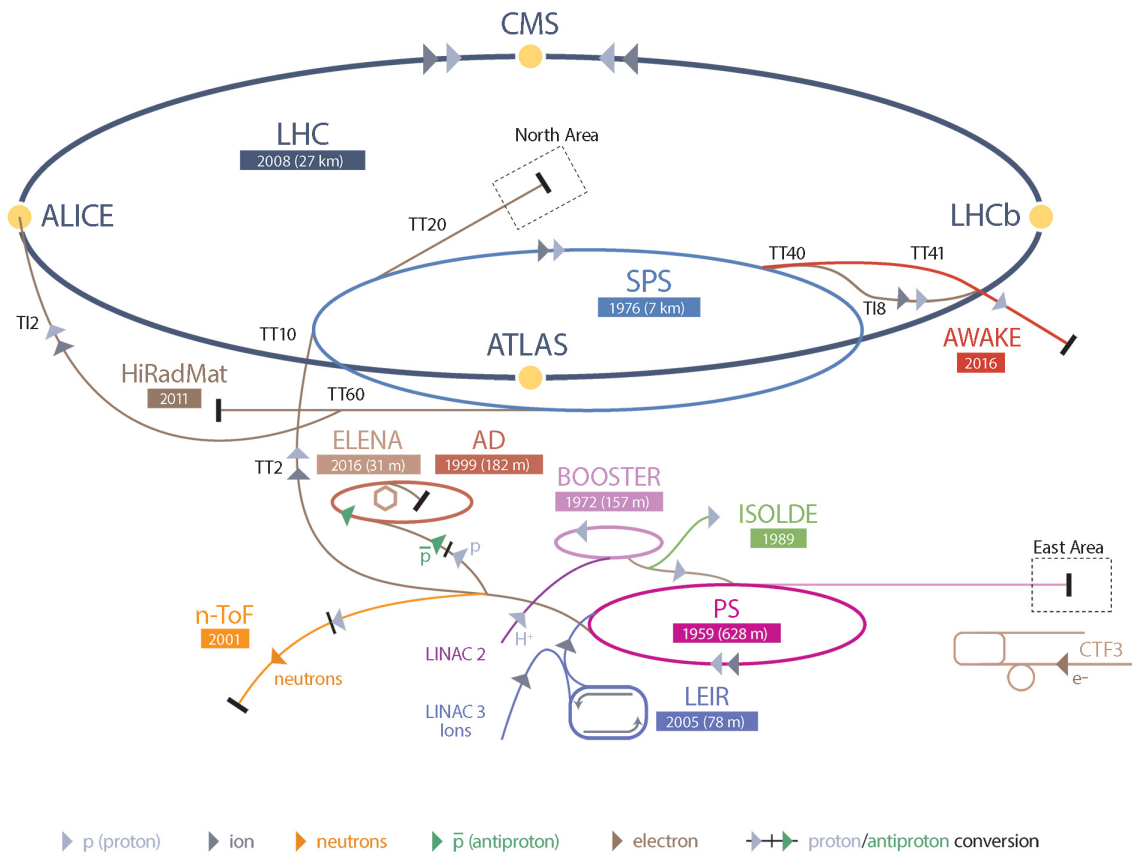


Figure 2.4: CERN accelerator complex.

2.2.1.1 Particle acceleration

The LHC is the last of a long series of accelerating devices. Before being accelerated by the LHC, the particles need to pass through different acceleration stages. All these acceleration stages are visible on Figure 2.4 and pictures of the accelerators are showed in Figure 2.5.

The story of accelerated protons at CERN starts with a bottle of hydrogen gas injected into the source chamber of the linear particle accelerator *LINAC 2* in which a strong electric field strips the

1057 electron off the hydrogen molecules only to keep their nuclei, the protons. The cylindrical conductors,
1058 alternatively positively or negatively charged by radiofrequency cavities, accelerate protons by
1059 pushing them from behind and pulling them from the front and ultimately give them an energy of
1060 50 MeV, increasing their mass by 5% in the process.

1061

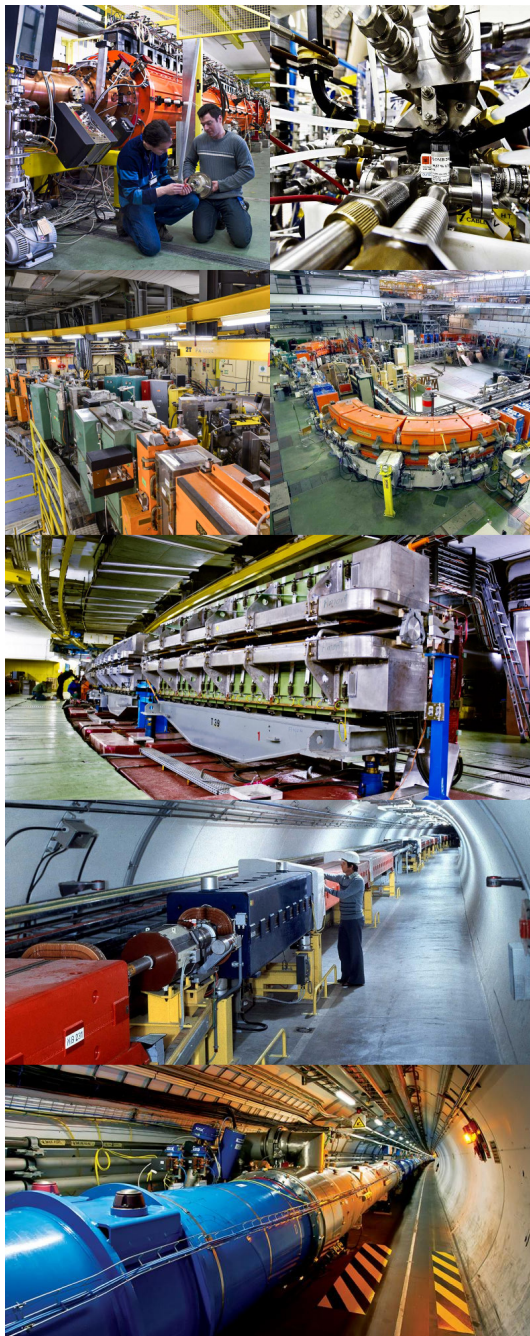


Figure 2.5: Pictures of the different accelerators. From top to bottom: first the LINAC 2 and the Pb source of LINAC 3. Then the Booster and the LEIR. Finally, the PS, the SPS and the LHC.

When exiting the LINAC 2, the protons are divided into 4 bunches and injected into the 4 superimposed synchrotron rings of the *Booster* where they are then accelerated to reach an energy of 1.4 GeV before being injected into the *PS*. Before the Booster was operational in 1972, the protons were directly injected into the *PS* from the LINAC 2 but the low injection energy limited the amount

of protons that could be accelerated at once by the PS. With the Booster, the PS accepts approximately 100 times more particles.

1068

The 4 proton bunches are thus sent as one to the PS where their energy eventually reaches 26 GeV. Since the 70s, the main goal of this 628 m circumference synchrotron has been to supply other machines with accelerated particles. Nowadays, not only the PS accelerates protons, it also accelerates heavy ions from the *Low Energy Ion Ring (LEIR)*. Indeed, the LHC experiments are not only designed to study *pp*-collisions but also *Pb*-collisions. Lead is first injected into the dedicated linear collider *LINAC 3*, that accelerates the ions using the same principle than *LINAC 2*. Electrons are stripped off the lead ions all along the acceleration process and eventually, only bare nuclei are injected in the LEIR whose goal is to transform the long ion pulses received into short dense bunches for LHC. Ions injected and stored in the PS were accelerated by the LEIR from 4.2 MeV to 72 MeV.

1078

Directly following the PS, is finally the last acceleration stage before the LHC, the 7 km long *SPS*. The SPS accelerates the protons to 450 GeV and inject proton in both LHC accelerator rings that will increase their energy up to 7 TeV. When the LHC runs with heavy lead ions for ALICE and LHCb, ions are injected and accelerated to reach the energy of 2.8 TeV/A.

1083

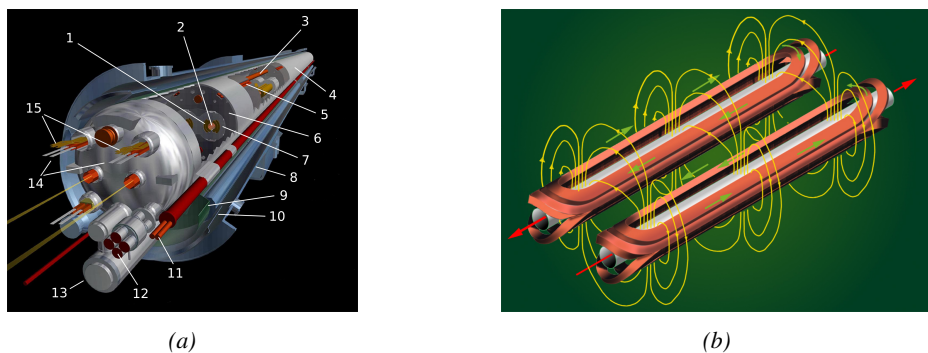


Figure 2.6: Figure 2.6a: schematics of the LHC cryodipoles. 1: Superconducting Coils, 2: Beam pipe, 3: Heat exchanger Pipe, 4: Helium-II Vessel, 5: Superconducting Bus-bar, 6: Iron Yoke, 7: Non-Magnetic Collars, 8: Vacuum Vessel, 9: Radiation Screen, 10: Thermal Shield, 11: Auxiliary Bus-bar Tube, 12: Instrumentation Feed Throughs, 13: Protection Diode, 14: Quadrupole Bus-bars, 15: Spool Piece Bus-bars. Figure 2.6b: magnetic field and resulting motion force applied on the beam particles.

1084

The LHC beams are not continuous and are rather organised in bunch of particles. When in *pp*-collision mode, the beams are composed of 2808 bunches of 1.15×10^{11} protons separated by 25 ns. When in *Pb* collision mode, the 592 *Pb* bunches are on the contrary composed of 2.2×10^8 ions separated by 100 ns. The two parallel proton beams of the LHC are contained in a single twin-bore magnet due to the space restriction in the LEP tunnel. Indeed, building 2 completely separate accelerator rings next to each other was impossible. The dipoles of the 1232 twin-bore magnets are showed in Figure 2.6 alongside the magnetic field generated along the dipole section to accelerate the particles. The dipoles generate a nominal field of 8.33 T, needed to give protons and lead nucleons their nominal energy. Some 392 quadrupoles, presented in Figure 2.7, are also used to focus to the beams, as well as other multipoles to correct smaller imperfections.

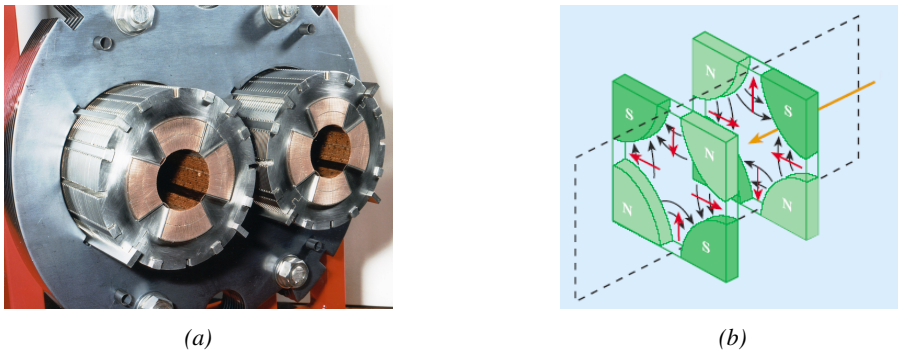


Figure 2.7: Figure 2.7a: picture of the LHC quadrupoles. Figure 2.7b: magnetic fields and resulting focussing force applied on the beam by 2 consecutive quadrupoles.

2.2.2 CMS, a multipurpose experiment

Among the four main LHC experiments is the Compact Muon Solenoid used as a multipurpose tool to investigate the SM and physics beyond its scope. Proposed through a letter of intention in 1992 [14], and as its name suggests, this very compact detector's uses the muons as a clear tag of most of SM and new physics interesting channels. In the original 1997 Technical Design Report (TDR) [21], the very first sentences were stating that "*Muons are an unmistakable signature of most of the physics LHC is designed to explore. The ability to trigger on and reconstruct muons at the highest luminosities is central to the concept of CMS, the Compact Muon Solenoid.*" CMS participated in the discovery of the Higgs boson and the measurement of its properties and couplings together with ATLAS and is also actively involved in the search for SUSY and heavy ion collisions. Other exotic physics are also being investigated using the data collected by CMS.

The CMS apparatus in itself is the heaviest detector ever built starring a 15m diameter and a 29 m length for a total weight of 14 kT. A thick 4 T solenoid magnet located at the beam interaction point hosts trackers and calorimeters. Extending in all directions around the magnet, heavy iron return yokes are installed to extend the magnetic field and support a muon system. The apparatus consists of a barrel, referring to the magnet and the detectors contained in it and the part of the muon system built directly in the cylinder around the magnet, and of 2 endcaps in the forward and backward region of the detector that closes the apparatus and complete the detection coverage along the beam line. A front view on the barrel is provided in Figure 2.8 while a detailed view of the apparatus is given in Figure 2.9.

In order to efficiently detect all long leaving particles and measure their properties with good precision, the CMS detector uses an onion like layout around of the interaction point in order to maximize the covered solid angle. As detailed in Figure 2.10, in the innermost region of the detector, closest to the interaction point, the silicon tracker records the trajectory of charged particles. Around it, the electromagnetic calorimeter (ECAL) stops and measure the energy deposition of electrons and photons. In the next layer, the hadron calorimeter (HCAL), hadrons are stopped and their energy measured. These layers are contained inside of the magnet of CMS, the superconducting solenoid. Outside of the magnet are the muon chambers embedded into iron return yokes used to control the magnetic field and gives muons, the only particles traveling completely through the whole detector, a double bending helping in reconstructing their energy and trajectory. Note that photons and neutral

¹¹²⁵ hadrons are differentiated from electrons and charged hadrons in the calorimeters by the fact that
¹¹²⁶ don't interact with the silicon tracker and that they are not influenced by the magnetic field.

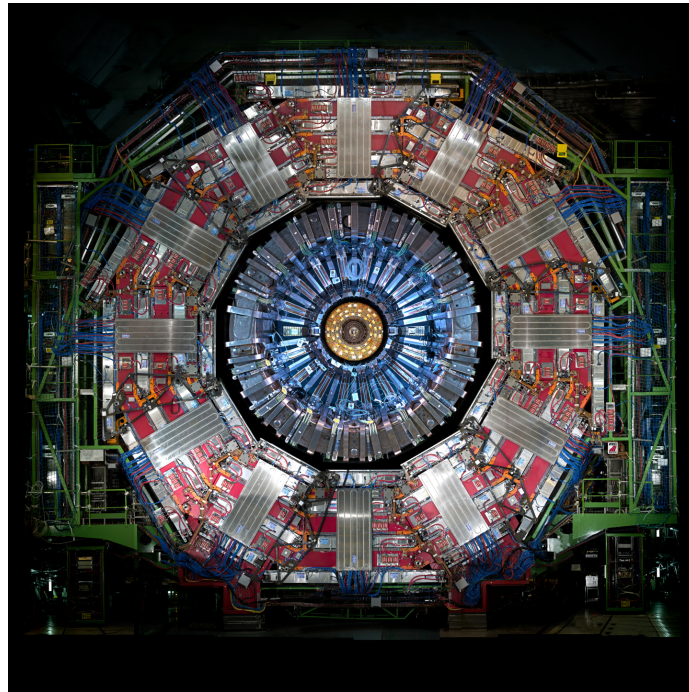


Figure 2.8: Picture of the CMS barrel. The red outer layer is the muon system hosted into the red iron return yokes. The calorimeters are the blue cylinder inside in magnet solenoid and the tracker is the inner yellow cylinder built around the beam pipe.

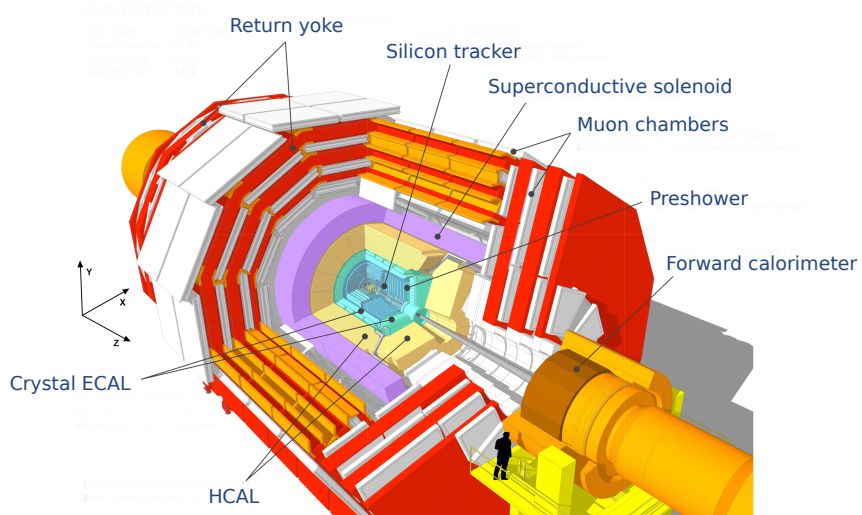


Figure 2.9: View of the CMS apparatus and of its different components.

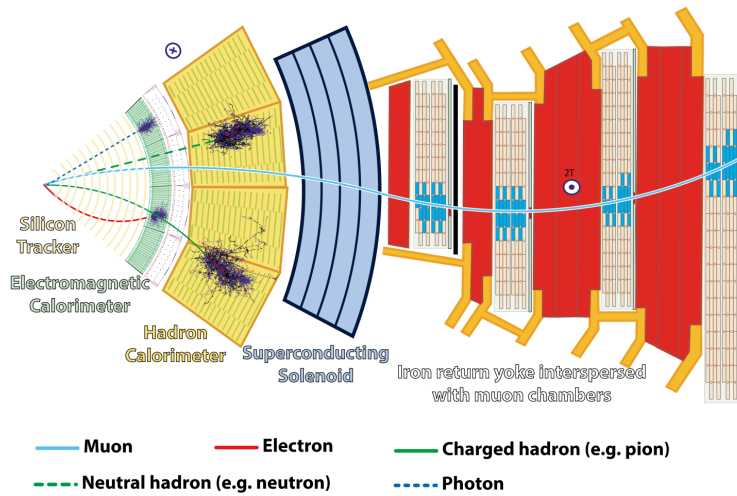


Figure 2.10: Slice showing CMS sub-detectors and how particles interact with them.

1127 The silicon tracker visible on Figure 2.11 is divided into 2 different sub-systems: the *pixel detector* at the very core and the *microstrip detector* around it. This system is composed of 75 million
 1128 individual readout channels with up to 6000 channels per squared centimeter for the pixels making
 1129 it the world's biggest silicon detector. This density allows for measurements of the particle tracks
 1130 with a precision of the order of $10\text{ }\mu\text{m}$. This is necessary to reconstruct all the different interaction
 1131 vertices with precision and have a precise measure of the curvature of the charged particles traveling
 1132 through the magnetic field to estimate their charge and momentum.
 1133

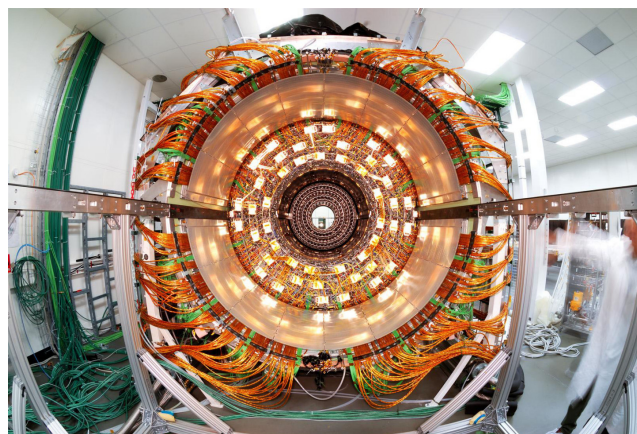


Figure 2.11: CMS tracker.

1134 The ECAL directly surrounding the tracker is composed of crystals of lead tungstate, PbWO_4 , a
 1135 very dense but optically transparent material used to stop high energy electrons and photons. These
 1136 crystal blocks basically are extremely dense scintillators which scintillate in fast, short light bursts
 1137 proportionally to the energy deposition. The light is yielded rapidly and contained at 80% in the
 1138 corresponding 25 ns lasting bunch crossing. Each crystal is isolated from the other by the carbon
 1139 fiber matrix they are embedded in. It is composed of a barrel containing more than 60,000 crystals

and of closing endcaps containing another 15,000 crystals. In front of the ECAL endcap is installed a preshower detector made out of two layers of lead and silicon strip detectors to increase the spatial resolution close to the beam line for pion-photon and single-double photon discrimination purposes. Figure 2.12 shows the calorimeter inside of the magnet and the crystals.

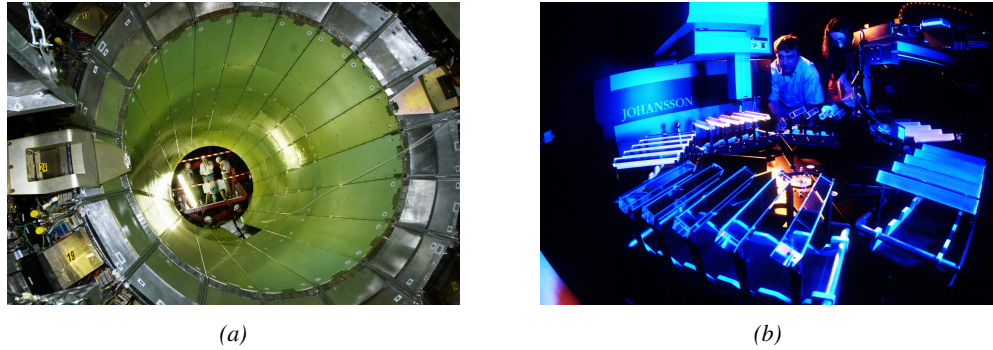


Figure 2.12: Figure 2.12a: picture of the ECAL. Figure 2.12b: picture of the lead tungstate crystals composing the ECAL.

The next layer is the HCAL measuring the hadrons momentum and providing indirect hints of non interacting neutral particles, such as neutrinos, as missing transverse momentum. Several layers of brass or steel are interleaved with plastic scintillators readout by photodiodes using wavelength-shifting fibers. The HCAL is also composed of a barrel, showed in Figure 2.13 and of endcaps. It also features forward calorimeters on both sides of CMS in the region very close to the beam line at high pseudorapidity ($3.0 < |\eta| < 5.0$). The role of these forward calorimeters, made using steel and quartz fibers, is to measure very energetic hadrons.

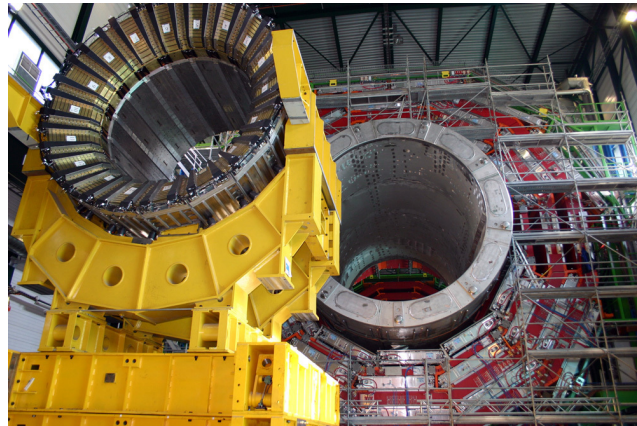


Figure 2.13: CMS hadron calorimeter barrel.

Finally, in the outer region of the apparatus, a muon system is used to trigger on potentially interesting event by identifying muons. Indeed, the muon system is a very important part of the CMS trigger infrastructure designed to efficiently select data from the enormous data flow received by the detectors as the LHC delivers collisions at a rate of 40 MHz with a pile-ip of 20 to 30 collisions per bunch crossing during Phase-I and up to 200 during Phase-II, representing billions of interactions

per second among which a large quantity are low energy collisions that are not likely to produce new reactions, and which is physically impossible for nowadays technologies to cope with. Working at a maximum rate of 100 kHz, the trigger system is able to select the 100,000 more interesting events by looking at the energy distribution of the interaction products and clear signatures like muons reconstructed by the muon system. the vast majority of these events will not finally be stored after physics tests are applied.

The challenge for the muon system is to provide a robust and fast measurement of muons. Three different subsystems, and soon 4 after LS2, compose the muon system as showed in Figure 2.14 in which a quadrant of the CMS detector focused on muon system. Drift Tube (DT) are found in the barrel region covering the low pseudorapidity region where particles transverse momentum is lower and Cathode Strip Chamber (CSC) are found in the endcap region covering higher pseudorapidity region closer to beam line where particles have a stronger momentum. The redundancy of the system is insured by Resistive Plate Chamber (RPC) in both the barrel and endcap region. Nevertheless, the region closest to the beam line ($|\eta| > 1.8$) was not equipped with RPCs. This lack of redundancy in the high pseudo rapidity region will be solved during LS2, the following Year End Technical Stop (YETS) in 2021 and 2022, and LS3 where the necessary services, detectors and Link System, that collects the data and synchronizes them, will be installed.

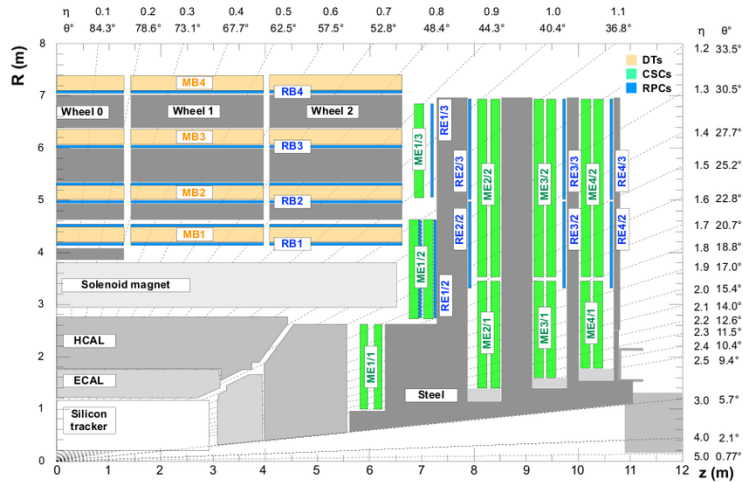


Figure 2.14: A quadrant of the muon system, showing DTs (yellow), RPCs (blue), and CSCs (green).

The barrel region is divided into 5 *wheels* made out of 4 *rings* of detectors with iron return yokes in between them whereas the endcaps are made out of 4 disks, each divided into pseudorapidity stations, 2 for CSCs (except for the first disk where 3 stations are equipped) and 3 for RPCs, although only 2 RPCs stations are equipped at present. The wheels and disks are showed in Figure 2.15. So far, each subsystem was dedicated to a particular task. DTs, in the barrel, and CSCs, in the endcaps, are used mainly for their spatial resolution. Indeed, DTs' resolution is of the order of 100 μm along both the $(r - \phi)$ and $(r - z)$ components while the resolution of CSCs is similar but varies in a range from 50 μm to 140 μm depending on the distance to the beamline. On the other hand, RPCs are used for their time resolution as they can deliver an information on the muon tracks within 1.5 ns.

The 250 CMS DTs, found in the barrel covering the pseudorapidity region $0 < |\eta| < 1.2$ and whose structure is shown in Figure 2.16, are composed of 3 *superlayers* of DT cells. Two of

these superlayers are dedicated to measuring the ϕ coordinate of the muons and while the last one measures the η (or z) coordinate. Each superlayer consists on 4 layers of 60 to 70 DT cells arranged in quincunx to allow for a precise reconstruction of the muon path through the DT layers. Each DT cell is a rectangular aluminium gas volume with a central anode wire. Cathode strips are placed on the narrow surface of the cells and electrode strips are placed on the wide surface to help shaping the electric field to ensure a consistent drift velocity of electrons in the drift volume. These detectors are operated using a 85/15 mixture of Ar and CO_2 .

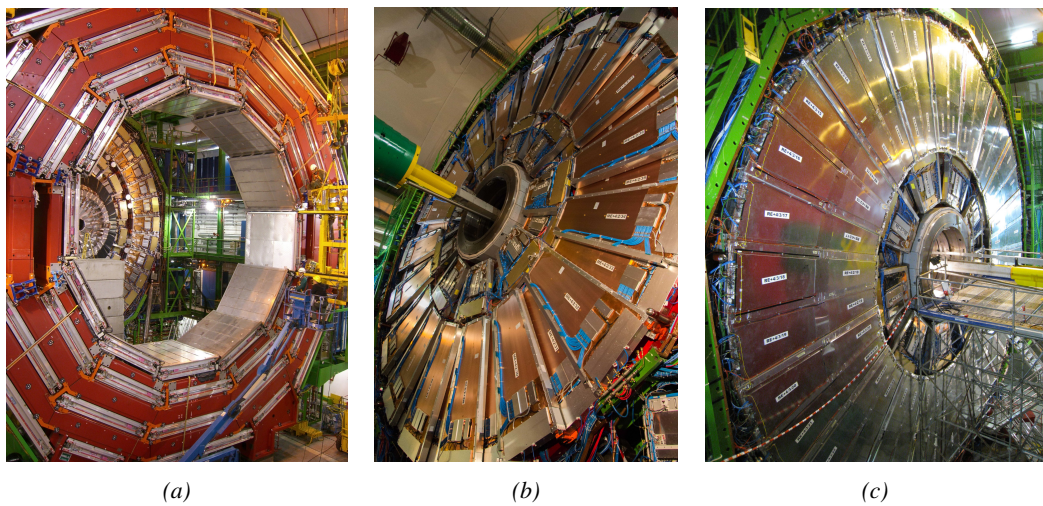


Figure 2.15: Figure 2.15a: Barrel wheel with its detector rings and return yokes. Figure 2.15b: CSC endcap disk with the 2 CSC stations. The outer station is made of 10 deg detectors while the inner station is made of 20 deg detectors. Figure 2.15c: RPC endcap disk. The inner station is not equipped and the inner CSC station can be seen.

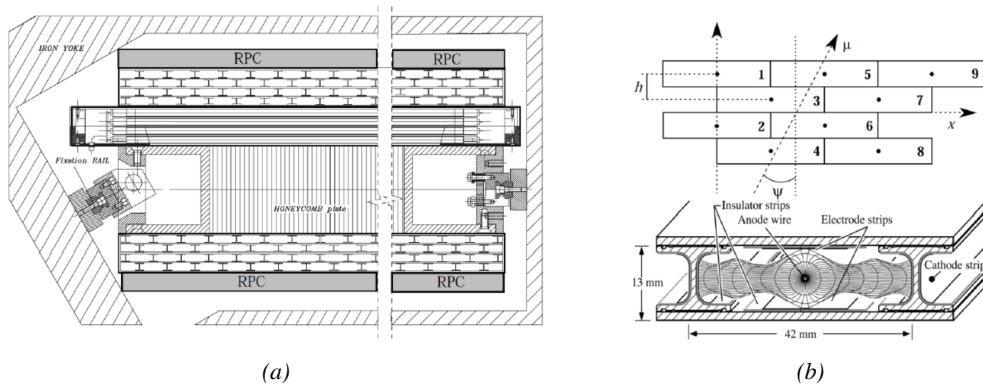


Figure 2.16: Figure 2.16a: Cross section of a DT module showing the two superlayers measuring the ϕ coordinate, perpendicular to the cross section plane, and the superlayer measuring the η coordinate, placed in between the two others with honeycomb and parallel to the cross section plane. The DT detector is sandwiched in between 2 RPCs whose readout strips are perpendicular to the cross section plane, measuring the ϕ coordinate. Figure 2.16b: A DT cell is shown together with its electric field. The path of a muon through a superlayer is shown.

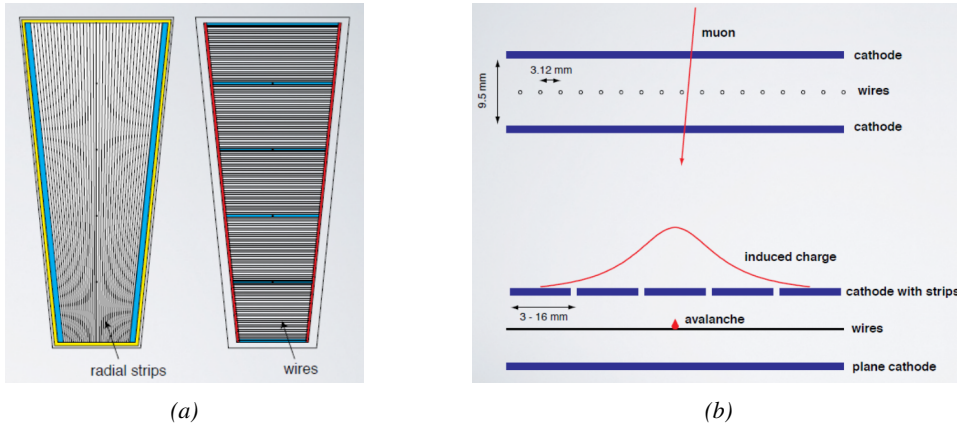


Figure 2.17: Figure 2.17a: cathode strips and anode wire layout of a CSC panel. Figure 2.17b avalanche development and charge collection by anode wires and induction on cathode strips inside of a CSC panel.

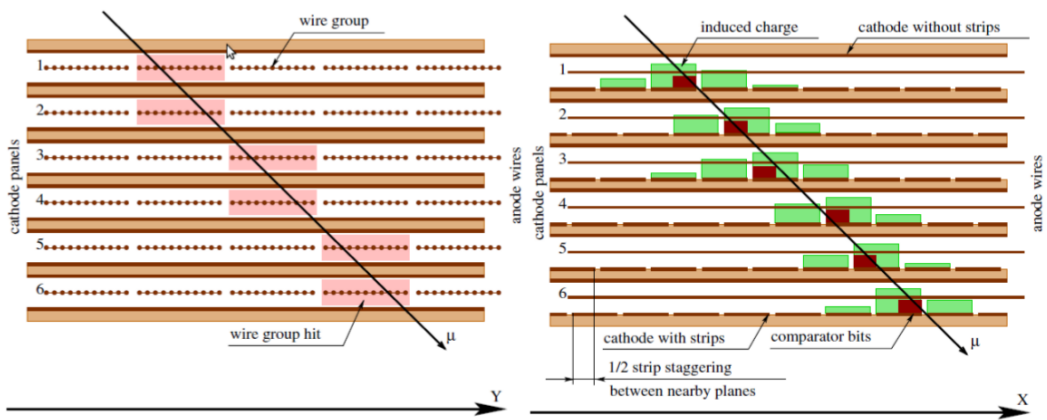


Figure 2.18: Muon track reconstruction through the 6 panels of a CMS CSC using the information of anode wire groups and cathode strip charge distribution combined with comparator bits to decide on which half strip the muon is more likely to have passed.

The 540 CMS CSCs, found in the endcaps covering the pseudorapidity region $0.9 < |\eta| < 2.5$ and described through Figure 2.17, are composed of 6 panels of CSC, each panel consisting in a wide gas volume of 9.5 mm (7 mm in the case of ME1/1 station) containing anode wires and whose surfaces are cathodes. The top cathode is a wide copper plane of the size of the gas volume. The bottom cathode is divided into thin trapezoidal copper strips radially arranged to measure the azimuthal coordinate ϕ with a pitch ranging from 8 to 16 mm. The $0.50 \mu\text{m}$ anode wires are placed perpendicularly to the strips to measure radial coordinate r and are grouped by 10 to 15 with a wire to wire space of 3.2 mm. In the specific case of ME1/1 placed against the HCAL endcap, the $0.30 \mu\text{m}$ anode wires have a wire to wire distance of 2.5 mm and are not disposed perpendicularly to the strips but slightly tilted by an angle of 29 deg to compensate for the lorentz force due to the very strong local magnetic field of 4 T. These detectors are operated with a 40/50/10 mixture of Ar, CO₂ and CF₄. Combining the information of the multiple CSC panels, the detectors achieve a very precise measurement of the muon track.

Despite their excellent spatial resolution, the wire chambers (DTs and CSCs) are limited in terms of time resolution by the fact that the charge needs to drift towards the anode wire and be collected before having the confirmation that a particle was detected as the drift volume is not used to develop avalanches. Indeed, the stronger electric field close to the anode wire triggers the avalanche and the gain of the detector. Due to the drift, the time resolution is thus limited at best to approximately 2 to 3 ns. In addition, even though the intrinsic time resolution of the tracking chambers is rather good compared to the 25 ns in between successive collisions, the processing time of the trigger system doesn't allow for very fast triggering as it provides a time precision of only 12.5 ns. Thus, detectors fully dedicated to timing measurement have been installed as a redundant system. These detectors are RPCs, also gaseous detectors but that use current induction instead of charge collection allowing for a time resolution of the order of 1.5 ns only. Theoretically, depending on the design used, RPCs could reach a time resolution of the order of 10 ps but in the context of LHC where bunch crossing happen every 25 ns, a time resolution of 1.5 ns is sufficient to accurately assign the right bunch crossing to each detected muon.

The 1056 RPCs equipping the CMS muon system both in the barrel and endcap regions and covering the pseudorapidity region $0 < |\eta| < 1.6$ are composed of two layers of RPC *gaps* as described in Figure 2.19. Each gap consists in two resistive electrodes made out of 2 mm thick Bakelite enclosing a 2 mm thick gas volume containing a 95.2/4.5/0.3 mixture of $C_2H_2F_4$, $i - C_4H_{10}$ and SF_6 . Due to this geometry, the electric field inside of a gap is homogeneous and linear at every point in the gas translating into a uniform development of avalanches in the gas volume as soon as a passing muon ionises the gas. The two gaps sandwich a readout copper strip plane. A negative voltage is applied on the outer electrodes, used as cathodes, and the inner electrodes, the anodes, are simply connected to the ground as well as the readout panel that picks up the current induced by the accumulated charge of the growing avalanches in one or both of the gas gaps. This OR system allows for a lower gain (i.e. a lower electric field) on both gaps to reach the maximal efficiency of such a detector.

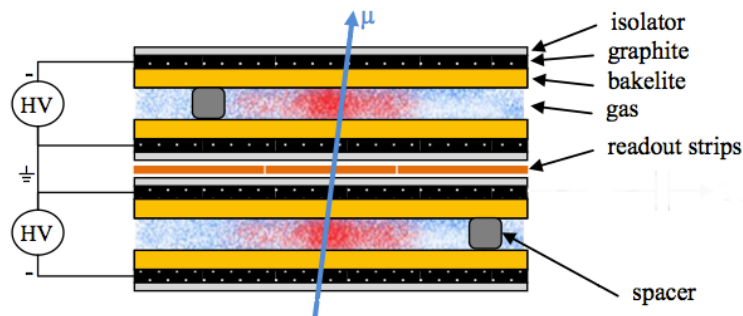


Figure 2.19: Double gap layout of CMS RPCs. Muons passing through the gas volumes will create electron-ion pairs by ionising the gas. this ionisation will immediately translate into a developing avalanche.

2.2.3 High Luminosity LHC

The very first proton beam successfully circulated in the LHC in September 2008 directly followed by an incident leading to mechanical damage that would delay the LHC program for a year until November 2009, the very first collisions at a center-of-mass energy of 7 TeV taking place in March 2010. The energy of the beam would be increased after a First Long Shutdown (LS1) starting early

1235 2013 after less than 3 years of data taking. Nevertheless, this first data taking period at only 7 TeV
 1236 was sufficient to claim the discovery of a new particle compatible with the Higgs boson in July 2012.
 1237 During the 2 years of shutdown, the upgrade of the accelerator allowed for several maintainances
 1238 along the beam pipes, repair and consolidation of magnet connection and high-current splices. But
 1239 not only the LHC was upgraded. Indeed, the experiments at the 4 collision points also took the
 1240 advantage of this time to upgrade their system in prevision of the next LHC run (Run-II) until
 1241 2018 and the Second Long Shutdown (LS2) as the luminosity and energy of the beam would be
 1242 continuously increasing. By the end of Run-II, the luminosity will have reached twice its nominal
 1243 value when the center-of-mass energy has already got close to its nominal value by reaching an
 1244 historical 13 TeV for the first time in 2017.

1245 The next long shutdown will occur at the end of this year and will again be the occasion for simi-
 1246 lar maintenance and consolidation in prevision of Run-III and the future upgrade of LS3. Still, the
 1247 main occupation of LS2 on LHC side will be the upgrade of LHC injectors. On the experiments side,
 1248 LHCb and ALICE will, in a very tight schedule, implement major upgrades while ATLAS and CMS
 1249 will wait until LS3 to upgrade their detectors in prevision of high luminosity LHC-Phase-II. ALICE
 1250 main challenge is an upgrade of their apparatus to cope with the 50 kHz $Pb - Pb$ collisions. Simi-
 1251 larly, LHCb will upgrade their frontend readout electronics to cope with the full 40 MHz collisions
 1252 delivered by LHC. ATLAS will perform standard maintenance and CMS will focus on the urgent up-
 1253 grade of the pixel detector and on the installation of new muon detectors in order to take profit of LS2
 1254 time to mitigate the upgrade of detectors foreseen during LS3. Run-III will start in 2021 with the LHC
 1255 at its nominal center-of-mass energy and will bring LHC-Phase-I to an end at the end of 2023. By
 1256 then the luminosity will only increase to reach 2.5 times the nominal luminosity but during these 3
 1257 years of run, the LHC will deliver as much integrated luminosity as what what brought during the al-
 1258 most 7 years of both Run-I and II of data taking. Phase-I will end with an overall 300 fb^{-1} delivered.
 1259



Figure 2.20: Detailed timeline of for LHC and HL-LHC operation until 2028 and operation projection until 2038. This timeline only describes the operation plans after LS1.

1260 After approximately 15 years of operation, the LHC will undergo a new series of upgrade during

the LS3 in order to boost its discovery potential. This moment onward is what is referred to HL-LHC or Phase-II as showed in Figure 2.20. The goal is to aim to a luminosity 5 to 7 times stronger than the nominal one trying to reach even 10 times this value if possible. Increasing the luminosity means that the beam size at the collision points needs to be reduced to boost the number of collisions per bunch. For this purpose, new focusing and bending magnets and collimators will be installed at the collision points as well as newly developed "crab cavities" that will tilt the particle bunches just prior to the collisions by giving them transverse momentum and thus increasing their meeting area. In addition, the full proton injection line will be upgraded.

Over its full lifetime, the HL-LHC is expected to deliver an outstanding integrated luminosity of 3000 fb^{-1} leading, in the case of Higgs studies, to measuring the couplings of the boson to a precision of 2 to 5% thanks to the estimated 15 millions of Higgs created each year providing a more precise measurement of potential deviations from the theoretical predictions. SUSY studies would also see their limits pushed away and could lead to a new breakthrough. SUSY is a particularly important topic as it could give an answer to why the Higgs boson can stay so light while coupled to heavy particles by introducing the contributions of the super partners on top of providing dark matter candidates. Finally, the increase of luminosity will give the possibility to investigate "exotic" mode like for example the models introducing extra dimensions to explain the hierarchy problem.

On the experiments side, the pile-up (PU) will be increased up to 150 to 200 interactions per bunch crossing in ATLAS and CMS, making necessary an strong upgrade of the trigger system and of the inner trackers and of the calorimeters. Both ATLAS and CMS will also need to upgrade the muon trigger at the level of the endcaps mainly focusing on the coverage near the beam line in order to increase the detection acceptance and event selection. Moreover, the increased luminosity will also lead to an increased background rate and a faster ageing of the detectors. This PhD work takes place into this very specific context of muon detector consolidation and certification for the HL-LHC period in order to provide the CMS experiment with robust detectors that will live through the next 20 years of HL-LHC.

2.3 Muon Phase-II Upgrade

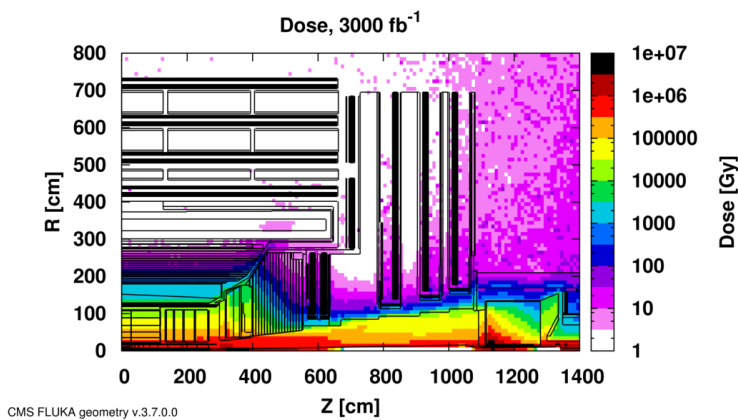


Figure 2.21: Absorbed dose in the CMS cavern after an integrated luminosity of 3000 fb^{-1} . R is the transverse distance from the beamline and Z is the distance along the beamline from the Interaction Point at $Z=0$.

The end of 2018 will mark the beginning of LS2 and the start of Phase-II upgrade activities. From the HL-LHC period onwards, i.e. past LS3, the performance degradation due to integrated radiation as well as the average number of inelastic collisions per bunch crossing, seen as pile-up into the detector readout that far exceeds the original LHC plans, will rise substantially and become a major challenge for all of the LHC experiments, like CMS, that were forced to address an upgrade program for Phase-II [22]. Dealing with the data from the muon detectors will force to upgrade the detectors and electronics towards the most recent technologies. Simultaneously, this will push new latency requirements onto Level-1 trigger and data acquisition that will only be fulfilled by upgrading the system with electronics having deeper buffering and faster processing. Simulations of the expected distribution of absorbed dose in the CMS detector under HL-LHC conditions show in Figure 4.16 that detectors placed close to the beam line will have to withstand high irradiation, the radiation dose being of the order of a few tens of Gy.

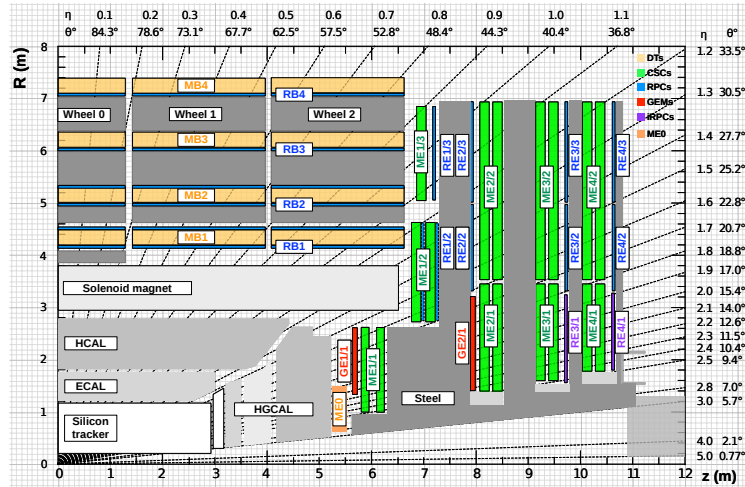


Figure 2.22: A quadrant of the muon system, showing DTs (yellow), RPCs (blue), and CSCs (green). The locations of new forward muon detectors for Phase-II are contained within the dashed box and indicated in red for GEM stations (ME0, GE1/I, and GE2/I) and dark blue for improved RPC (iRPC) stations (RE3/I and RE4/I).

Moreover, the increase of background close to the beam line will affect the background rate seen by the muon detectors in this area and tracking muons will prove to be difficult as this region is not yet equipped with all the detectors that were already foreseen for Phase-I. Improving this situation will come with the increase of hit numbers recorded along the particle track to reduce the ambiguity on muon versus background detection. The measurement of small production cross-section and/or decay branching ratio processes, such as the Higgs boson coupling to charge leptons or the $B_s \rightarrow \mu^+ \mu^-$ decay, is of major interest and specific upgrades in the forward regions of the detector will be required to maximize the physics acceptance on the largest possible solid angle.

To ensure proper trigger performance within the present coverage, the muon system will be completed with new chambers. Figure 2.22 shows the addition of Gas Electron Multiplier (GEM) and RPCs in the pseudo-rapidity region $1.6 < |\eta| < 2.4$ to complete the redundancy of the already existing CSCs as originally scheduled in the CMS Technical Proposal [23]. A first step into this direction will be taken by installing GEMs on the first endcap disk in position GE1/I during LS2, during which preparations for the future installation of more GEMs and RPCs will take place by

1314 installing the needed services. During the YETS following LS2, improved RPC (iRPC) will be
 1315 installed on the third and fourth endcap disks in position RE3/1 and RE4/1, and more GEMs will
 1316 equip the second endcap in position GE2/1 and the inner layer, closest to the HCAL endcap called
 1317 ME0 during LS3, finally completing the redundant coverage of the muon system.

1318 Nevertheless, the region beyond $|\eta| > 2.4$ and extending to $|\eta| = 5.0$ only is covered by the for-
 1319 ward HCAL detectors. Extensions of the tracker in the context of HL-LHC will increase its coverage
 1320 up to $|\eta| = 4.0$ but the identification of muons and measurement of their energy with reasonable pre-
 1321 cision with only the tracker is nearly impossible. Thus, this increased tracker coverage range needs
 1322 to be put in parallel with a matching muon detector and will open doors to multi-lepton final states
 1323 in which leptons are likely to have a great momentum and to be found near the beam line.

1324

1325 Finally, as the muon system is composed only of gaseous detectors, strong environmental con-
 1326 cerns have risen over the last years as the European directives will restrict the use of fluorine based
 1327 gas mixtures. Both the CSC and RPC subsystems, using CF_4 , $C_2H_2F_4$, or SF_6 , will need to adapt
 1328 their working gas in order to strongly reduce the greenhouse potential of the mixtures released into
 1329 the atmosphere due to gas leaks.

1330 **2.3.1 Phase-II upgrade of the DT system**

1331 **2.3.2 Phase-II upgrade of the CSC system**

1332 **2.3.3 Phase-II upgrade of the RPC system**

1333 RPCs are used by the CMS first level trigger for their good timing performances. Indeed, a very
 1334 good bunch crossing identification can be obtained with the present CMS RPC system, given their
 1335 fast response of the order of 1 ns. In order to contribute to the precision of muon momentum mea-
 1336 surements, muon chambers should have a spatial resolution less or comparable to the contribution
 1337 of multiple scattering [21]. Most of the plausible physics is covered only considering muons with
 1338 $p_T < 100$ GeV thus, in order to match CMS requirements, a spatial resolution of $\mathcal{O}(\text{few mm})$ the
 1339 proposed new RPC stations, as shown by the simulation in figure 2.23. According to preliminary
 1340 designs, RE3/1 and RE4/1 readout pitch will be comprised between 3 and 6 mm and 5 η -partitions
 1341 could be considered.

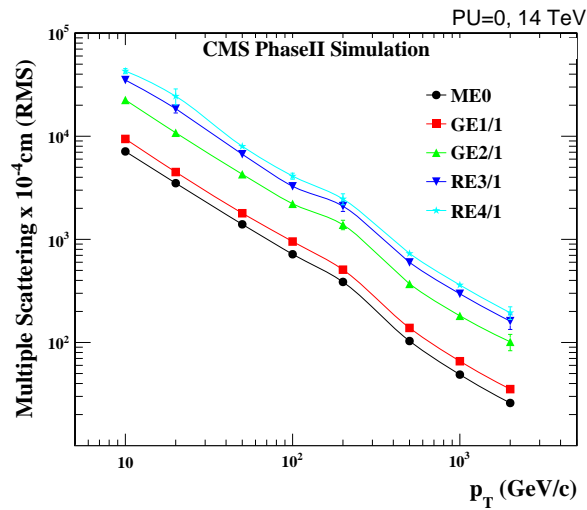


Figure 2.23: RMS of the multiple scattering displacement as a function of muon p_T for the proposed forward muon stations. All of the electromagnetic processes such as bremsstrahlung and magnetic field effect are included in the simulation.

1342 2.3.4 Phase-II upgrade of the Level-1 trigger

3

1343

1344

Physics of Resistive plate chambers

1345 A Resistive Plate Chamber (RPC) is a gaseous detector using the same physical processes described
1346 in Chapter 3. It has been developed in 1981 by Santonico and Cardarelli [24], under the name of
1347 *Resistive Plate Counter*, as an alternative to the local-discharge spark counters proposed in 1978
1348 by Pestov and Fedotovich [25, 26]. Working with spark chambers implied using high-pressure gas
1349 and high mechanical precision which the RPC simplified by formerly using a gas mixture of argon
1350 and butane flowed at atmospheric pressure and a constant and uniform electric field propagated
1351 in between two parallel electrode plates. Moreover, a significant increase in rate capability was
1352 introduced by the use of electrode plate material with high bulk resistivity, preventing the discharge
1353 from growing throughout the whole gas gap. Indeed, the effect of using resistive electrodes is that
1354 the constant electric field is locally canceled out by the development of the discharge, limiting its
1355 growth.

1356 Through its development history, different operating modes [27–29] and new detector designs [30–
1357 32] have been discovered, leading to further improvement of the rate capability of such a detector.
1358 Moreover, the addition of SF_6 into the gas mix improved the stability of operation of the RPC [33,
1359 34].

1360 The low developing costs and easily achievable large detection areas offered by RPCs, as well as
1361 the wide range of possible designs, made them a natural choice to as muon chambers and/or trigger
1362 detectors in multipurpose experiments such as CMS [21] or ATLAS [35], time-of-flight detectors in
1363 ALICE [36], calorimeter with CALICE [37] or even detectors for volcanic muography with ToMu-
1364 Vol [38].

1365 3.1 Principle

1366 RPCs are ionisation detectors composed of two parallel resistive plate electrodes in between which
1367 a constant electric field is set. The space in between the electrodes, referred as *gap*, is filled with a
1368 dense gas that is used to generate primary ionization into the gas volume. The free charge carriers
1369 (electrons and cations) created by the ionization of the gas molecules are then accelerated towards

¹³⁷⁰ the electrodes by the electric field, as shown in Figure 3.1 [39].

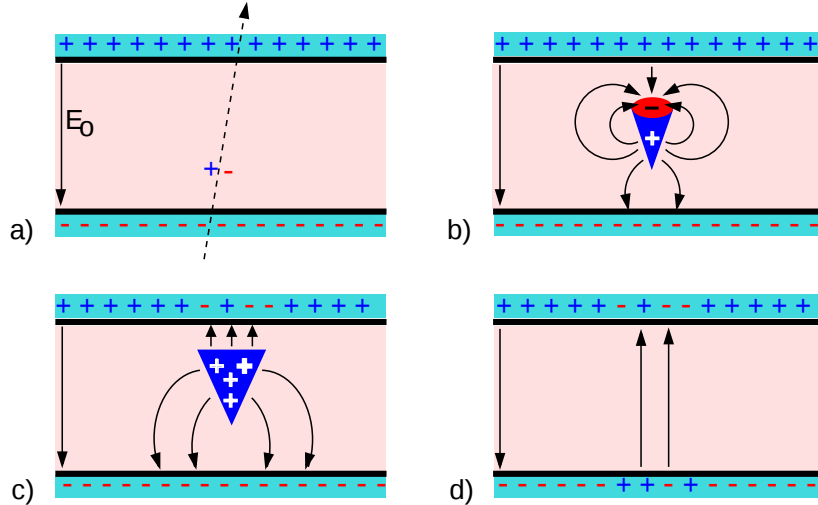


Figure 3.1: Different phases of the avalanche development in the RPC gas volume subjected to a constant electric field E_0 . a) An avalanche is initiated by the primary ionisation caused by the passage of a charged particle through the gas volume. b) Due to its growing size, the avalanche starts to locally influence the electric field. c) The electrons, lighter than the cations reach the anode first. d) The ions reach the cathode. While the charges have not recombined, the electric field in the small region around the avalanche stays affected and locally blind the detector.

¹³⁷¹ RPCs being passive detectors, a current on pick-up copper read-out placed outside of the gas
¹³⁷² volume is induced by the charge accumulation during the growth of the avalanche. As a result,
¹³⁷³ the time resolution of the detector is substantially increased as the output signal is generated while
¹³⁷⁴ the electrons are still in movement. The advantage of a constant electric field, over multi-wire
¹³⁷⁵ proportional chambers, is that the electrons are being fully accelerated from the moment charge
¹³⁷⁶ carriers are freed and feel the full strength of the electric field that doesn't depend on the distance to
¹³⁷⁷ the readout and that the output signal doesn't need for the electrons to be physically collected.

¹³⁷⁸ The typical gas mixture RPCs are operated with is generally composed of 3 gas compounds.

- ¹³⁷⁹ • Tetrafluoroethane ($C_2F_4H_2$), also referred to as *Freon*, is the principal compound of the RPC
¹³⁸⁰ gas mixtures, with a typical fraction above 90%. It is used for it's high effective Townsend
¹³⁸¹ coefficient and the great average fast charge that allows to operate the detector with a high
¹³⁸² threshold with respect to argon, for example, that has similar effective Townsend coefficient
¹³⁸³ but suffers from a lower fast charge. To operate with similar conditions, argon would require a
¹³⁸⁴ higher electric field leading to a higher fraction of streamers, thus limiting the rate capability
¹³⁸⁵ of the detector [40].
- ¹³⁸⁶ • Isobutane (i- C_4H_{10}), only present in a few percent in the gas mixtures, is used for its UV
¹³⁸⁷ quenching properties [41] helping to prevent streamers due to UV photon emission during the
¹³⁸⁸ avalanche growth.
- ¹³⁸⁹ • Sulfur hexafluoride, (SF_6), referred to simply as *SF6*, is used in very little quantities for its
¹³⁹⁰ high electronegativity. Excess of electrons are being absorbed by the compound and streamers

1391 are suppressed [34]. Nevertheless, a fraction of SF_6 higher than 1% will not bring any extra
 1392 benefit in terms of streamer cancelation power but will lead to higher operating voltage [33],
 1393 as can be understood through Figure 3.2.

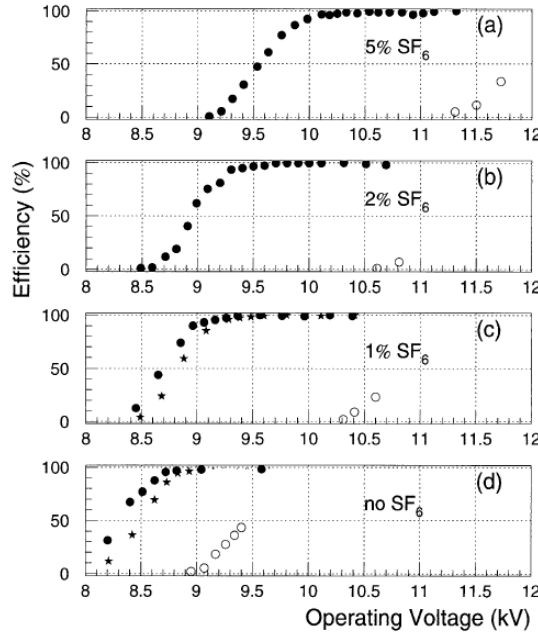


Figure 3.2: Efficiency (circles and stars with 30 mV and 100 mV thresholds respectively) and streamer probability (opened circles) as function of the operating voltage of a 2 mm single gap HPL RPC flushed with a gas mixture containing (a) 5%, (b) 2%, (c) 1% and (d) no SF_6 [33].

1394 After an avalanche developed in the gas, a time long compared to the development of a discharge
 1395 is needed to recombine the charge carriers in the electrode material due to their resistivity. This
 1396 property has the advantage of affecting the local electric field and avoiding sparks in the detector
 1397 but, on the other hand, the rate capability is intrinsically limited by the time constant τ_{RPC} of the
 1398 detector. Using a quasi-static approximation of Maxwell's equations for weakly conducting media,
 1399 it can be shown that the time constant τ_{RPC} necessary to the charge recombination at the interface
 1400 in between the electrode and the gas volume is given by the Formula 3.1 [42].

$$\tau_{RPC} = \frac{\epsilon_{electrode} + \epsilon_{gas}}{\sigma_{electrode} + \sigma_{gas}} \quad (3.1)$$

1401 A gas can be assimilated to vacuum, leading to $\epsilon_{gas} = \epsilon_0$ and $\sigma_{gas} = 0$, and the electrodes
 1402 permittivity and conductivity can be written as $\epsilon_{electrode} = \epsilon_r \epsilon_0$ and $\sigma_{electrode} = 1/\rho_{electrode}$,
 1403 showing the strong dependence of the time constant to the electrodes resistivity in Formula 3.2.

$$\tau_{RPC} = (\epsilon_r + 1)\epsilon_0 \times \rho_{electrode} \quad (3.2)$$

1404 Very few materials with a low enough resistivity exist in nature. The resistivity targeted to build
 1405 RPCs ranges from 10^9 to $10^{12} \Omega \cdot \text{cm}$. The most common RPC electrode materials are displayed in
 1406 Table 3.1. When the doped glass and ceramics can offer short time constants of the order of 1 ms,

¹⁴⁰⁷ the developing cost of such materials is quite high due to the very low demand. Thus, High-pressure
¹⁴⁰⁸ laminate (HPL) is often the choice for high rate experiments using very large RPC detection areas.
¹⁴⁰⁹ Other experiments working at cosmic muon fluxes can safely operate with ordinary float glass.

Material	$\rho_{electrode}$ ($\Omega \cdot \text{cm}$)	ϵ_r	τ_{RPC} (ms)
Float glass	10^{12}	~ 7	~ 700
High-pressure laminate	10^{10} to 10^{12}	~ 6	~ 6 to 600
Doped glass (LR S)	10^9 to 10^{11}	~ 10	~ 1 to 100
Doped ceramics (SiN/SiC)	10^9	~ 8.5	~ 1
Doped ceramics (Ferrite)	10^8 to 10^{12}	~ 20	~ 0.2 to 2000

Table 3.1: Properties of the most used electrode materials for RPCs.

¹⁴¹⁰ 3.1.1 Electron drift velocity

¹⁴¹¹ Talk about the electron drift velocity and mention the time resolution of RPCs.

¹⁴¹² 3.2 Rate capability and time resolution of Resistive Plate Chambers

¹⁴¹⁴ As already previously discussed, the electrode material plays a key role in the max intrinsic rate
¹⁴¹⁵ capability of RPCs. R&D is being done to develop at always cheaper costs material with lower
¹⁴¹⁶ resistivity. Nevertheless, the amount of charge released, i.e. the size of the discharge, if reduced
¹⁴¹⁷ leads to a smaller blind area in the detector, increasing the rate capability of the detector.

¹⁴¹⁸ 3.2.1 Operation modes

¹⁴¹⁹ RPCs where developed early 1980s. At that time it was using an operating mode now referred to
¹⁴²⁰ as *streamer mode*. Streamers are large discharges that develop in between the 2 electrodes enough
¹⁴²¹ to locally discharge the electrodes. If the electric field inside of the gas volume is strong enough,
¹⁴²² with electrons being fast compared to ions, a large and dense cloud of positive ions will develop
¹⁴²³ nearby the anode and extend toward the cathode while the electrons are being collected, eventually
¹⁴²⁴ leading to a streamer discharge due to the increase of field seen at the cathode. the field is then strong
¹⁴²⁵ enough so that electrons are pulled out of the cathode. Electrodes, though they are a unique volume
¹⁴²⁶ of resistive material, can be assimilated to capacitors. At the moment an electric field is applied in
¹⁴²⁷ between their outer surfaces, the charge carriers inside of the volume will start moving leading to
¹⁴²⁸ a situation where there is no voltage across the electrodes and a higher density of negative charges,
¹⁴²⁹ i.e. electrons, on the inner surface of the cathode. Finally, when a streamer discharge occurs, these
¹⁴³⁰ electrons are partially released in the gas volume contributing to increase the discharge strength until
¹⁴³¹ the formation of a conductive plasma, the streamer. This can be understood through Figure 3.3 [27].
¹⁴³² Streamer signals are very convenient in terms of read-out as no amplification is required with output
¹⁴³³ pulses amplitudes of the order of a few tens to few hundreds of mV as can be seen on Figure 3.4.

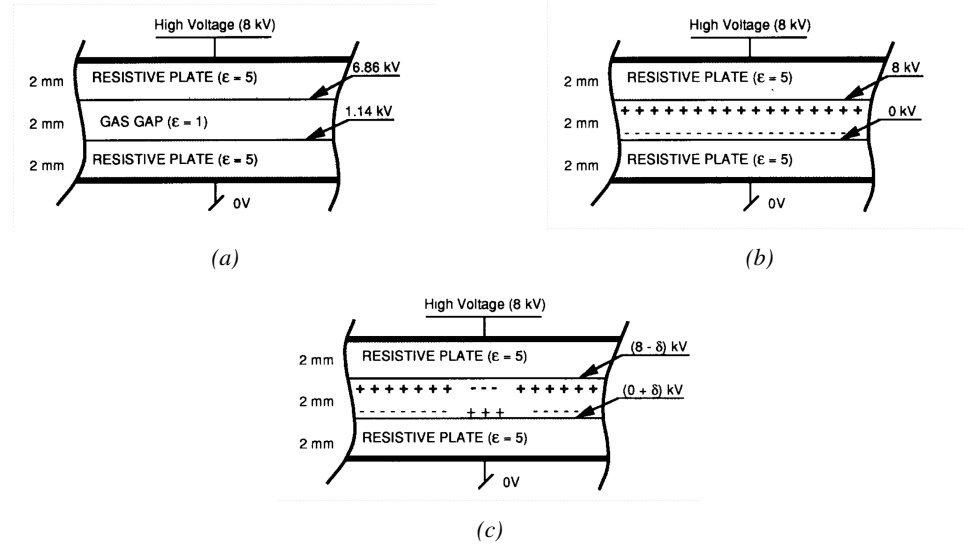


Figure 3.3: Movement of the charge carriers in an RPC. Figure 3.3a: Voltage across an RPC whose electrode have a relative permittivity of 5 at the moment the tension is applied. Figure 3.3b: After the charge carriers moved, the electrodes are charged and there is no voltage drop over the electrodes anymore. The full potential is applied on the gas gap only. Figure 3.3c: The streamer discharge initiated by a charged particle transports electrons and cations towards the anode and cathode respectively.

When the electric field is reduced though, the electronic gain is small until the electrons get close enough to the anode and the positive ion cloud is much smaller. The electric field cannot rise to the point a field emission of electrons on the cathode is possible. The resulting signal is weak, of the order of a few mv as shown on Figure 3.4, and requires amplification. This is the *avalanche mode* of RPC operation.

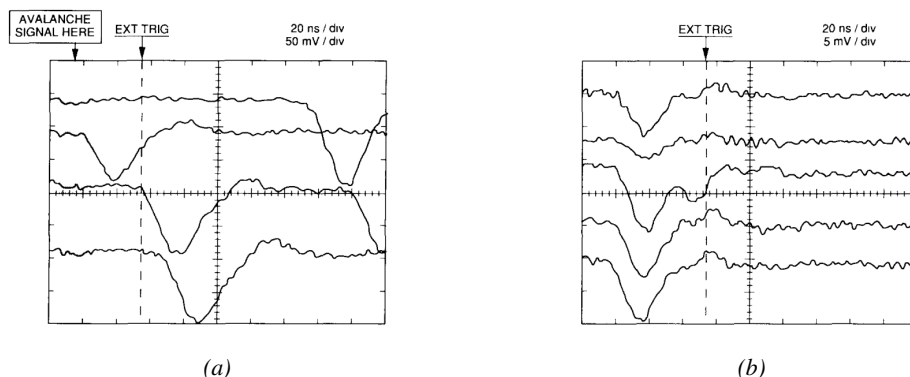


Figure 3.4: Typical oscilloscope pulses in streamer mode (Figure 3.4a) and avalanche mode (Figure 3.4b). In the case of streamer mode, the very small avalanche signal is visible.

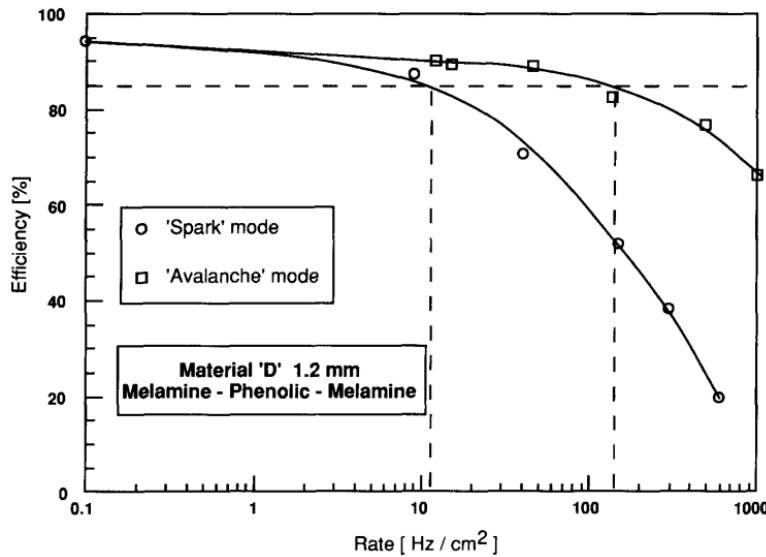


Figure 3.5: Rate capability comparison for the streamer and avalanche mode of operation. An order of magnitude in rate capability for a maximal efficiency drop of 10% is gained by using the avalanche mode over the streamer mode.

This mode offers a higher rate capability by providing smaller discharges that don't affect the electrodes charge and are more locally contained in the gas volume as was demonstrated by Crotty with Figure 3.5 [27]. The detector only stays locally blind the time the charge carriers are recombined and there is no need for electrode recharge which is a long process affecting a large portion of the detector. Another advantage of avalanche signals over streamer is the great time consistency. Figure 3.4 shows very clearly that avalanche signals have a very small time jitter. This is a natural choice for high rate experiments.

3.2.2 Detector designs and performance

Different RPC design have been used and each of them present its own advantages. Historically, the first type of RPC to have been developed is what is referred now to *narrow gap* RPC [24, 43]. After the avalanche mode has been discovered [27], it has been proven that increasing the width of the gas gap lead to higher rate capability, due to lower charge deposition per avalanche, and lower power dissipation [43]. Nevertheless, by increasing the gas gap width, the time resolution of the detector decreases. This is a natural result if the increase of active gas volume in the detector is taken into account. Indeed, for a given threshold, only the small fraction of gas closest to the cathode will provide enough gain to have a detectable signal. In the case of a wider gas volume, the active region is then larger and a larger time jitter is introduced with the variation of starting position of the avalanche, as discussed in [30]. To solve improve both the time resolution and the rate capability, different methods were used trying to get advantages of both narrow and wide gap RPCs.

1458 **3.2.2.1 Double-gap RPC**

1459 Double-gap RPCs are made out of 2 narrow RPC detectors. The 2 RPC gaps are stacked on top of
 1460 each other as shown in Figure 3.6. This detector layout, popularized by the two multipurpose experiments
 1461 CMS [21] and ATLAS [35] at LHC, can be used as an OR system in which each individual
 1462 chamber participates in the output signal. The gain of such a detector is greatly reduced with respect
 1463 to single-gap RPCs with an efficiency plateau reached at lower voltage, as visible on Figure 3.7.

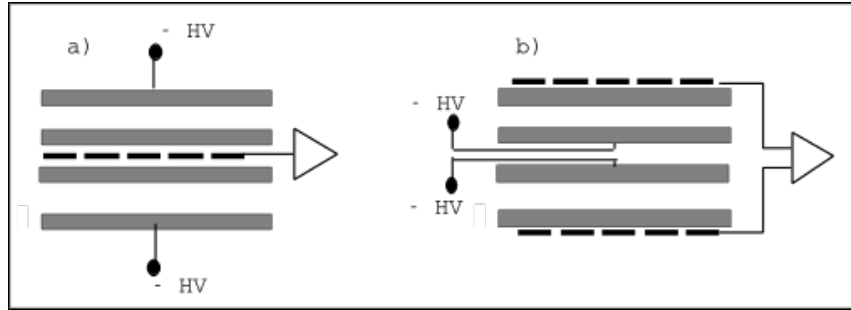


Figure 3.6: Possible double-gap RPC layouts: a) "standard" 1D double-gap RPC, as used in CMS experiment, where the anodes are facing each other and a 1D read-out plane is sandwiched in between them, b) double read-out double-gap RPC as used in ATLAS experiment, where the cathodes are facing each other and 2 read-out planes are used on the outer surfaces. This last layout can offer the possibility to use a 2D reconstruction by using orthogonal read-out planes.

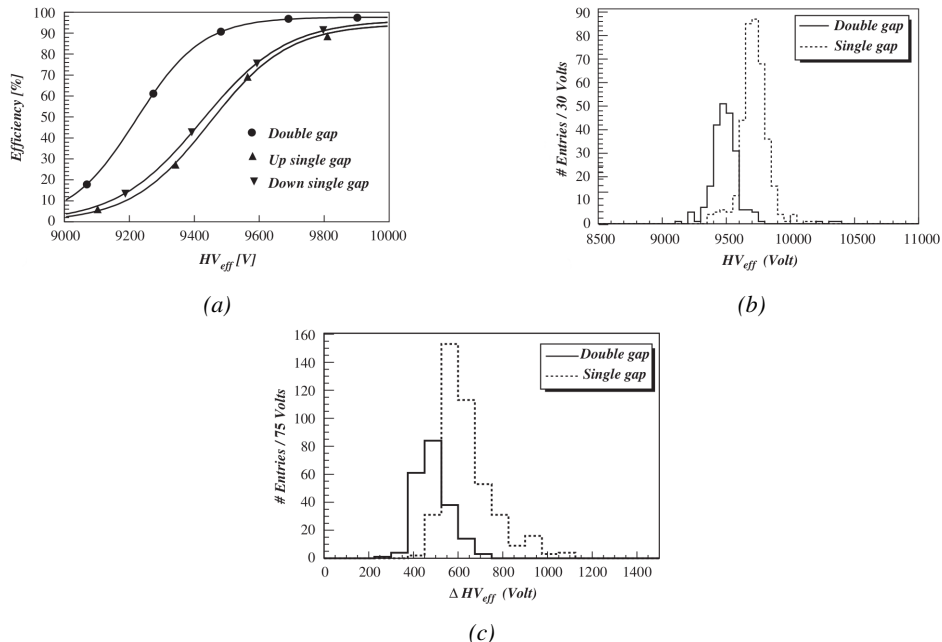


Figure 3.7: Comparison of performance of CMS double and single gap RPCs using cosmic muons [44]. Figure 3.7a: Comparison of efficiency sigmoids. Figure 3.7b: Voltage distribution at 95% of maximum efficiency. Figure 3.7c: $\Delta_{10\%}^{90\%}$ distribution.

3.2.2.2 Multigap RPC (MRPC)

MRPCs are layouts in which floating sub electrode plates are placed into a wide gap RPC to divide the gas volume and create a sum of narrow gaps [30, 31]. The time resolution of such a detector can reach of few tens of ps, with gas gaps of the order of a few hundred μm as shown in Figure 3.8 representing ALICE Time-of-flight (ToF) MRPCs.

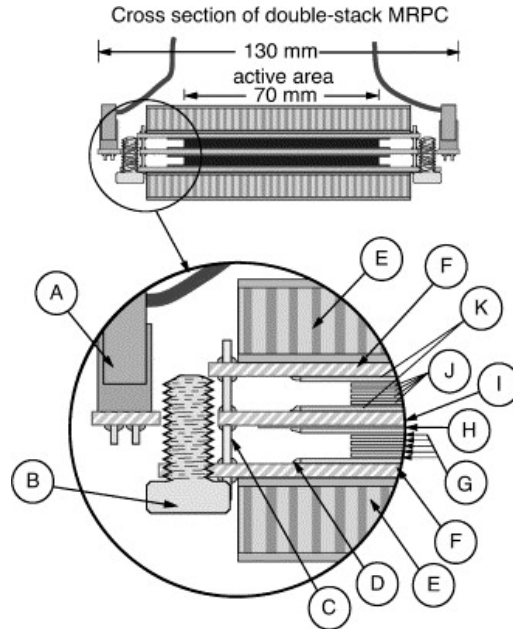


Figure 3.8: Presentation of ALICE MRPC using $250 \mu\text{m}$ gas gaps, $620 \mu\text{m}$ outer glass electrodes and $550 \mu\text{m}$ inner floating electrodes. More details on the labels are given in [45].

Sometimes used as a double multigap RPC, taking advantage of the OR of double gap RPCs, the MRPC is mainly used as ToF detector [45–49] due to its excellent timing properties that allow to perform particle identification as explained by Williams in [50]. The principle of particle identification using ToF is simply the measurement of the velocity of a particle. Indeed, particles are defined by their mass (for the parameter of interest here, their electric charge being measured using the bending angle of the particles traveling through a magnetic field) and this mass can be calculated by measuring the velocity β and momentum of the particle:

$$\beta = \frac{p}{\sqrt{p^2 + m^2}} \quad (3.3)$$

Intuitively, it is trivial to understand that 2 different particles having the same momentum will have a different velocity due to the mass difference and thus a different flight time T_1 and T_2 through the detector and this is used to separate and identify particles. The better the time resolution of the ToF system used, the stronger will the separation be:

$$T = \frac{L}{v} = \frac{L}{c \cdot \beta}, \quad \Delta T = T_1 - T_2 = \frac{L}{c} \left(\sqrt{1 + m_1^2/p^2} - \sqrt{1 + m_2^2/p^2} \right) \cong (m_1^2 - m_2^2) \frac{L}{2cp^2} \quad (3.4)$$

1480 An example of particle identification is given for the case of STAR experiment in Figure 3.9.

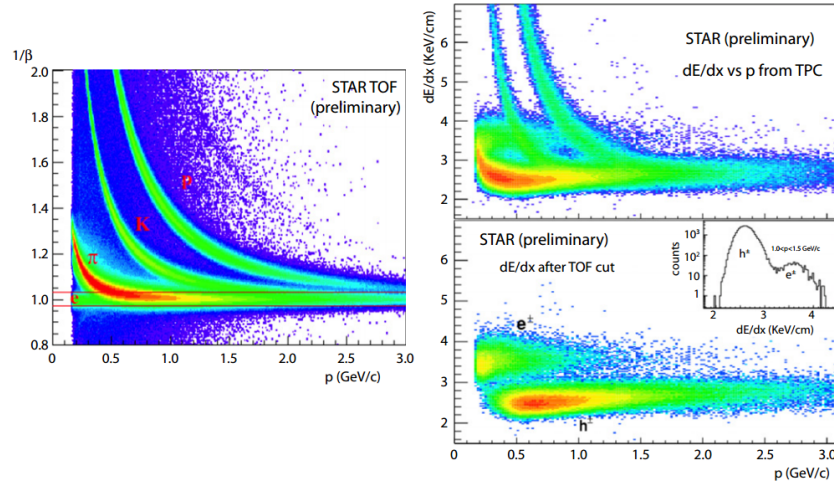


Figure 3.9: Particle identification applied to electrons in the STAR experiment. The identification is performed combining ToF and dE/dx measurements [50].

1481 Another benefice of using such small gas gaps is the strong reduction of the average avalanche
1482 volume and thus of the blind spot on MRPCs leading to an improved rate capability. Multigaps can
1483 sustain backgrounds of several kHz/cm² as demonstrated in Figure 3.10.

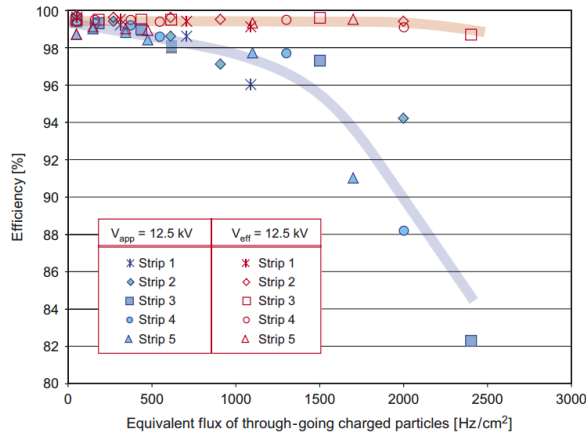


Figure 3.10: Comparison of the detector performance of ALICE ToF MRPC [51] at fixed applied voltage (in blue) and at fixed effective voltage (in red). The effective voltage is kept fixed by increasing the applied voltage accordingly to the current drawn by the detector.

1484 3.2.2.3 Charge distribution and performance limitations

1485 The direct consequence of the different RPC layouts is a variation of intrinsic time resolution of the
1486 RPC as the gap size decreases. An advantage is given to multigaps whose design use sub-millimeter
1487 gas volumes providing very consistent signals.

1488 On the charge spectrum point of view, each layout has its own advantages. When the double-gap
 1489 has the highest induced over drifting charge ratio, as seen in Figure 3.11, the multigap has a charge
 1490 spectrum strongly detached from the origin, as visible in Figure 3.12. A high induced over drifting
 1491 charge ratio means that the double gap can be safely operated at high threshold or that at similar
 1492 threshold it can be operated with a twice smaller drifting charge, meaning a higher rate capability.
 1493 On the other hand, the strong detachment of the charge spectrum from the origin in the MRPC case
 1494 allows to reach a higher efficiency with increasing threshold as most of the induced charge is not low
 1495 due to the convolution of several single gap spectra. The range of stable efficiency increases with
 1496 the number of gap, as presented in Figure 3.13.

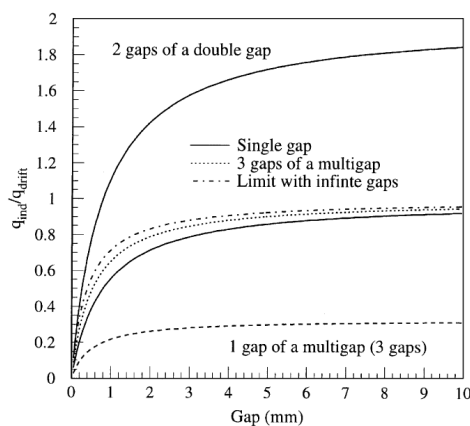


Figure 3.11: Ratio between total induced and drifting charge have been simulated for single gap, double-gap and multigap layouts [52]. The total induced charge for a double-gap RPC is a factor 2 higher than for a multigap.

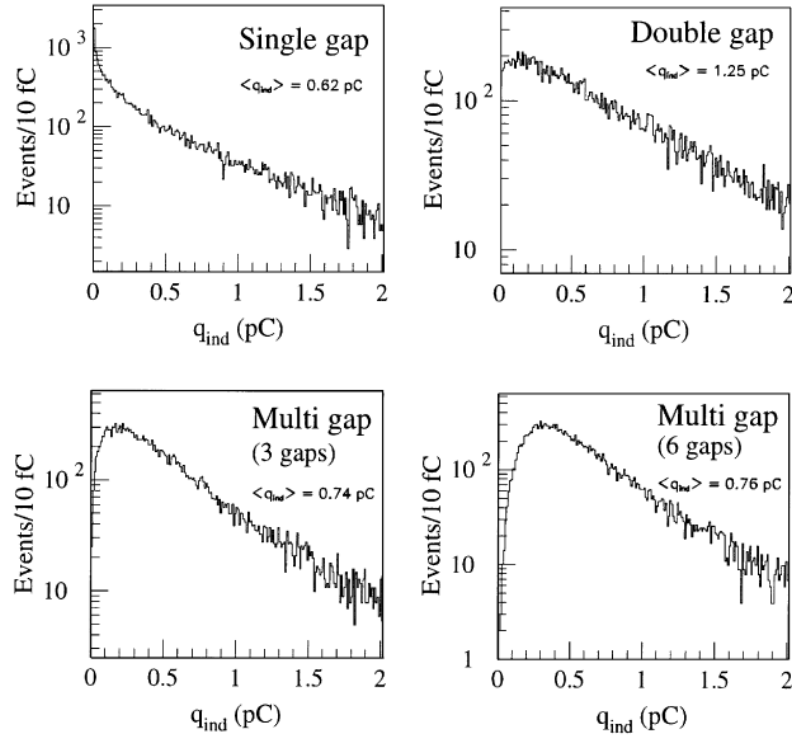


Figure 3.12: Charge spectra have been simulated for single gap, double-gap and multigap layouts [52]. It appears that when single gap shows a decreasing spectrum, double and multigap layouts exhibit a spectrum whose peak is detached from the origin. The detachment gets stronger as the number of gaps increases.

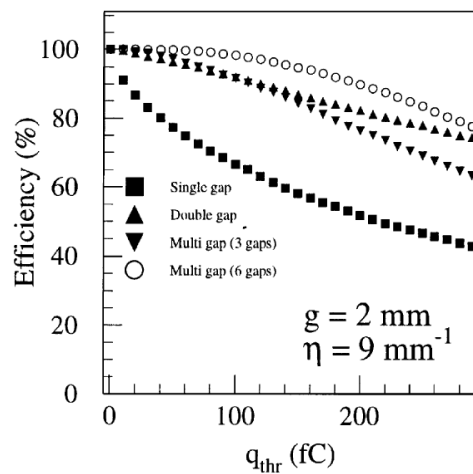


Figure 3.13: The maximal theoretical efficiency is simulated for single gap, double-gap and multigap layouts [52] at a constant gap thickness of 2 mm and using an effective Townsend coefficient of 9 mm^{-1} .

- ¹⁴⁹⁷ **3.3 Signal formation**
- ¹⁴⁹⁸ **3.4 Gas transport parameters**

4

1499

1500

1501

Longevity studies and Consolidation of the present CMS RPC subsystem

4.1 Resistive Plate Chambers at CMS

4.1.1 Overview

1504 The Resistive Plate Chambers (RPC) system, located in both barrel and endcap regions, provides a
1505 fast, independent muon trigger with a looser p_T threshold over a large portion of the pseudorapidity
1506 range ($|\eta| < 1.6$) [add reconstruction].

1507

1508 During High-Luminosity LHC (HL-LHC) operations the expected conditions in terms of back-
1509 ground and pile-up will make the identification and correct P_T assignment a challenge for the Muon
1510 system. The goal of RPC upgrade is to provide additional hits to the Muon system with precise tim-
1511 ing. All these informations will be elaborated by the trigger system in a global way enhancing the
1512 performance of the trigger in terms of efficiency and rate control. The RPC Upgrade is based on two
1513 projects: an improved Link Board System and the extension of the RPC coverage up to $|\eta| = 2.4$.
1514 [FIXME 2.4 or 2.5?]

1515 The Link Board system, that will be described in section xxx, is responsible to process, syn-
1516 chronize and zero-suppress the signals coming from the RPC front end boards. The Link Board
1517 components have been produced between 2006 and 2007 and will be subjected to aging and failure
1518 in the long term. The upgraded Link Board system will overcome the aging problems described in
1519 section xxx and will allow for a more precise timing information to the RPC hits from 25 to 1 ns [ref
1520 section xxx].

1521 The extension of the RPC system up to $|\eta| = 2.1$ was already planned in the CMS TDR [ref
1522 cmstdr] and staged because of budget limitations and expected background rates higher than the rate
1523 capability of the present CMS RPCs in that region. An extensive R&D program has been done in
1524 order to develop an improved RPC that fulfills the CMS requirements. Two new RPC layers in the
1525 innermost ring of stations 3 and 4 will be added with benefits to the neutron-induced background

1526 reduction and efficiency improvement for both trigger and offline reconstruction.

1527 4.1.2 The present RPC system

1528 The RPC system is organized in 4 stations called RB1 to RB4 in the barrel region, and RE1 to RE4
 1529 in the endcap region. The innermost barrel stations, RB1 and RB2, are instrumented with 2 layers
 1530 of RPCs facing the innermost (RB1in and RB2in) and outermost (RB1out and RB2out) sides of the
 1531 DT chambers. Every chamber is then divided from the read-out point of view into 2 or 3 η partitions
 1532 called “rolls”. The RPC system consist of 480 barrel chambers and 576 endcap chambers. Details
 1533 on the geometry are discussed in the paper [ref to geo paper].

1534 The CMS RPC chamber is a double-gap, operated in avalanche mode to ensure reliable operation
 1535 at high rates. Each RPC gap consists of two 2-mm-thick resistive High-Pressure Laminate (HPL)
 1536 plates separated by a 2-mm-thick gas gap. The outer surface of the HPL plates is coated with a thin
 1537 conductive graphite layer, and a voltage is applied. The RPCs are operated with a 3-component,
 1538 non-flammable gas mixture consisting of 95.2% freon ($C_2H_2F_4$, known as R134a), 4.5% isobutane
 1539 ($i-C_4H_{10}$), and 0.3% sulphur hexafluoride (SF_6) with a relative humidity of 40% - 50%. Readout
 1540 strips are aligned in η between the 2 gas gaps. [\[Add a sentence on FEBs.\]](#)

1541 The discriminated signals coming from the Front End boards feed via twisted cables (10 to 20 m
 1542 long) the Link Board System located in UXC on the balconies around the detector. The Link System
 1543 consist of the 1376 Link Boards (LBs) and the 216 Control Boards (CBs), placed in 108 Link Boxes.
 1544 The Link Box is a custom crate (6U high) with 20 slots (for two CBs and eighteen LBs). The Link
 1545 Box contains custom backplane to which the cables from the chambers are connected, as well as the
 1546 cables providing the LBs and CBs power supply and the cables for the RPC FEBs control with use
 1547 of the I2C protocol (trough the CB). The backplane itself contains only connectors (and no any other
 1548 electronic devices).

1549 The Link Board has 96 input channels (one channel corresponds to one RPC strip). The input
 1550 signals are the ~ 100 ns binary pulses which are synchronous to the RPC hits, but not to the LHC
 1551 clock (which drives the entire CMS electronics). Thus the first step of the FEB signals processing
 1552 is synchronization, i.e. assignment of the signals to the BXes (25 ns periods). Then the data are
 1553 compressed with a simple zero-suppressing algorithm (the input channels are grouped into 8 bit
 1554 partitions, only the partitions with at least one nonzero bit are selected for each BX). Next, the non-
 1555 empty partitions are time-multiplexed i.e. if there are more than one such partition in a given BX,
 1556 they are sent one-by-one in consecutive BXes. The data from 3 neighbouring LBs are concentrated
 1557 by the middle LB which contains the optical transmitter for sending them to the USC over a fiber at
 1558 1.6 Gbps.

1559 The Control Boards provide the communication of the control software with the LBs via the
 1560 FEC/CCU system. The CBs are connected into token rings, each ring consists of 12 CBs of one
 1561 detector tower and a FEC mezzanine board placed on the CCS board located in the VME crate in
 1562 the USC. In total, there are 18 rings in the entire Link System. The CBs also perform automatic
 1563 reloading of the LB's firmware which is needed in order to avoid accumulation of the radiation
 1564 induced SEUs in the LBs firmware.

1565 Both LBs and CB are based on the Xilinx Spartan III FPGAs, the CB additionally contains
 1566 radiation-tolerant (FLASH based) FPGA Actel ProAsicPlus.

1567 The High Voltage power system is located in USC, not exposed to radiation and easily accessible
 1568 for any reparation. A single HV channel powers 2 RPC chambers both in the barrel and endcap
 1569 regions. The Low Voltage boards are located in UXC on the balconies and provide the voltage to the

¹⁵⁷⁰ front end electronics.

¹⁵⁷¹ 4.1.3 Pulse processing of CMS RPCs

¹⁵⁷² Signals induced by cosmic particle in the RPC strips are shaped by standard CMS RPC Front-End
¹⁵⁷³ Electronics (FEE) following the scheme of Figure 4.1. On a first stage, analogic signals are amplified
¹⁵⁷⁴ and then sent to the Constant Fraction Discriminator (CFD) described in Figure 4.2. At the end of
¹⁵⁷⁵ the chain, 100 ns long pulses are sent in the LVDS output. These output signal are sent on one side to
¹⁵⁷⁶ a V1190A Time-to-Digital Converter (TDC) module from CAEN and on the other to an OR module
¹⁵⁷⁷ to count the number of detected signals. Trigger and hit coïncidences are monitored using scalers.
¹⁵⁷⁸ The TDC is used to store the data into ROOT files. These files are thus analysed to understand the
¹⁵⁷⁹ detectors performance.

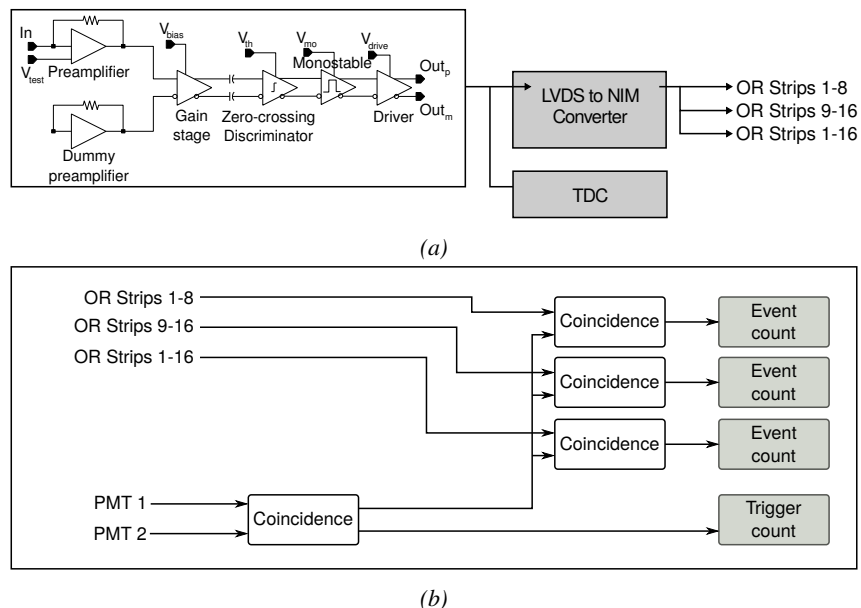


Figure 4.1: Signals from the RPC strips are shaped by the FEE described on Figure 4.1a. Output LVDS signals are then read-out by a TDC module connected to a computer or converted into NIM and sent to scalers. Figure 4.1b describes how these converted signals are put in coincidence with the trigger.

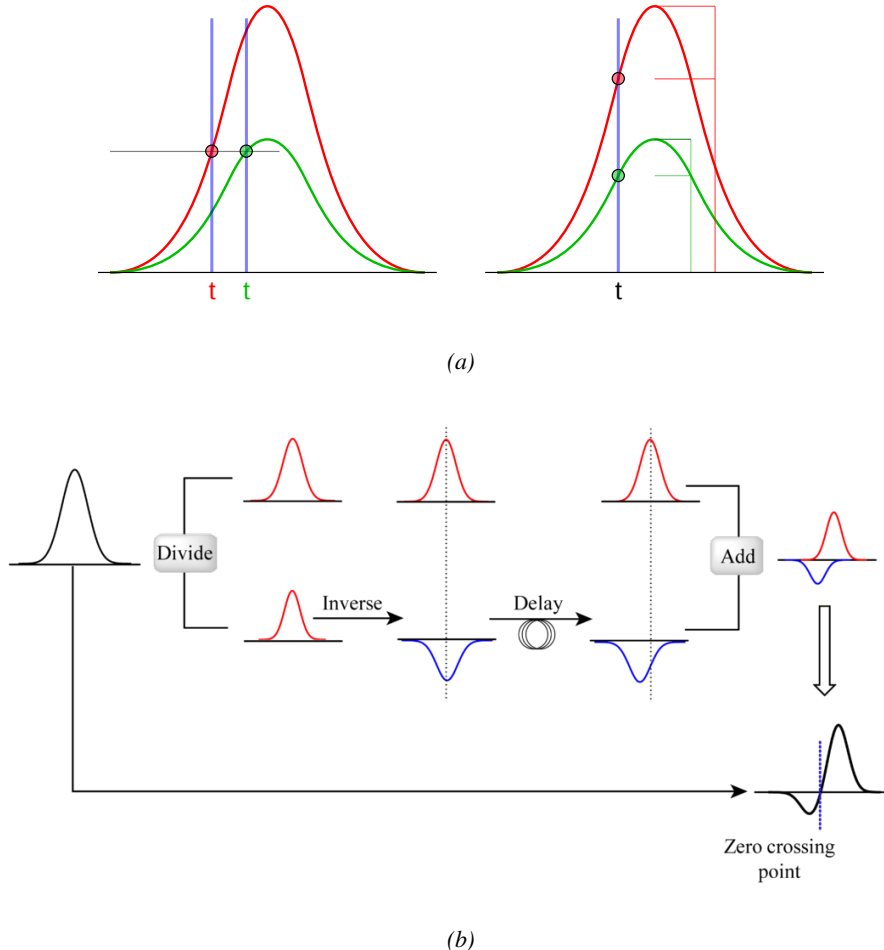


Figure 4.2: Description of the principle of a CFD. A comparison of threshold triggering (left) and constant fraction triggering (right) is shown in Figure 4.2a. Constant fraction triggering is obtained thanks to zero-crossing technique as explained in Figure 4.2b. The signal arriving at the input of the CFD is split into three components. A first one is delayed and connected to the inverting input of a first comparator. A second component is connected to the noninverting input of this first comparator. A third component is connected to the noninverting input of another comparator along with a threshold value connected to the inverting input. Finally, the output of both comparators is fed through an AND gate.

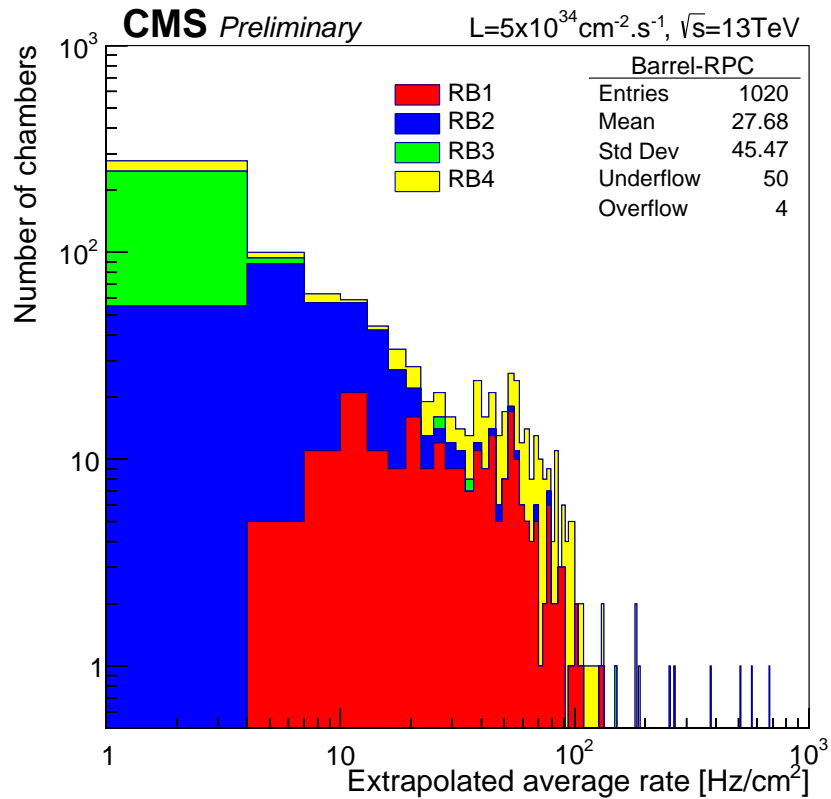
1580 4.2 Testing detectors under extreme conditions

1581 The upgrade from LHC to HL-LHC will increase the peak luminosity from $10^{34} \text{ cm}^{-2} \text{ s}^{-1}$ to reach
 1582 $5 \times 10^{34} \text{ cm}^{-2} \text{ s}^{-1}$, increasing in the same way the total expected background to which the RPC
 1583 system will be subjected to. Composed of low energy gammas and neutrons from $p\text{-}p$ collisions, low
 1584 momentum primary and secondary muons, puch-through hadrons from calorimeters, and particles
 1585 produced in the interaction of the beams with collimators, the background will mostly affect the
 1586 regions of CMS that are the closest to the beam line, i.e. the RPC detectors located in the endcaps.
 1587 [To update.]

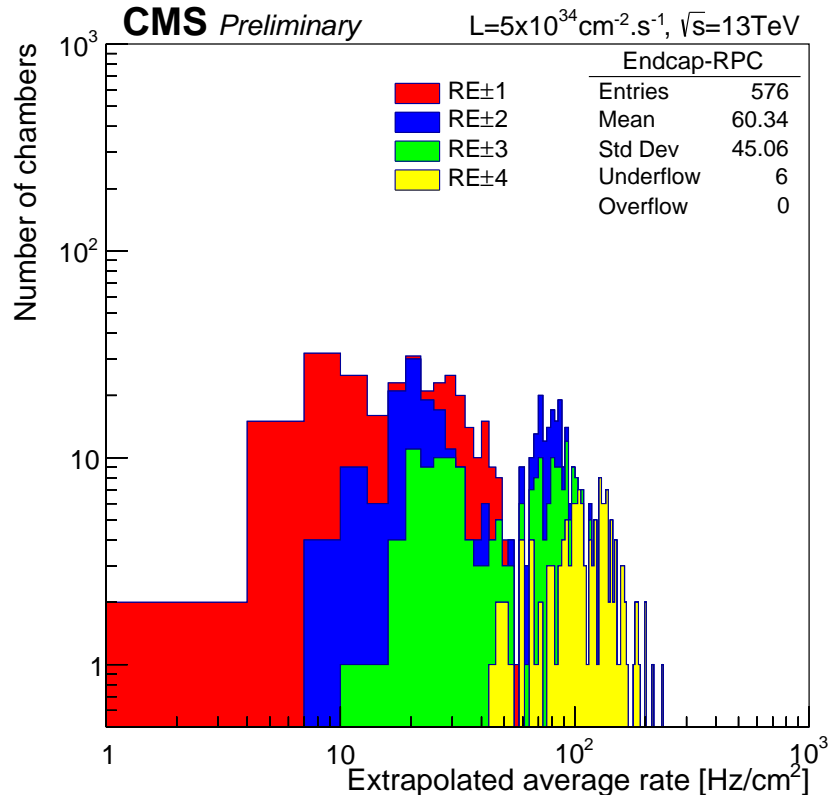
1588

1589 The 2016 data allowed to study the values of the background rate in all RPC system. In Fig-
1590 ure 4.3, the distribution of the chamber background hit rate per unit area is shown at a luminosity
1591 of $5 \times 10^{34} cm^{-2}.s^{-1}$ linearly extrapolating from data collected in 2016 [ref mentioning the linear
1592 dependency of rate vs lumi]. The maximum rate per unit area at HL-LHC conditions is expected to
1593 be of the order of $600 Hz/cm^2$ (including a safety factor 3). Nevertheless, Fluka simulations have
1594 conducted in order to understand the background at HL-LHC conditions. The comparison to the
1595 data has shown, in Figure 4.4, a discrepancy of a factor 2 even though the order of magnitude is
1596 consistent. [Understand mismatch.]

1597



(a)



(b)

Figure 4.3: (4.3a) Extrapolation from 2016 data of single hit rate per unit area in the barrel region. (4.3b) Extrapolation from 2016 data of single hit rate per unit area in the endcap region.

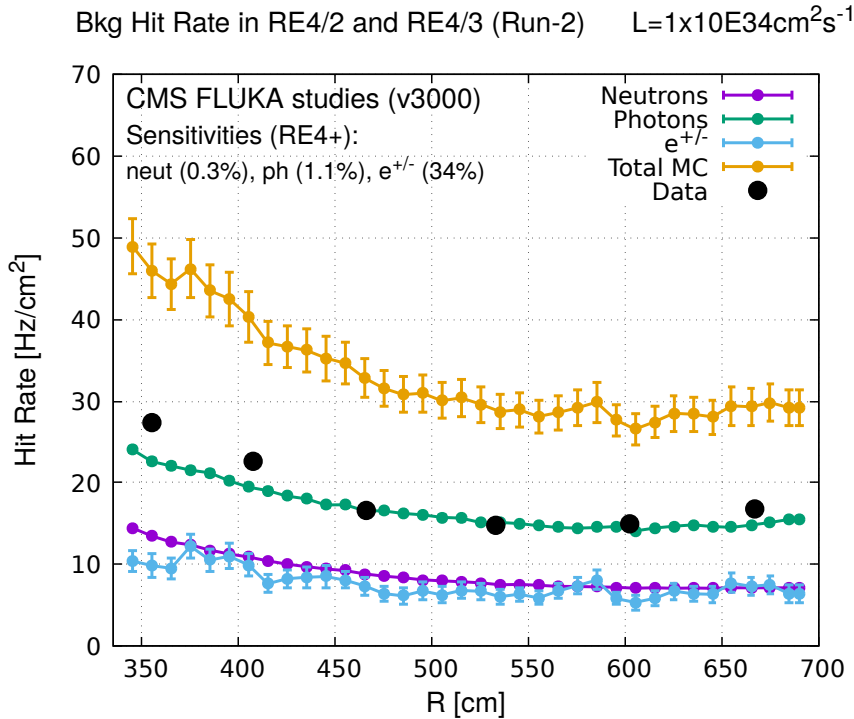


Figure 4.4: Background Fluka simulation compared to 2016 Data at $L = 10^{34} \text{ cm}^{-2} \cdot \text{s}^{-1}$ in the fourth endcap disk region. A mismatch in between simulation and data can be observed. [\[To be understood.\]](#)

1598 In the past, extensive long-term tests were carried out at several gamma and neutron facilities
 1599 certifying the detector performance. Both full size and small prototype RPCs have been irradiated
 1600 with photons up to an integrated charge of $\sim 0.05 \text{ C/cm}^2$ and $\sim 0.4 \text{ C/cm}^2$, respectively [53, 54].
 1601 During Run-I, the RPC system provided stable operation and excellent performance and did not
 1602 show any aging effects for integrated charge of the order of 0.01 C/cm^2 . Projections on currents
 1603 from 2016 Data, has allowed to determine that the total integrated charge, by the end of HL-LHC,
 1604 would be of the order of 1 C/cm^2 (including a safety factor 3). [\[Corresponding figure needed.\]](#)
 1605

1606 4.2.1 The Gamma Irradiation Facilities

1607 4.2.1.1 GIF

1608 Located in the SPS West Area at the downstream end of the X5 test beam, the Gamma Irradiation
 1609 Facility (GIF) was a test area in which particle detectors were exposed to a particle beam in presence
 1610 of an adjustable gamma background [55]. Its goal was to reproduce background conditions these
 1611 detectors would suffer in their operating environment at LHC. GIF layout is shown in Figure 4.5.
 1612 Gamma photons are produced by a strong ^{137}Cs source installed in the upstream part of the zone
 1613 inside a lead container. The source container includes a collimator, designed to irradiate a $6 \times 6 \text{ m}^2$
 1614 area at 5 m maximum to the source. A thin lens-shaped lead filter helps providing with a uniform
 1615 outcoming flux in a vertical plane, orthogonal to the beam direction. The principal collimator hole
 1616 provides a pyramidal aperture of $74^\circ \times 74^\circ$ solid angle and provides a photon flux in a pyramidal vol-

ume along the beam axis. The photon rate is controled by further lead filters allowing the maximum rate to be limited and to vary within a range of four orders of magnitude. Particle detectors under test are then placed within the pyramidal volume in front of the source, perpendicularly to the beam line in order to profit from the homogeneous photon flux. Adjusting the background flux of photons can then be done by using the filters and choosing the position of the detectors with respect to the source.

1622

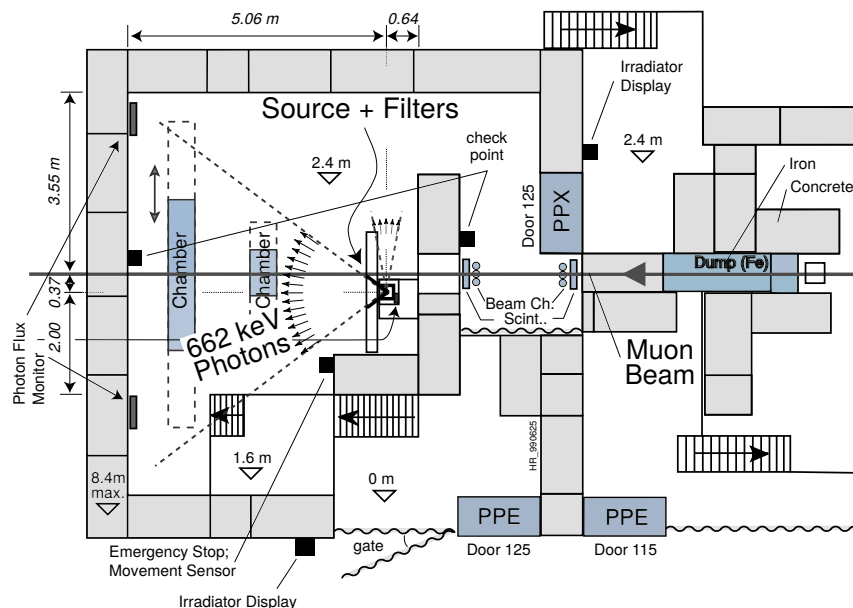


Figure 4.5: Layout of the test beam zone called X5c GIF at CERN. Photons from the radioactive source produce a sustained high rate of random hits over the whole area. The zone is surrounded by 8 m high and 80 cm thick concrete walls. Access is possible through three entry points. Two access doors for personnel and one large gate for material. A crane allows installation of heavy equipment in the area.

As described on Figure 4.6, the ^{137}Cs source emits a 662 keV photon in 85% of the decays. An activity of 740 GBq was measured on the 5th March 1997. To estimate the strength of the flux in 2014, it is necessary to consider the nuclear decay through time assiciated to the Cesium source whose half-life is well known ($t_{1/2} = (30.05 \pm 0.08)$ y). The GIF tests where done in between the 20th and the 31st of August 2014, i.e. at a time $t = (17.47 \pm 0.02)$ y resulting in an attenuation of the activity from 740 GBq in 1997 to 494 GBq in 2014.

1629

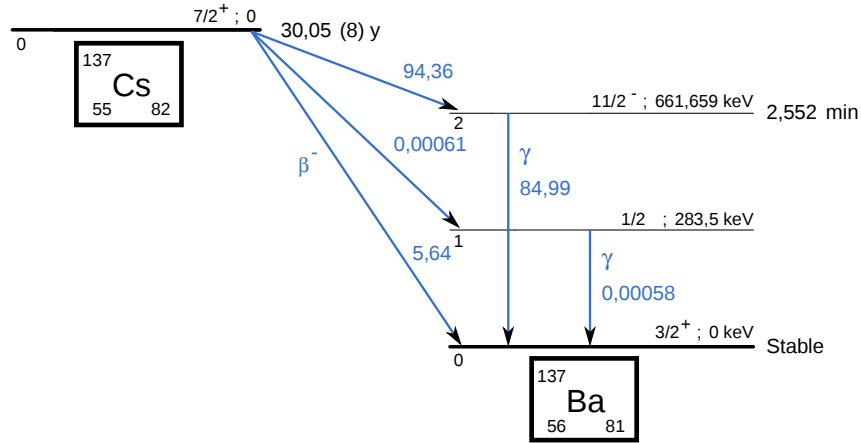


Figure 4.6: ^{137}Cs decays by β^- emission to the ground state of ^{137}Ba ($\text{BR} = 5.64\%$) and via the 662 keV isomeric level of ^{137}Ba ($\text{BR} = 94.36\%$) whose half-life is 2.55 min.

1630 4.2.1.2 GIF++

1631 The new Gamma Irradiation Facility (GIF++), located in the SPS North Area at the downstream end
 1632 of the H4 test beam, has replaced its predecessor during LS1 and has been operational since spring
 1633 2015 [56]. Like GIF, GIF++ features a ^{137}Cs source of 662 keV gamma photons, their fluence being
 1634 controlled with a set of filters of various attenuation factors. The source provides two separated large
 1635 irradiation areas for testing several full-size muon detectors with continuous homogeneous irradiation,
 1636 as presented in Figure 4.7.

1637

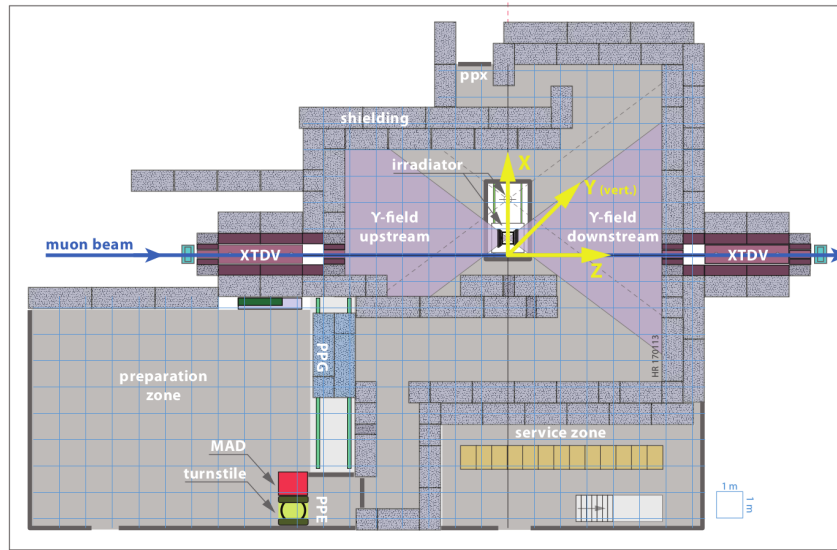


Figure 4.7: Floor plan of the GIF++ facility. When the facility downstream of the GIF++ takes electron beam, a beam pipe is installed along the beam line (z -axis). The irradiator can be displaced laterally (its center moves from $x = 0.65 \text{ m}$ to 2.15 m), to increase the distance to the beam pipe.

1638 The source activity was measured to be about 13.5 TBq in March 2016. The photon flux being
 1639 far greater than HL-LHC expectations, GIF++ provides an excellent facility for accelerated aging
 1640 tests of muon detectors.

1641

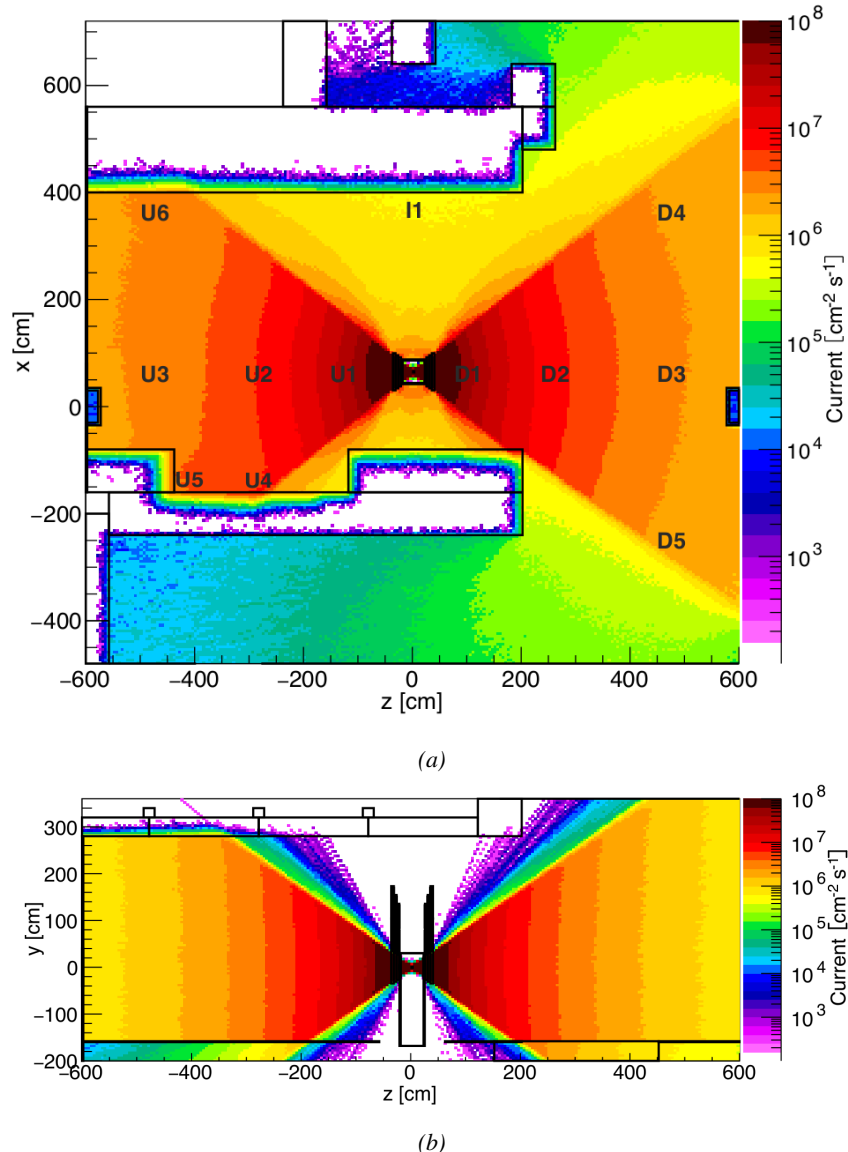


Figure 4.8: Simulated unattenuated current of photons in the xz plane (Figure 4.8a) and yz plane (Figure 4.8b) through the source at $x = 0.65$ m and $y = 0$ m. With angular correction filters, the current of 662 keV photons is made uniform in xy planes.

1642
 1643
 1644

The source is situated in the muon beam line with the muon beam being available a few times a year. The H4 beam, composed of muons with a momentum of about 150 GeV/c, passes through the GIF++ zone and is used to study the performance of the detectors. Its flux is of 104 particles/s/cm²

1645 focused in an area similar to $10 \times 10 \text{ cm}^2$. Therefore, with properly adjusted filters, one can imitate
 1646 the HL-LHC background and study the performance of muon detectors with their trigger/readout
 1647 electronics in HL-LHC environment.

1648

1649 4.3 Preliminary tests at GIF

1650 4.3.1 Resistive Plate Chamber test setup

1651 During summer 2014, preliminary tests have been conducted in the GIF area on a newly produced
 1652 RE4/2 chamber labelled RE-4-2-BARC-161. This chamber has been placed into a trolley covered
 1653 with a tent. The position of the RPC inside the tent and of the tent related to the source is described
 1654 in Figure 4.9. To test this CMS RPC, three different absorber settings were used. First of all,
 1655 measurements were done with fully opened source. Then, to complete this preliminary study, the
 1656 gamma flux has been attenuated from a factor 2 and a factor 5. The expected gamma flux at the level
 1657 of our detector will be discussed in subsection ??.

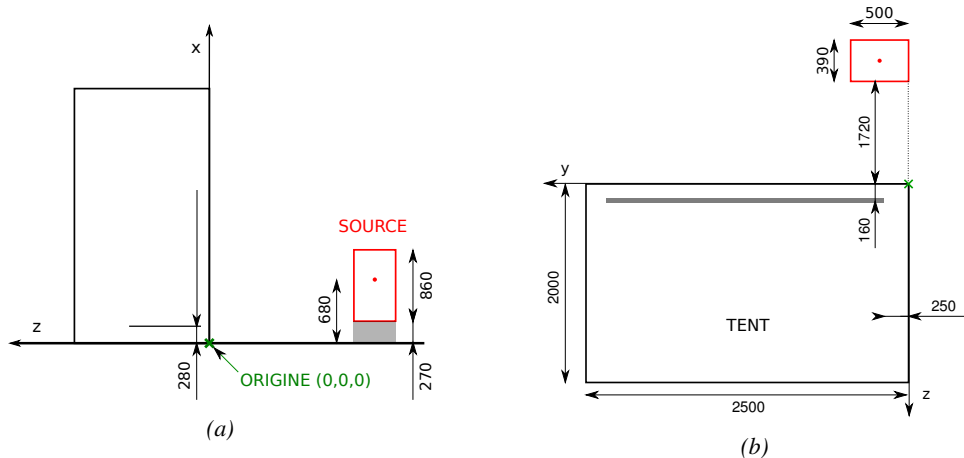


Figure 4.9: Description of the RPC setup. Dimensions are given in mm. A tent containing RPCs is placed at 1720 mm from the source container. The source is situated in the center of the container. RE-4-2-BARC-161 chamber is 160 mm inside the tent. This way, the distance between the source and the chambers plan is 2060 mm. Figure 4.9a provides a side view of the setup in the xz plane while Figure 4.9b shows a top view in the yz plane.



Figure 4.10: RE-4-2-BARC-I61 chamber is inside the tent as described in Figure 4.9. In the top right, the two scintillators used as trigger can be seen. This trigger system has an inclination of 10° relative to horizontal and is placed above half-partition B2 of the RPCs. PMT electronics are shielded thanks to lead blocks placed in order to protect them without stopping photons from going through the scintillators and the chamber.

1658 At the time of the tests, the beam not being operational anymore, a trigger composed of 2 plastic
 1659 scintillators has been placed in front of the setup with an inclination of 10 deg with respect to the
 1660 detector plane in order to look at cosmic muons. Using this particular trigger layout, shown on Fig-
 1661 ure 4.10, leads to a cosmic muon hit distribution into the chamber similar to the one in Figure 4.11.
 1662 Measured without gamma irradiation, two peaks can be seen on the profile of partition B, centered
 1663 on strips 52 and 59. Section ?? will help us understand that these two peaks are due respectively to
 1664 forward and backward coming cosmic particles where forward coming particles are first detected by
 1665 the scintillators and then the RPC while the backward coming muons are first detected in the RPC.

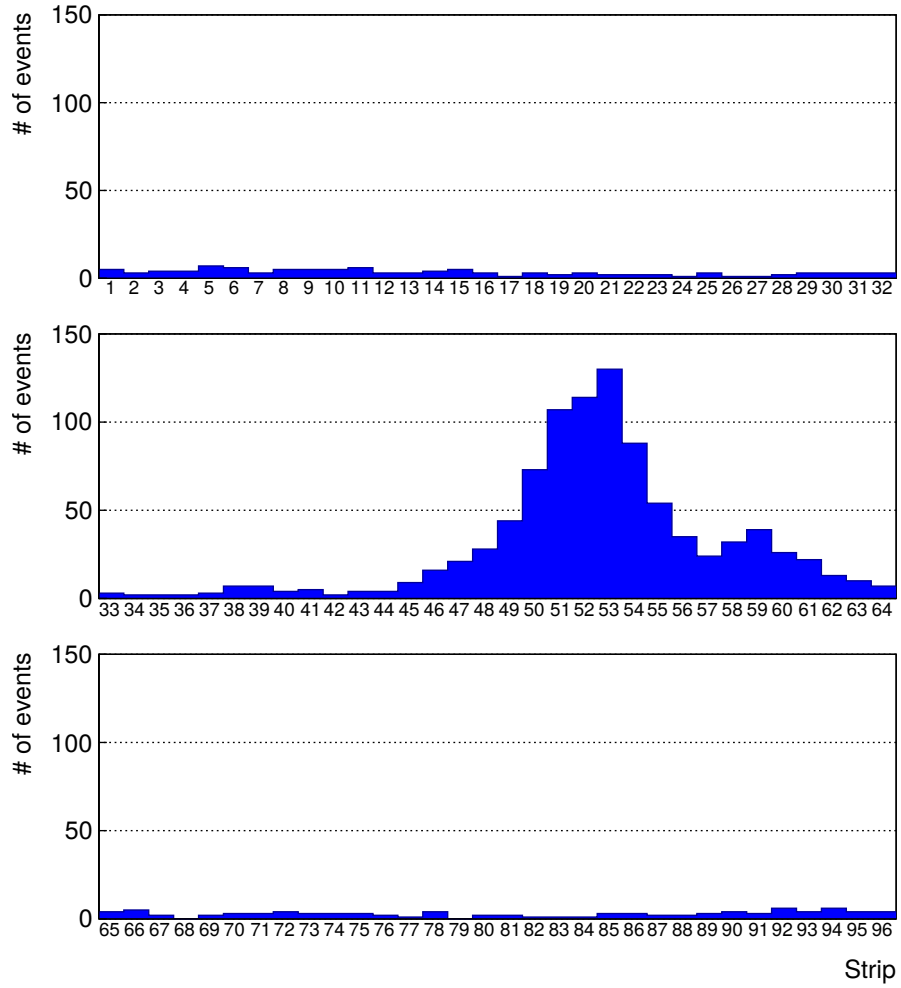


Figure 4.11: Hit distributions over all 3 partitions of RE-4-2-BARC-161 chamber is showed on these plots. Top, middle and bottom figures respectively correspond to partitions A, B, and C. These plots show that some events still occur in other half-partitions than B2, which corresponds to strips 49 to 64, in front of which the trigger is placed, contributing to the inefficiency of detection of cosmic muons. In the case of partitions A and C, the very low amount of data can be interpreted as noise. On the other hand, it is clear that a little portion of muons reach the half-partition B1, corresponding to strips 33 to 48.

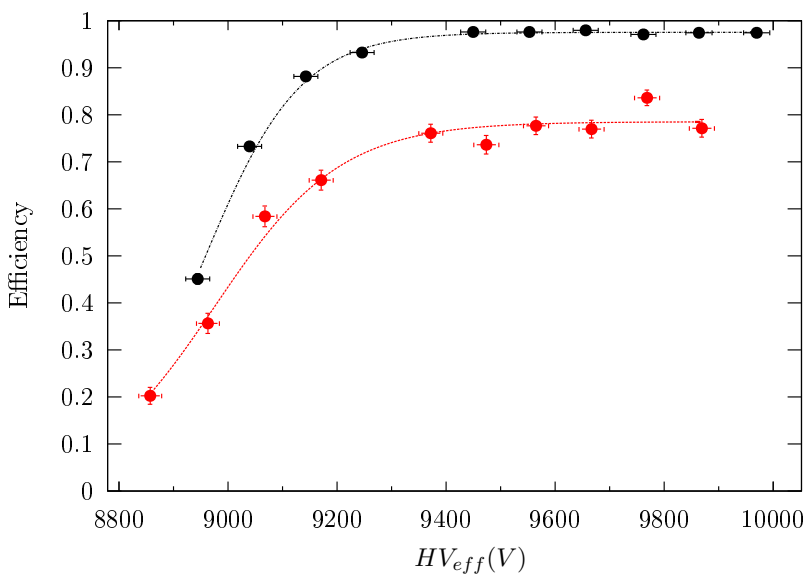
4.3.2 Data Acquisition

4.3.3 Geometrical acceptance of the setup layout to cosmic muons

In order to profit from a constant gamma irradiation, the detectors inside of the GIF bunker need to be placed in a plane orthogonal to the beam line. The muon beam that used to be available was meant to test the performance of detectors under test. This beam not being active anymore, another solution to test detector performance had to be used. Thus, it has been decided to use cosmic muons detected through a telescope composed of two scintillators. Lead blocks were used as shielding to

1673 protect the photomultipliers from gammas as can be seen from Figure 4.10.

1674 An inclination has been given to the cosmic telescope to maximize the muon flux. A good com-
 1675 promise had to be found between good enough muon flux and narrow enough hit distribution to
 1676 be sure to contain all the events into only one half partitions as required from the limited available
 1677 readout hardware. Nevertheless, a consequence of the misplaced trigger, that can be seen as a loss
 1678 of events in half-partition B1 in Figure 4.11, is an inefficiency. Nevertheless, the inefficiency of ap-
 1679 proximately 20 % highlighted in Figure 4.12 by comparing the performance of chamber BARC-161
 1680 in 904 and at GIF without irradiation seems too important to be explained only by the geometri-
 1681 cal acceptance of the setup itself. Simulations have been conducted to show how the setup brings
 1682 inefficiency.



1683 *Figure 4.12: Results are derived from data taken on half-partition B2 only. On the 18th of June 2014, data
 1684 has been taken on chamber RE-2-BARC-161 at building 904 (Prevessin Site) with cosmic muons providing us a
 1685 reference efficiency plateau of $(97.54 \pm 0.15)\%$ represented by a black curve. A similar measurement has been
 1686 done at GIF on the 21st of July with the same chamber giving a plateau of $(78.52 \pm 0.94)\%$ represented by a
 1687 red curve.*

1688 4.3.3.1 Description of the simulation layout

1689 The layout of GIF setup has been reproduced and incorporated into a Monte Carlo (MC) simulation
 1690 to study the influence of the disposition of the telescope on the final distribution measured by the
 1691 RPC. A 3D view of the simulated layout is given into Figure 4.13. Muons are generated randomly
 1692 in a horizontal plane located at a height corresponding to the lowest point of the PMTs. This way,
 1693 the needed size of the plane in order to simulate events happening at very big azimuthal angles (i.e.
 $\theta \approx \pi$) can be kept relatively small. The muon flux is designed to follow the usual $\cos^2\theta$ distribution
 1694 for cosmic particle. The goal of the simulation is to look at muons that pass through the muon
 1695 telescope composed of the two scintillators and define their distribution onto the RPC plane. During
 1696 the reconstruction, the RPC plane is then divided into its strips and each muon track is assigned to a
 1697 strip.

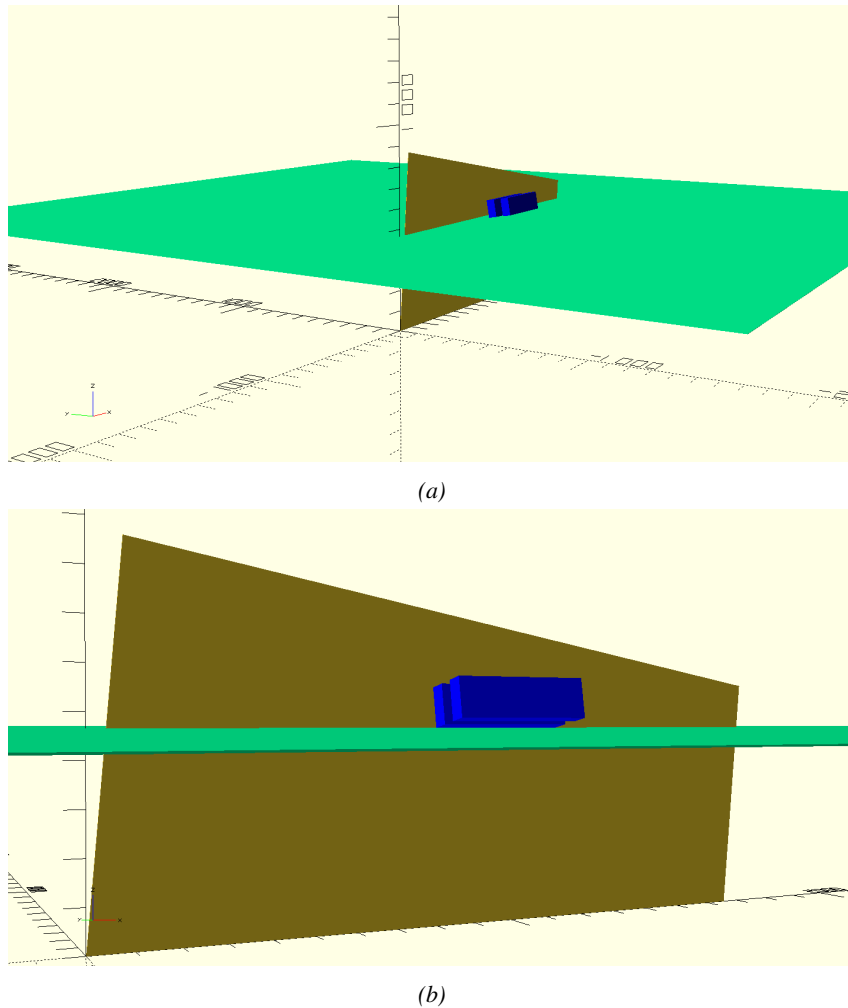


Figure 4.13: Representation of the layout used for the simulations of the test setup. The RPC is represented as a yellow trapezoid while the two scintillators as blue cuboids looking at the sky. A green plane corresponds to the muon generation plane within the simulation. Figure 4.9a shows a global view of the simulated setup. Figure 4.9b shows a zoomed view that allows to see the 2 scintillators as well as the full RPC plane.

1694 In order to further refine the quality of the simulation and understand deeper the results the
 1695 dependance of the distribution has been studied for a range of telescope inclinations. Moreover,
 1696 the threshold applied on the PMT signals has been included into the simulation in the form of a
 1697 cut. In the approximation of uniform scintillators, it has been considered that the threshold can be
 1698 understood as the minimum distance particles need to travel through the scintillating material to give
 1699 a strong enough signal. Particles that travel a distance smaller than the set "threshold" are thus not
 1700 detected by the telescope and cannot trigger the data taking. Finally, the FEE threshold also has
 1701 been considered in a similar way. The mean momentum of horizontal cosmic rays is higher than
 1702 those of vertical ones but the stopping power of matter for momenta ranging from 1 GeV to 1 TeV
 1703 stays comparable. It is then possible to assume that the mean number of primary e^-/ion pairs per
 1704 unit length will stay similar and thus, depending on the applied discriminator threshold, muons with

1705 the shortest path through the gas volume will deposit less charge and induce a smaller signal on the
 1706 pick-up strips that could eventually not be detected. These two thresholds also restrain the overall
 1707 geometrical acceptance of the system.

1708 4.3.3.2 Simulation procedure

1709 The simulation software has been designed using C++ and the output data is saved into ROOT
 1710 histograms. Simulations start for a threshold T_{scint} varying in a range from 0 to 45 mm in steps
 1711 of 5 mm, where $T_{scint} = 0$ mm corresponds to the case where there isn't any threshold apply on
 1712 the input signal while $T_{scint} = 45$ mm, which is the scintillator thickness, is the case where muons
 1713 cannot arrive orthogonally onto the scintillator surface. For a given T_{scint} , a set of RPC thresholds
 1714 are considered. The RPC threshold, T_{RPC} varies from 2 mm, the thickness of the gas volume, to
 1715 3 mm in steps of 0.25 mm. For each $(T_{scint}; T_{RPC})$ pair, $N_\mu = 10^8$ muons are randomly generated
 1716 inside the muon plane described in the previous paragraph with an azimuthal angle θ chosen to follow
 1717 a $\cos^2\theta$ distribution.

1718 Planes are associated to each surface of the scintillators. Knowing muon position into the muon
 1719 plane and its direction allows us, by assuming that muons travel in a straight line, to compute the
 1720 intersection of the muon track with these planes. Applying conditions to the limits of the surfaces
 1721 of the scintillator faces then gives us an answer to whether or not the muon passed through the
 1722 scintillators. In the case the muon has indeed passed through the telescope, the path through each
 1723 scintillator is computed and muons whose path was shorter than T_{scint} are rejected and are thus
 1724 considered as having not interacted with the setup.

1725 On the contrary, if the muon is labeled as good, its position within the RPC plane is computed
 1726 and the corresponding strip, determined by geometrical tests in the case the distance through the
 1727 gas volume was enough not to be rejected because of T_{RPC} , gets a hit and several histograms
 1728 are filled in order to keep track of the generation point on the muon plane, the intersection points
 1729 of the reconstructed muons within the telescope, or on the RPC plane, the path traveled through
 1730 each individual scintillator or the gas volume, as well as other histograms. Moreover, muons fill
 1731 different histograms whether they are forward or backward coming muons. They are discriminated
 1732 according to their direction components. When a muon is generated, an (x, y, z) position is assigned
 1733 into the muon plane as well as a $(\theta; \phi)$ pair that gives us the direction it's coming from. This way,
 1734 muons satisfying the condition $0 \leq \phi < \pi$ are designated as backward coming muons while muons
 1735 satisfying $\pi \leq \phi < 2\pi$ as forward coming muons.

1736 This simulation is then repeated for different telescope inclinations ranging in between 4 and 20°
 1737 and varying in steps of 2° . Due to this inclination and to the vertical position of the detector under
 1738 test, the muon distribution reconstructed in the detector plane is asymmetrical. The choice as been
 1739 made to chose a skew distribution formula to fit the data built as the multiplication of gaussian and
 1740 sigmoidal curves together. A typical gaussian formula is given as 4.1 and has three free parameters
 1741 as A_g , its amplitude, \bar{x} , its mean value and σ , its root mean square. Sigmoidal curves as given by
 1742 formula 4.2 are functions converging to 0 and A_s as x diverges. The inflection point is given as x_i
 1743 and λ is proportional to the slope at $x = x_i$. In the limit where $\lambda \rightarrow \infty$, the sigmoid becomes a
 1744 step function.

$$g(x) = A_g e^{-\frac{(x-\bar{x})^2}{2\sigma^2}} \quad (4.1)$$

$$s(x) = \frac{A_s}{1 + e^{-\lambda(x-x_i)}} \quad (4.2)$$

Finally, a possible representation of a skew distribution is given by formula 4.3 and is the product of 4.1 and 4.2. Naturally, here $A_{sk} = A_g \times A_s$ and represents the theoretical maximum in the limit where the skew tends to a gaussian function.

$$sk(x) = g(x) \times s(x) = A_{sk} \frac{e^{\frac{-(x-\bar{x})^2}{2\sigma^2}}}{1 + e^{-\lambda(x-x_i)}} \quad (4.3)$$

4.3.3.3 Results

Influence of T_{scint} on the muon distribution

Influence of T_{RPC} on the muon distribution

Influence of the telescope inclination on the muon distribution

Comparison to data taken at GIF without irradiation

4.3.4 Photon flux at GIF

4.3.4.1 Expectations from simulations

In order to understand and evaluate the γ flux in the GIF area, simulations had been conducted in 1999 and published by S. Agosteo et al [55]. Table 4.1 presented in this article gives us the γ flux for different distances D to the source. This simulation was done using GEANT and a Monte Carlo N-Particle (MCNP) transport code, and the flux F is given in number of γ per unit area and unit time along with the estimated error from these packages expressed in %.

Nominal ABS	Photon flux F [$s^{-1}cm^{-2}$]			
	at $D = 50$ cm	at $D = 155$ cm	at $D = 300$ cm	at $D = 400$ cm
1	$0.12 \cdot 10^8 \pm 0.2\%$	$0.14 \cdot 10^7 \pm 0.5\%$	$0.45 \cdot 10^6 \pm 0.5\%$	$0.28 \cdot 10^6 \pm 0.5\%$
2	$0.68 \cdot 10^7 \pm 0.3\%$	$0.80 \cdot 10^6 \pm 0.8\%$	$0.25 \cdot 10^6 \pm 0.8\%$	$0.16 \cdot 10^6 \pm 0.6\%$
5	$0.31 \cdot 10^7 \pm 0.4\%$	$0.36 \cdot 10^6 \pm 1.2\%$	$0.11 \cdot 10^6 \pm 1.2\%$	$0.70 \cdot 10^5 \pm 0.9\%$

Table 4.1: Total photon flux ($E\gamma \leq 662$ keV) with statistical error predicted considering a ^{137}Cs activity of 740 GBq at different values of the distance D to the source along the x -axis of irradiation field [55].

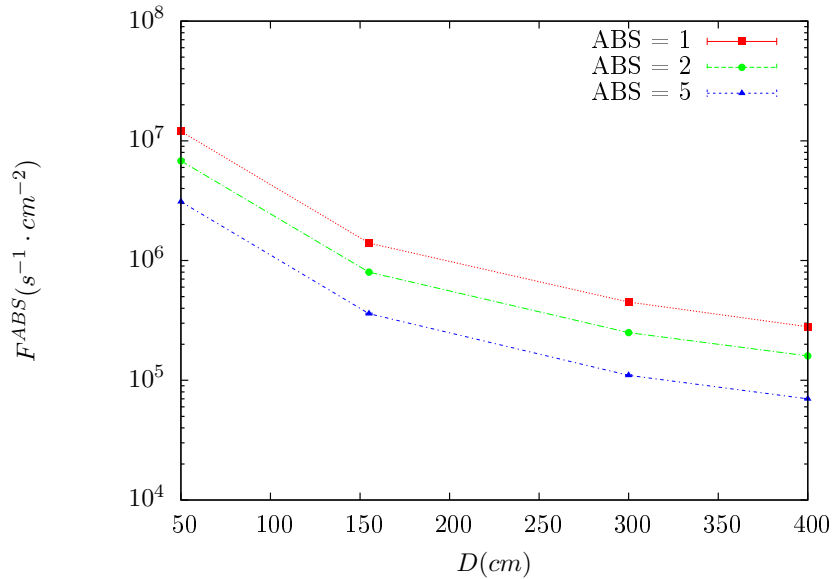


Figure 4.14: γ flux $F(D)$ is plot using values from table 4.1. As expected, the plot shows similar attenuation behaviours with increasing distance for each absorption factors.

The simulation doesn't directly provides us with an estimated flux at the level of our RPC. First of all, it is needed to extract the value of the flux from the available data contained in the original paper and then to estimate the flux in 2014 at the time the experimentation took place. Figure 4.14 that contains the data from Table 4.1. In the case of a pointlike source emitting isotropic and homogeneous gamma radiations, the gamma flux F at a distance D to the source with respect to a reference point situated at D_0 where a known flux F_0 is measured will be expressed like in Equation 4.4, assuming that the flux decreases as $1/D^2$, where c is a fitting factor.

$$F^{ABS} = F_0^{ABS} \times \left(\frac{cD_0}{D} \right)^2 \quad (4.4)$$

By rewriting Equation 4.4, it comes that :

$$c = \frac{D}{D_0} \sqrt{\frac{F^{ABS}}{F_0^{ABS}}} \quad (4.5)$$

$$\Delta c = \frac{c}{2} \left(\frac{\Delta F^{ABS}}{F^{ABS}} + \frac{\Delta F_0^{ABS}}{F_0^{ABS}} \right) \quad (4.6)$$

Finally, using Equation 4.5 and the data in Table 4.1 with $D_0 = 50$ cm as reference point, we can build Table 4.2. It is interesting to note that c for each value of D doesn't depend on the absorption factor.

Nominal ABS	Correction factor c		
	at $D = 155$ cm	at $D = 300$ cm	at $D = 400$ cm
1	$1.059 \pm 0.70\%$	$1.162 \pm 0.70\%$	$1.222 \pm 0.70\%$
2	$1.063 \pm 1.10\%$	$1.150 \pm 1.10\%$	$1.227 \pm 0.90\%$
5	$1.056 \pm 1.60\%$	$1.130 \pm 1.60\%$	$1.202 \pm 1.30\%$

Table 4.2: Correction factor c is computed thanks to formulae 4.5 taking as reference $D_0 = 50$ cm and the associated flux F_0^{ABS} for each absorption factor available in table 4.1.

1771 For the range of D/D_0 values available, it is possible to use a simple linear fit to get the evolution
 1772 of c . The linear fit will then use only 2 free parameters, a and b , as written in Equation 4.7. This gives
 1773 us the results showed in Figure 4.15. Figure 4.15b confirms that using only a linear fit to extract c is
 1774 enough as the evolution of the rate that can be obtained superimposes well on the simulation points.

$$c \left(\frac{D}{D_0} \right) = a \frac{D}{D_0} + b \quad (4.7)$$

$$F^{ABS} = F_0^{ABS} \left(a + \frac{bD_0}{D} \right)^2 \quad (4.8)$$

$$\Delta F^{ABS} = F^{ABS} \left[\frac{\Delta F_0^{ABS}}{F_0^{ABS}} + 2 \frac{\Delta a + \Delta b \frac{D_0}{D}}{a + \frac{bD_0}{D}} \right] \quad (4.9)$$

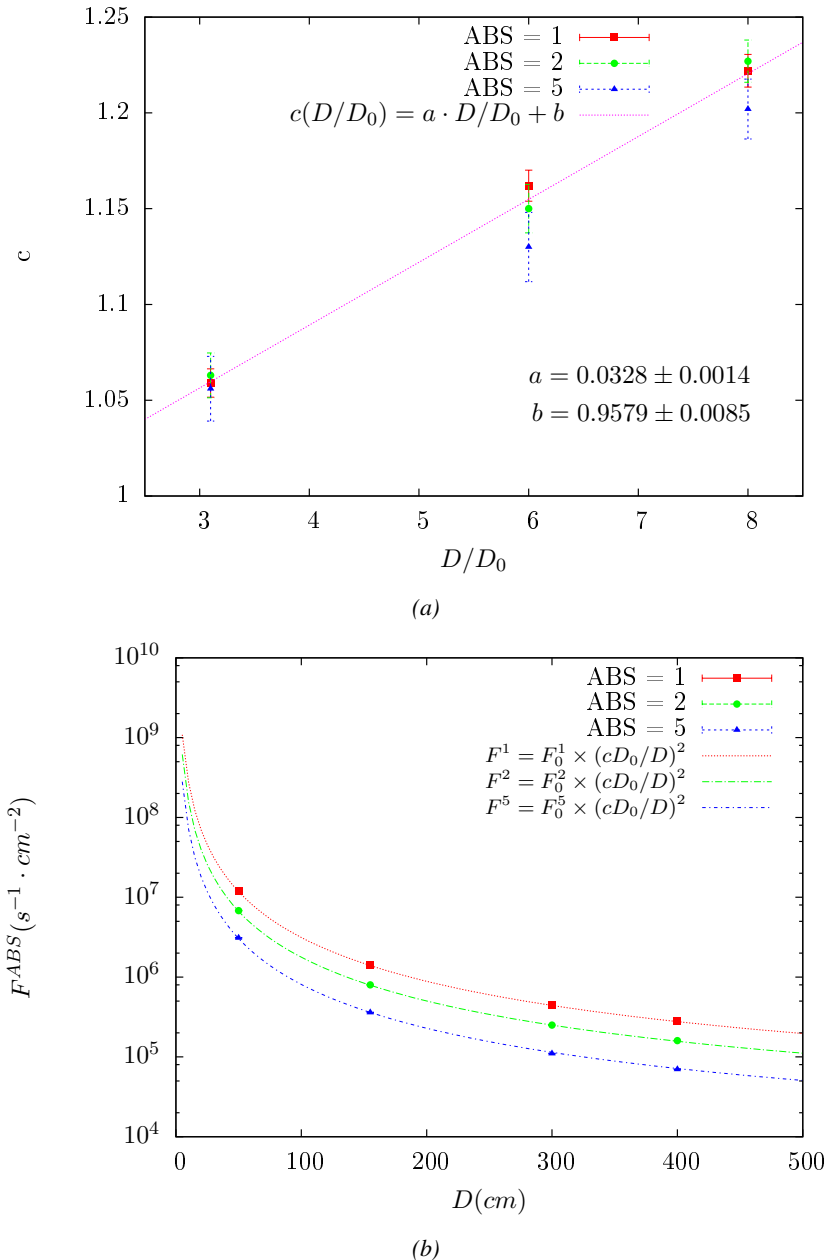


Figure 4.15: Figure 4.15a shows the linear approximation fit done via formulae 4.7 on data from table 4.2. Figure 4.15b shows a comparison of this model with the simulated flux using a and b given in figure 4.15a in formulae 4.4 and the reference value $D_0 = 50\text{cm}$ and the associated flux for each absorption factor F_0^{ABS} from table 4.1

In the case of the 2014 GIF tests, the RPC plane is located at a distance $D = 206\text{ cm}$ to the source. Moreover, to estimate the strength of the flux in 2014, it is necessary to consider the nuclear decay through time associated to the Cesium source whose half-life is well known ($t_{1/2} = (30.05 \pm 0.08)\text{ y}$). The very first source activity measurement has been done on the 5th of March 1997 while the GIF

1779 tests where done in between the 20th and the 31st of August 2014, i.e. at a time $t = (17.47 \pm 0.02)$ y
 1780 resulting in an attenuation of the activity from 740 GBq in 1997 to 494 GBq in 2014. All the needed
 1781 information to extrapolate the flux through our detector in 2014 has now been assembled, leading
 1782 to the Table 4.3. It is interesting to note that for a common RPC sensitivity to γ of $2 \cdot 10^{-3}$, the
 1783 order of magnitude of the estimated hit rate per unit area is of the order of the kHz for the fully
 1784 opened source. Moreover, taking profit of the two working absorbers, it will be possible to scan
 1785 background rates at 0 Hz, ~ 300 Hz as well as ~ 600 Hz. Without source, a good estimate of the
 1786 intrinsic performance will be available. Then at 300 Hz, the goal will be to show that the detectors
 1787 fulfill the performance certification of CMS RPCs. Then a first idea of the performance of the
 1788 detectors at higher background will be provided with absorption factors 2 (~ 600 Hz) and 1 (no
 1789 absorption). [Here I will also put a reference to the plot showing the estimated background rate at
 1790 the level of RE3/1 in the case of HL-LHC but this one being in another chapter, I will do it later.]

Nominal ABS	Photon flux F [$s^{-1}cm^{-2}$]			Hit rate/unit area [$Hz cm^{-2}$] at $D^{2014} = 206$ cm
	at $D_0^{1997} = 50$ cm	at $D^{1997} = 206$ cm	at $D^{2014} = 206$ cm	
1	$0.12 \cdot 10^8 \pm 0.2\%$	$0.84 \cdot 10^6 \pm 0.3\%$	$0.56 \cdot 10^6 \pm 0.3\%$	1129 ± 32
2	$0.68 \cdot 10^7 \pm 0.3\%$	$0.48 \cdot 10^6 \pm 0.3\%$	$0.32 \cdot 10^6 \pm 0.3\%$	640 ± 19
5	$0.31 \cdot 10^7 \pm 0.4\%$	$0.22 \cdot 10^6 \pm 0.3\%$	$0.15 \cdot 10^6 \pm 0.3\%$	292 ± 9

Table 4.3: The data at D_0 in 1997 is taken from [55]. In a second step, using Equations 4.8 and 4.9, the flux at D can be estimated in 1997. Then, taking into account the attenuation of the source activity, the flux at D can be estimated at the time of the tests in GIF in 2014. Finally, assuming a sensitivity of the RPC to γ $s = 2 \cdot 10^{-3}$, an estimation of the hit rate per unit area is obtained.

¹⁷⁹¹ **4.3.4.2 Dose measurements**

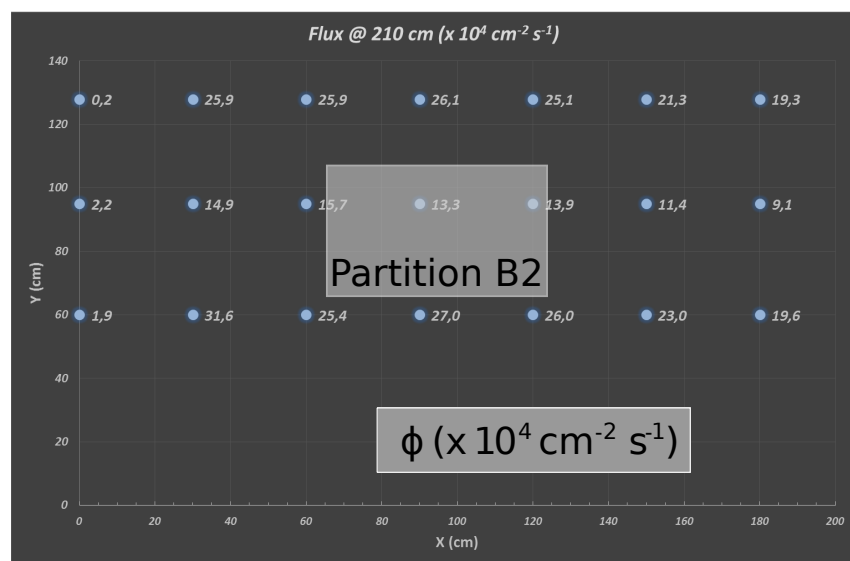


Figure 4.16: Dose measurements has been done in a plane corresponding to the tents front side. This plan is 1900 mm away from the source. As explained in the first chapter, a lens-shaped lead filter provides a uniform photon flux in the vertical plan orthogonal to the beam direction. If the second line of measured fluxes is not taken into account because of lower values due to experimental equipments in the way between the source and the tent, the uniformity of the flux is well showed by the results.

¹⁷⁹² **4.3.5 Results and discussions**

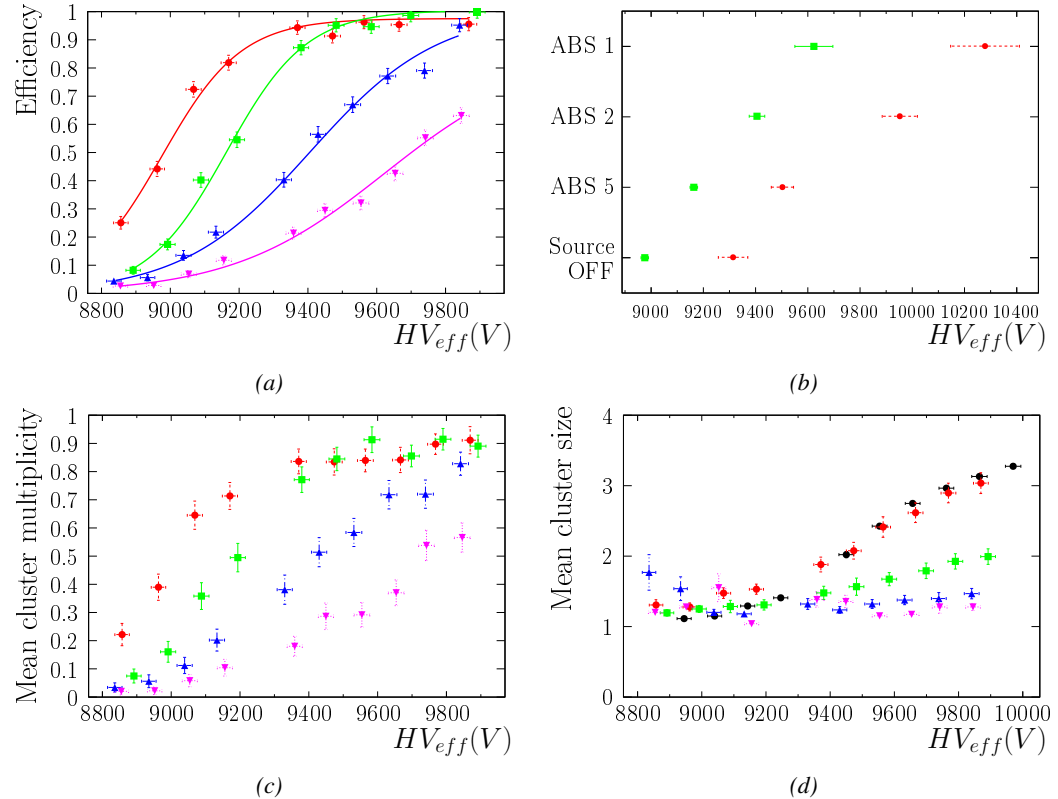


Figure 4.17

1793 4.4 Longevity tests at GIF++

1794 Longevity studies imply a monitoring of the performance of the detectors probed using a high inten-
1795 sity muon beam in a irradiated environment by periodically measuring their rate capability, the dark
1796 current running through them and the bulk resistivity of the Bakelite composing their electrodes.
1797 GIF++, with its very intense ^{137}Cs source, provides the perfect environment to perform such kind
1798 of tests. Assuming a maximum acceleration factor of 3, it is expected to accumulate the equivalent
1799 charge in 1.7 years.

1800 As the maximum background is found in the endcap, the choice naturally was made to focus the
1801 GIF++ longevity studies on endcap chambers. Most of the RPC system was installed in 2007. Nev-
1802 ertheless, the large chambers in the fourth endcap (RE4/2 and RE4/3) have been installed during
1803 LS1 in 2014. The Bakelite of these two different productions having different properties, four spare
1804 chambers of the present system were selected, two RE2,3/2 spares and two RE4/2 spares. Having
1805 two chambers of each type allows to always keep one of them non irradiated as reference, the per-
1806 formance evolution of the irradiated chamber being then compared through time to the performance
1807 of the non irradiated one.

1808 The performance of the detectors under different level of irradiation is measured periodically dur-
1809 ing dedicated test beam periods using the H4 muon beam. In between these test beam periods, the
1810 two RE2,3/2 and RE4/2 chambers selected for this study are irradiated by the ^{137}Cs source in order
1811 to accumulate charge and the gamma background is monitored, as well as the currents. The two
1812 remaining chambers are kept non-irradiated as reference detectors. Due to the limited gas flow in
1813 GIF++, the RE4 chamber remained non-irradiated until end of November 2016 where a new mass
1814 flow controller has been installed allowing for bigger volumes of gas to flow in the system.

1815 Figures 4.18 and 4.19 give us for different test beam periods, and thus for increasing integrated
1816 charge through time, a comparison of the maximum efficiency, obtained using a sigmoid-like func-
1817 tion, and of the working point of both irradiated and non irradiated chambers [**SIGMOID2005**]. No
1818 aging is yet to see from this data, the shifts in γ rate per unit area in between irradiated and non
1819 irradiated detectors and RE2 and RE4 types being easily explained by a difference of sensitivity due
1820 to the various Bakelite resistivities of the HPL electrodes used for the electrode production.

1821 Collecting performance data at each test beam period allows us to extrapolate the maximum effi-
1822 ciency for a background hit rate of $300\text{ Hz}/\text{cm}^2$ corresponding to the expected HL-LHC conditions.
1823 Aging effects could emerge from a loss of efficiency with increasing integrated charge over time,
1824 thus Figure 4.20 helps us understand such degradation of the performance of irradiated detectors in
1825 comparison with non irradiated ones. The final answer for an eventual loss of efficiency is given in
1826 Figure 4.21 by comparing for both irradiated and non irradiated detectors the efficiency sigmoids
1827 before and after the longevity study. Moreover, to complete the performance information, the Bake-
1828 lite resistivity is regularly measured thanks to Ag scans (Figure 4.22) and the noise rate is monitored
1829 weekly during irradiation periods (Figure 4.23). At the end of 2016, no signs of aging were observed
1830 and further investigation is needed to get closer to the final integrated charge requirements proposed
1831 for the longevity study of the present CMS RPC sub-system.

1832

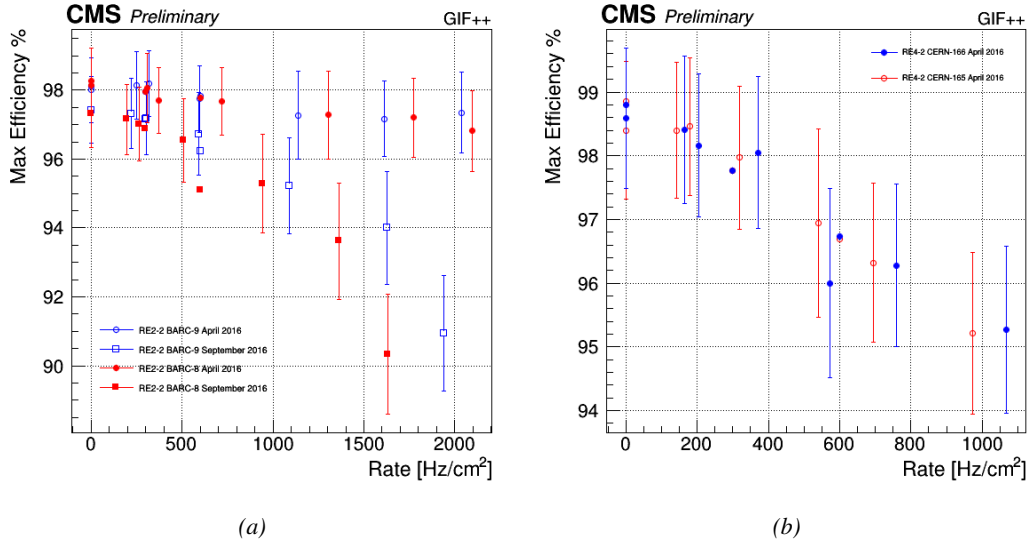


Figure 4.18: Evolution of the maximum efficiency for RE2 (4.18a) and RE4 (4.18b) chambers with increasing extrapolated γ rate per unit area at working point. Both irradiated (blue) and non irradiated (red) chambers are shown.

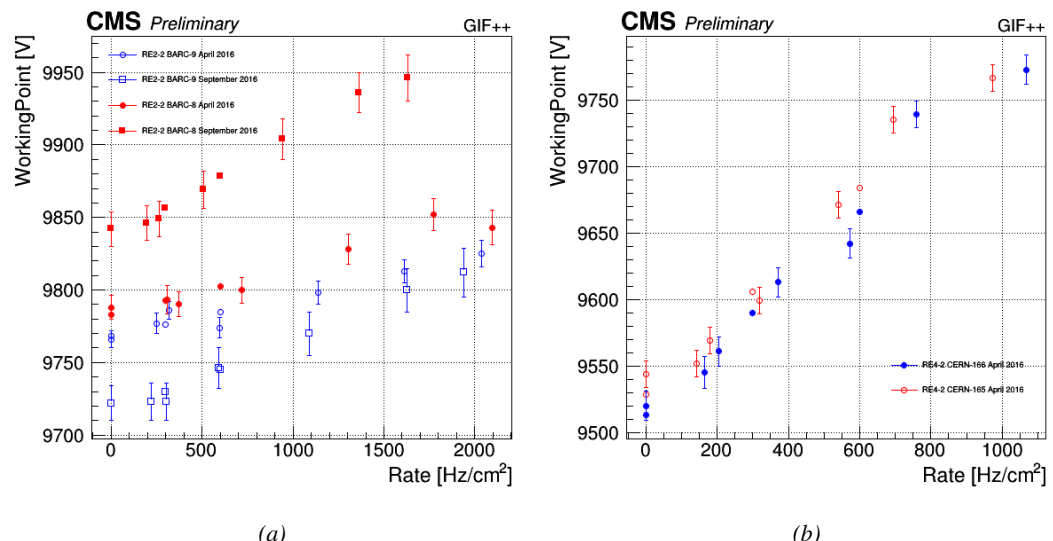


Figure 4.19: Evolution of the working point for RE2 (4.19a) and RE4 (4.19b) with increasing extrapolated γ rate per unit area at working point. Both irradiated (blue) and non irradiated (red) chambers are shown.

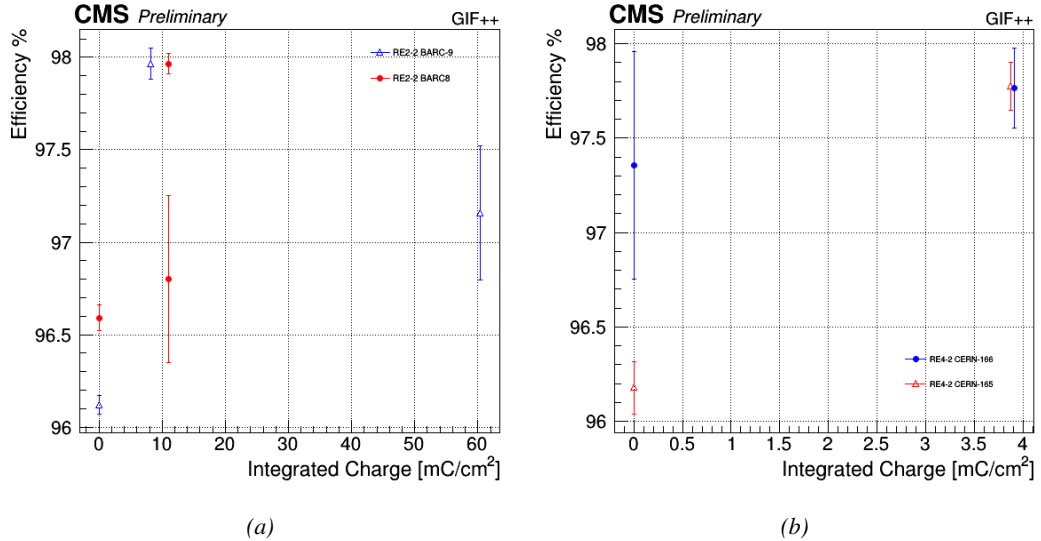


Figure 4.20: Evolution of the maximum efficiency at HL-LHC conditions, i.e. a background hit rate per unit area of 300 Hz/cm², with increasing integrated charge for RE2 (4.20a) and RE4 (4.20b) detectors. Both irradiated (blue) and non irradiated (red) chambers are shown. The integrated charge for non irradiated detectors is recorded during test beam periods and stays small with respect to the charge accumulated in irradiated chambers.

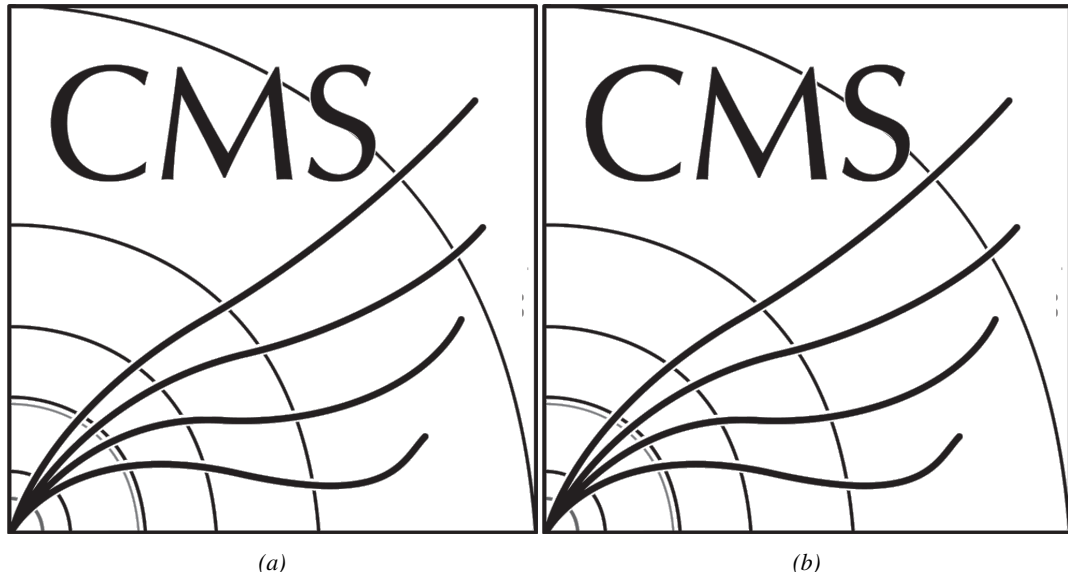


Figure 4.21: Comparison of the efficiency sigmoid before (triangles) and after (circles) irradiation for RE2 (4.21a) and RE4 (4.21b) detectors. Both irradiated (blue) and non irradiated (red) chambers are shown.

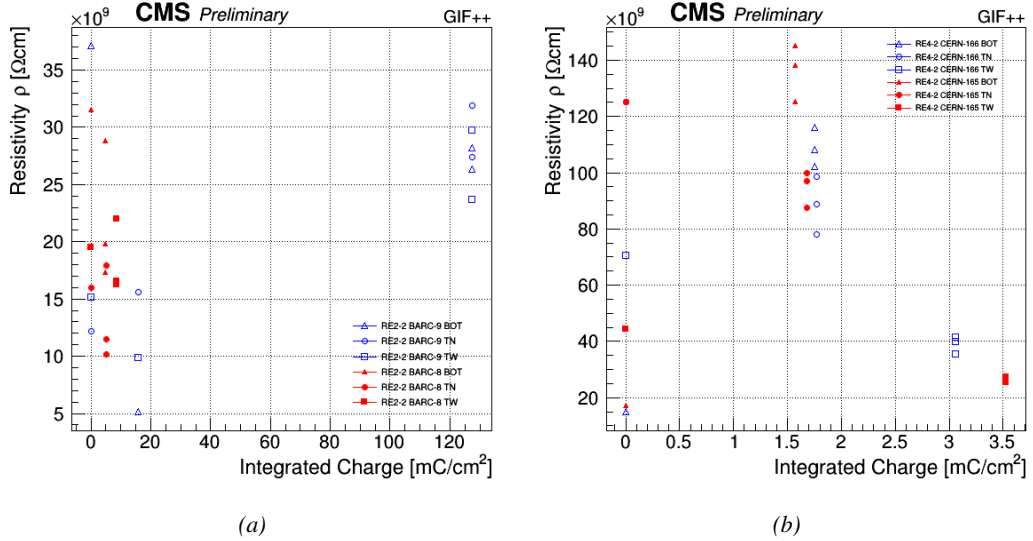


Figure 4.22: Evolution of the Bakelite resistivity for RE2 (4.22a) and RE4 (4.22b) detectors. Both irradiated (blue) and non-irradiated (red) chambers are shown.

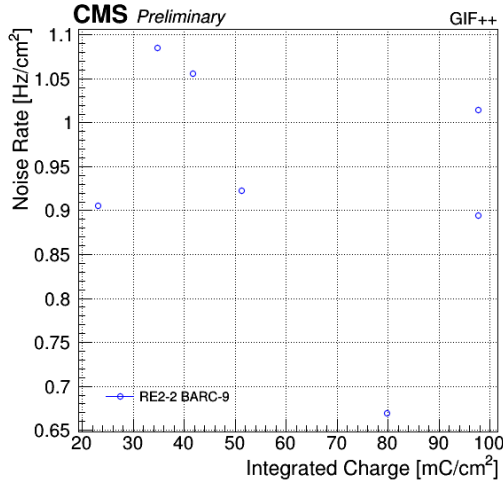


Figure 4.23: Evolution of the noise rate per unit area for the irradiated chamber RE2-2-BARC-9 only.

4.4.1 Description of the Data Acquisition

For the longevity studies, four spare chambers of the present system are used. Two spare RPCs of the RE2,3 stations as well as two spare RPCs from the new RE4 stations have been mounted in a Trolley. Six RE4 gaps are also placed in the trolley. The trolley is placed inside the GIFT++ in the upstream region of the bunker, taking the cesium source as a reference. The trolley is oriented for the detection surface of the chambers to be orthogonal to the beam line. The system can be moved along the orthogonal plane in order to have the beam in all η -partitions. For the aging the trolley is

1840 moved outside the beam line and is placed in a distance of 5.2 m to the source, which irradiates the
 1841 bunker using an attenuation filter of 2.2 which corresponds to a fluence of 10^7 gamma/cm^2 .

1842 During GIF++ operation, the data collected can be divided into different categories as several
 1843 parameters are monitored in addition to the usual RPC performance data. On one hand, to know
 1844 the performance of a chamber, it is need to measure its efficiency and to know the background
 1845 conditions in which it is operated. To do this, the hit signals from the chamber are recorded and
 1846 stored in a ROOT file via a Data Acquisition (DAQ) software. On the other hand, it is also very
 1847 important to monitor parameters such as environmental pressure and temperature, gas temperature
 1848 and humidity, RPC HV, LV, and currents, or even source and beam status. This is done through the
 1849 GIF++ web Detector Control Software (DCS) that stores this information in a database.

1850 Two different types of tests are conducted on RPCs via the DAQ. Indeed, the performance of the
 1851 detectors is measured periodically during dedicated test beam periods using the H4 muon beam. In
 1852 between these test beam periods, when the beam is not available, the chambers are irradiated by the
 1853 ^{137}Cs in order to accumulate deposited charge and the gamma background is measured.

1854 RPCs under test are connected through LVDS cables to V1190A Time-to-Digital Converter
 1855 (TDC) modules manufactured by CAEN. These modules, located in the rack area outside of the
 1856 bunker, get the logic signals sent by the chambers and save them into their buffers. Due to the
 1857 limited size of the buffers, the collected data is regularly erased and replaced. A trigger signal is
 1858 needed for the TDC modules to send the useful data to the DAQ computer via a V1718 CAEN USB
 1859 communication module.

1860 In the case of performance test, the trigger signal used for data acquisition is generated by the
 1861 coincidence of three scintillators. A first one is placed upstream outside of the bunker, a second one
 1862 is placed downstream outside of the bunker, while a third one is placed in front of the trolley, close by
 1863 the chambers. Every time a trigger is sent to the TDCs, i.e. every time a muon is detected, knowing
 1864 the time delay in between the trigger and the RPC signals, signals located in the right time window
 1865 are extracted from the buffers and saved for later analysis. Signals are taken in a time window of
 1866 400 ns centered on the muon peak (here we could show a time spectrum). On the other hand, in the
 1867 case of background rate measurement, the trigger signal needs to be "random" not to measure muons
 1868 but to look at gamma background. A trigger pulse is continuously generated at a rate of 300 Hz using
 1869 a dual timer. To integrate an as great as possible time, all signals contained within a time window of
 1870 10us prior to the random trigger signal are extracted form the buffers and saved for further analysis
 1871 (here another time spectrum to illustrate could be useful, maybe even place both spectrum together
 1872 as a single Figure).

1873 The signals sent to the TDCs correspond to hit collections in the RPCs. When a particle hits
 1874 a RPC, it induce a signal in the pickup strips of the RPC readout. If this signal is higher than the
 1875 detection threshold, a LVDS signal is sent to the TDCs. The data is then organised into 4 branches
 1876 keeping track of the event number, the hit multiplicity for the whole setup, and the time and channel
 1877 profile of the hits in the TDCs.

1878 **4.4.2 RPC current, environmental and operation parameter monitoring**

1879 In order to take into account the variation of pressure and temperature between different data taking
 1880 periods the applied voltage is corrected following the relationship :

$$1881 \quad HV_{eff} = HV_{app} \times \left(0.2 + 0.8 \cdot \frac{P_0}{P} \times \frac{T}{T_0} \right) \quad (4.10)$$

1881 where T_0 (=293 K) and P_0 (=990 mbar) are the reference values.

1882 **4.4.3 Measurement procedure**

1883 Insert a short description of the online tools (DAQ, DCS, DQM).

1884 Insert a short description of the offline tools : tracking and efficiency algorithm.

1885 Identify long term aging effects we are monitoring the rates per strip.

1886 **4.4.4 Longevity studies results**

5

1887

1888

Investigation on high rate RPCs

1889 **5.1 Rate limitations and ageing of RPCs**

1890 **5.1.1 Low resistivity electrodes**

1891 **5.1.2 Low noise front-end electronics**

1892 **5.2 Construction of prototypes**

1893 **5.3 Results and discussions**

6

1894

1895

Conclusions and outlooks

¹⁸⁹⁶ **6.1 Conclusions**

¹⁸⁹⁷ **6.2 Outlooks**

A

1898

1899

1900

A data acquisition software for CAEN VME TDCs

1901 Certifying detectors in the perspective of HL-LHC required to develop tools for the GIF++ experiment.
1902 Among them was the C++ Data Acquisition (DAQ) software that allows to make the communications
1903 in between a computer and TDC modules in order to retrieve the RPC data [57]. In this
1904 appendix, details about this software, as of how the software was written, how it functions and how
1905 it can be exported to another similar setup, will be given.

1906 A.1 GIF++ DAQ file tree

1907 GIF++ DAQ source code is fully available on github at https://github.com/afagot/GIF_DAQ. The software requires 3 non-optional dependencies:

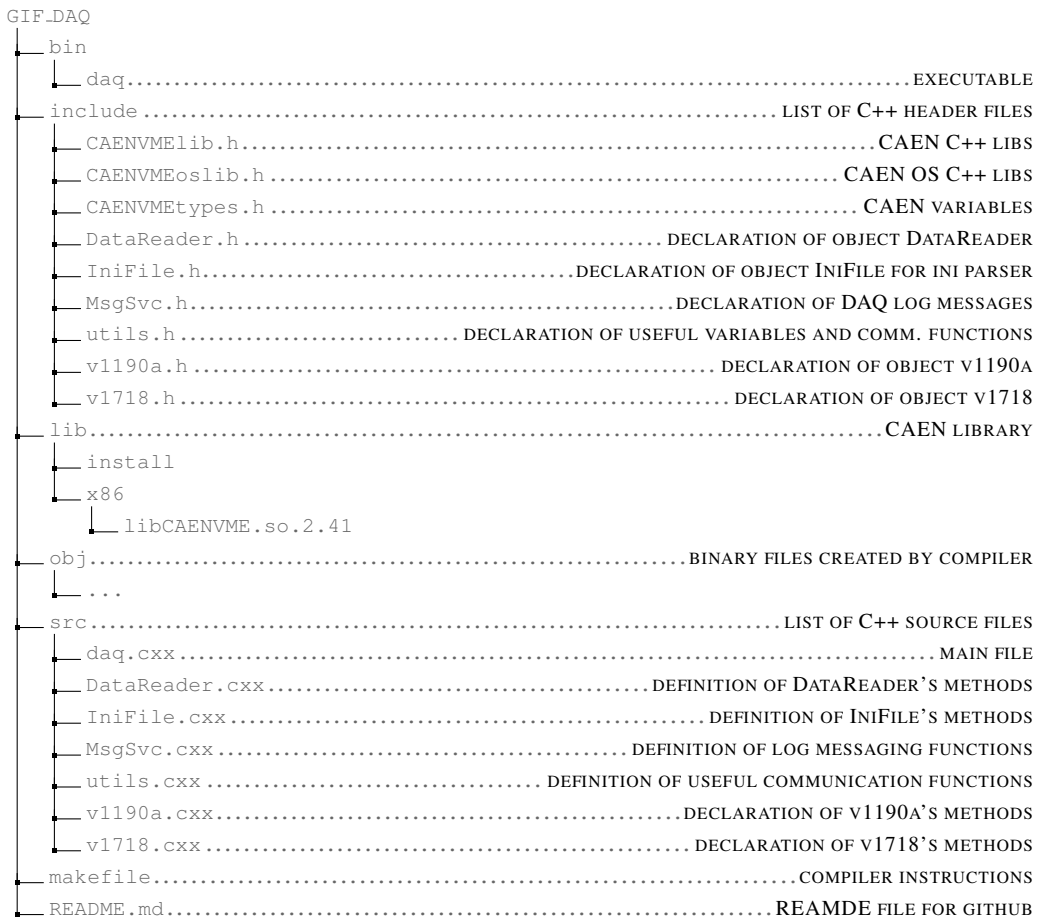
- 1909 • CAEN USB Driver, to mount the VME hardware,
- 1910 • CAEN VME Library, to communicate with the VME hardware, and
- 1911 • ROOT, to organize the collected data into a TTree.

1912 The CAEN VME library will not be packaged by distributions and will need to be installed man-
1913 ually. To compile the GIF++ DAQ project via a terminal, from the DAQ folder use the command:

1914 1915 `make`

1916 The source code tree is provided below along with comments to give an overview of the files' con-
1917 tent. The different objects created for this project (`v1718`, `v1190a`, `IniFile` & `DataReader`) will be
1918 described in details in the following sections.

1919



1920 A.2 Usage of the DAQ

1921 GIF++ DAQ, as used in GIF++, is not a standalone software. Indeed, the system being more com-
 1922 plexe, the DAQ only is a sub-layer of the software architecture developped to control and monitor
 1923 the RPCs that are placed into the bunker for performance study in an irradiated environment. The top
 1924 layer of GIF++ is a Web Detector Control System (webDCS) application. The DAQ is only called
 1925 by the webDCS when data needs to be acquired. The webDCS operates the DAQ through command
 1926 line. To start the DAQ, the webDCS calls:

1927
 1928 bin/daq /path/to/the/log/file/in/the/output/data/folder

1929 where /path/to/the/log/file/in/the/output/data/folder is the only argument required. This
 1930 log file is important for the webDCS as this file contains all the content of the communication of the
 1931 webDCS and the different systems monitored by the webDCS. Its content is constantly displayed
 1932 during data taking for the users to be able to follow the operations. The communication messages
 1933 are normally sent to the webDCS log file via the functions declared in file MsgSvc.h, typically
 1934 MSG_INFO(string message).

1935

A.3 Description of the readout setup

1937 The CMS RPC setup at GIF++ counts 5 V1190A Time-to-Digital Converter (TDC) manufactured
 1938 by CAEN [58]. V1190A are VME units accepting 128 independent Multi-Hit/Multi-Event TDC
 1939 channels whose signals are treated by 4 100 ps high performance TDC chips developed by CERN
 1940 / ECP-MIC Division. The communication between the computer and the TDCs to transfer data is
 1941 done via a V1718 VME master module also manufactured by CAEN and operated from a USB
 1942 port [59]. These VME modules are all hosted into a 6U VME 6021 powered crate manufactured by
 1943 W-Ie-Ne-R than can accommodate up to 21 VME bus cards [60]. These 3 components of the DAQ
 1944 setup are shown in Figure A.1.

1945

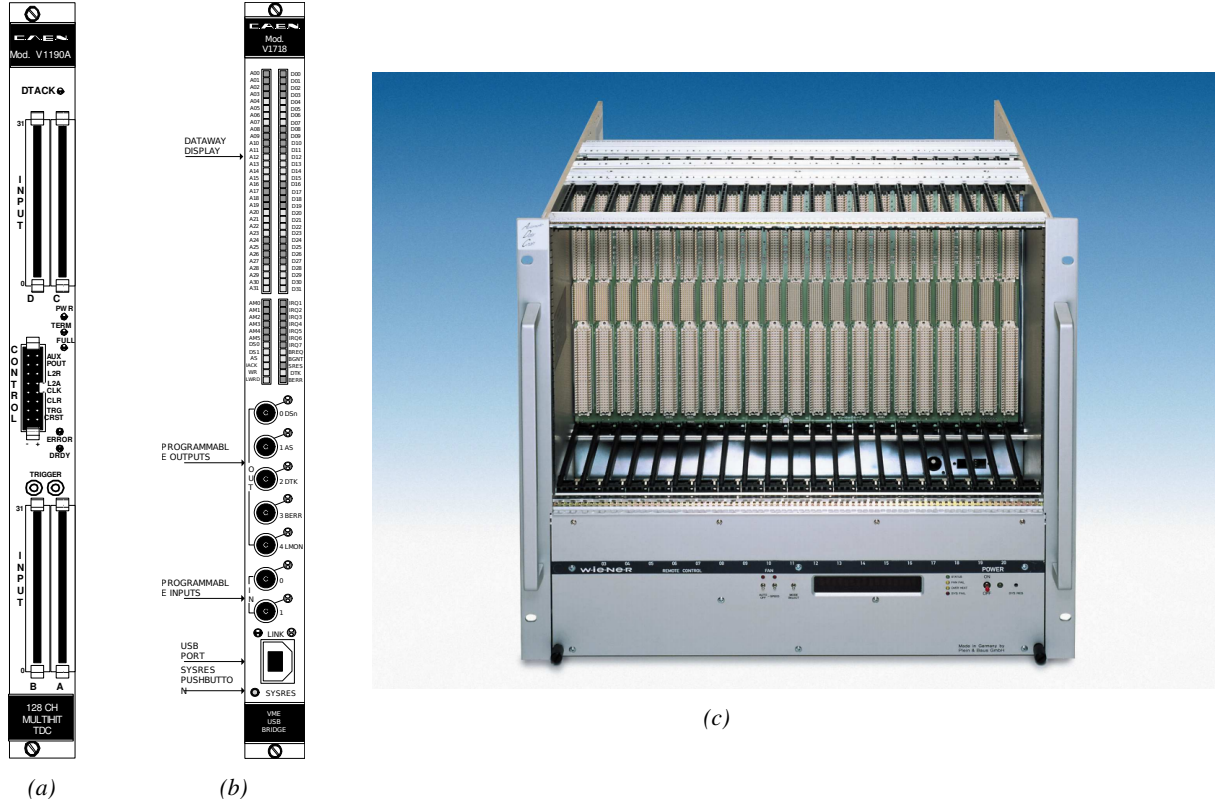


Figure A.1: (A.1a) View of the front panel of a V1190A TDC module [58]. (A.1b) View of the front panel of a V1718 Bridge module [59]. (A.1c) View of the front panel of a 6U 6021 VME crate [60].

1946

A.4 Data read-out

1947 To efficiently perform a data readout algorithm, C++ objects to handle the VME modules (TDCs
 1948 and VME bridge) have been created along with objects to store data and read the configuration file

1949 that comes as an input of the DAQ software.

1950

1951 A.4.1 V1190A TDCs

1952 The DAQ used at GIF takes profit of the *Trigger Matching Mode* offered by V1190A modules.
 1953 This setting is enabled through the method `v1190a::SetTrigMatching (int ntdcs)` where `ntdcs`
 1954 is the total number of TDCs in the setup this setting needs to be enabled for (Source Code A.1). A
 1955 trigger matching is performed in between a trigger time tag, a trigger signal sent into the TRIGGER
 1956 input of the TDC visible on Figure A.1a, and the channel time measurements, signals recorded from
 1957 the detectors under test in our case. Control over this data acquisition mode, explained through
 1958 Figure A.2, is offered via 4 programmable parameters:

- 1959 • **match window:** the matching between a trigger and a hit is done within a programmable time
 1960 window. This is set via the method

```
1961     void v1190a::SetTrigWindowWidth(UINT windowWidth, int ntdcs)
```

- 1962 • **window offset:** temporal distance between the trigger tag and the start of the trigger matching
 1963 window. This is set via the method

```
1964     void v1190a::SetTrigWindowWidth(UINT windowWidth, int ntdcs)
```

- 1965 • **extra search margin:** an extended time window is used to ensure that all matching hits are
 1966 found. This is set via the method

```
1967     void v1190a::SetTrigSearchMargin(UINT searchMargin, int ntdcs)
```

- 1968 • **reject margin:** older hits are automatically rejected to prevent buffer overflows and to speed
 1969 up the search time. This is set via the method

```
1970     void v1190a::SetTrigRejectionMargin(UINT rejectMargin, int ntdcs)
```

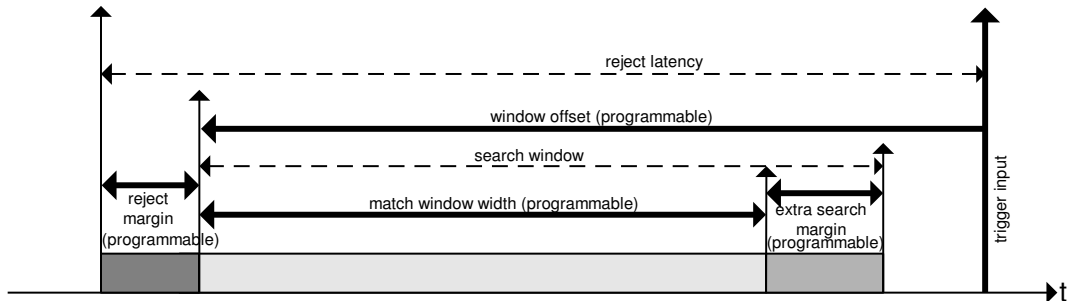


Figure A.2: Module V1190A Trigger Matching Mode timing diagram [58].

1971 Each of these 4 parameters are given in number of clocks, 1 clock being 25 ns long. It is easy to
 1972 understand at this level that there are 3 possible functioning settings:

- 1973 • **1:** the match window is entirely contained after the trigger signal,
- 1974 • **2:** the match window overlaps the trigger signal, or
- 1975 • **3:** the match window is entirely contained before the trigger signal as displayed on Figure A.2.

1976 In both the first and second cases, the sum of the window width and of the offset can be set to
1977 a maximum of 40 clocks, which corresponds to 1 μ s. Evidently, the offset can be negative, allowing
1978 for a longer match window, with the constraint of having the window ending at most 1 μ s after the
1979 trigger signal. In the third case, the maximum negative offset allowed is of 2048 clocks (12 bit) cor-
1980 responding to 51.2 μ s, the match window being strictly smaller than the offset. In the case of GIF++,
1981 the choice has been made to use this last setting by delaying the trigger signal. During the studies
1982 performed in GIF++, both the efficiency of the RPCs, probed using a muon beam, and the noise or
1983 gamma background rate are monitored. The extra search and reject margins are left unused.
1984 To probe the efficiency of RPC detectors, the trigger time tag is provided by the coïncidence of
1985 scintillators when a bunch of muons passes through GIF++ area is used to trigger the data acquisi-
1986 tion. For this measurement, it is useful to reduce the match window width only to contain the muon
1987 information. Indeed, the delay in between a trigger signal and the detection of the corresponding
1988 muon in the RPC being very contant (typically a few tens of ns due to jitter and cable length), the
1989 muon signals are very localised in time. Thus, due to a delay of approximalety 325 ns in between
1990 the muons and the trigger, the settings where chosen to have a window width of 24 clocks (600 ns)
1991 centered on the muon peak thanks to a negative offset of 29 clocks (725 ns).
1992 On the otherhand, monitoring the rates don't require for the DAQ to look at a specific time window.
1993 It is important to integrate enough time to have a robust measurement of the rate as the number of
1994 hits per time unit. The triggerring signal is provided by a pulse generator at a frequency of 300 Hz
1995 to ensure that the data taking occurs in a random way, with respect to beam physics, to probe only
1996 the irradiation spectrum on the detectors. The match window is set to 400 clocks (10 μ s) and the
1997 negative offset to 401 clocks as it needs to exceed the value of the match window.

```
1998
class v1190a
{
    private :
        long             Handle;
        vector<Data32>   Address;
        CVDataWidth      DataWidth;
        CVAddressModifier AddressModifier;

    public:

        v1190a(long handle, IniFile *inifile, int ntdcs);
        ~v1190a();
        Data16 write_op_reg(Data32 address, int code, string error);
        Data16 read_op_reg(Data32 address, string error);
        void Reset(int ntdcs);
        void Clear(int ntdcs);
        void TestWR(Data16 value,int ntdcs);
        void CheckTDCSstatus(int ntdcs);
        void CheckCommunication(int ntdcs);
        void SetTDCTestMode(Data16 mode,int ntdcs);
        void SetTrigMatching(int ntdcs);
        void SetTrigTimeSubtraction(Data16 mode,int ntdcs);
        void SetTrigWindowWidth(Uint windowHeight,int ntdcs);
        void SetTrigWindowOffset(Uint windowOffset,int ntdcs);
        void SetTrigSearchMargin(Uint searchMargin,int ntdcs);
        void SetTrigRejectionMargin(Uint rejectMargin,int ntdcs);
        void GetTrigConfiguration(int ntdcs);
        void SetTrigConfiguration(IniFile *inifile,int ntdcs);
        void SetTDCDetectionMode(Data16 mode,int ntdcs);
        void SetTDCResolution(Data16 lsb,int ntdcs);
        void SetTDCDeadTime(Data16 time,int ntdcs);
        void SetTDCHeadTrailer(Data16 mode,int ntdcs);
        void SetTDCEventSize(Data16 size,int ntdcs);
        void SwitchChannels(IniFile *inifile,int ntdcs);
        void SetIRQ(Data32 level, Data32 count,int ntdcs);
        void SetBlockTransferMode(Data16 mode,int ntdcs);
        void Set(IniFile *inifile,int ntdcs);
        void CheckStatus(CVErrorCodes status) const;
        int ReadBlockD32(Uint tdc, const Data16 address,
                         Data32 *data, const Uint words, bool ignore_berr)
        Uint Read(RAWData *DataList,int ntdcs);
};
```

2000 *Source Code A.1: Description of C++ object v1190a.*

The v1190a object, defined in the DAQ software as in Source Code A.1, offers the possibility to concatenate all TDCs in the readout setup into a single object containing a list of hardware addresses (addresses to access the TDCs' buffer through the VME crate) and each constructor and method acts on the list of TDCs.

2006 A.4.2 DataReader

Enabled thanks to v1190a::SetBlockTransferMode(Data16 mode, int ntdcs), the data transfer is done via Block Transfer (BLT). Using BLT allows to tranfer a fixed number of events called a *block*. This is used together with an Almost Full Level (AFL) of the TDCs' output buffers, defined

2010 through `v1190a::SetIRQ(Data32 level, Data32 count, int ntdcs)`. This AFL gives the maxi-
 2011 mum amount of 32735 words (16 bits, corresponding to the depth of a TDC output buffer) that can
 2012 be written in a buffer before an Interrupt Request (IRQ) is generated and seen by the VME Bridge,
 2013 stopping the data acquisition to transfer the content of each TDC buffers before resuming. For each
 2014 trigger, 6 words or more are written into the TDC buffer:

- 2015 • a **global header** providing information of the event number since the beginning of the data
 acquisition,
- 2017 • a **TDC header**,
- 2018 • the **TDC data** (*if any*), 1 for each hit recorded during the event, providing the channel and the
 time stamp associated to the hit,
- 2020 • a **TDC error** providing error flags,
- 2021 • a **TDC trailer**,
- 2022 • a **global trigger time tag** that provides the absolute trigger time relatively to the last reset,
 and
- 2024 • a **global trailer** providing the total word count in the event.

2025 As previously described in Section ??, CMS RPC FEEs provide us with 100 ns long LVDS out-
 2026 put signals that are injected into the TDCs' input. Any avalanche signal that gives a signal above the
 2027 FEEs threshold is thus recorded by the TDCs as a hit within the match window. Each hit is assigned
 2028 to a specific TDC channel with a time stamp, with a precision of 100 ps. The reference time, $t_0 = 0$,
 2029 is provided by the beginning of the match window. Thus for each trigger, coming from a scintillator
 2030 coïncidence or the pulse generator, a list of hits is stored into the TDCs' buffers and will then be
 2031 transferred into a ROOT Tree.

2032 When the BLT is used, it is easy to understand that the maximum number of words that have
 2033 been set as ALF will not be a finite number of events or, at least, the number of events that would
 2034 be recorded into the TDC buffers will not be a multiple of the block size. In the last BLT cycle to
 2035 tranfer data, the number of events to transfer will most probably be lower than the block size. In that
 2036 case, the TDC can add fillers at the end of the block but this option requires to send more data to the
 2037 computer and is thus a little slower. Another solution is to finish the transfer after the last event by
 2038 sending a bus error that states that the BLT reached the last event in the pile. This method has been
 2039 chosen in GIF++.

2041 Due to irradiation, an event in GIF++ can count up to 300 words per TDC. A limit of 4096 words
 2042 (12 bits) has been set to generate IRQ which represent from 14 to almost 700 events depending on
 2043 the average of hits collected per event. Then the block size has been set to 100 events with enabled
 2044 bus errors. When an AFL is reached for one of the TDCs, the VME bridge stops the acquisition by
 2045 sending a BUSY signal.

2047

```

2048     The data is then transferred one TDC at a time into a structure called RAWData (Source Code A.2).
2049
2050     struct RAWData{
2051         vector<int>           *EventList;
2052         vector<int>           *NHitsList;
2053         vector<int>           *QFlagList;
2054         vector<vector<int> >   *Channellist;
2055         vector<vector<float> > *TimeStampList;
2056     };

```

2051 *Source Code A.2: Description of data holding C++ structure `RAWData`.*

2052 In order to organize the data transfer and the data storage, an object called `DataReader` was
 2053 created (Source Code A.3). On one hand, it has `v1718` and `v1190a` objects as private members for
 2054 communication purposes, such as VME modules settings via the configuration file `*iniFile` or data
 2055 read-out through `v1190a::Read()` and on the other hand, it contains the structure `RAWData` that allows
 2056 to organise the data in vectors reproducing the tree structure of a ROOT file.

```

2057
2058     class DataReader
2059     {
2060         private:
2061             bool      StopFlag;
2062             IniFile *iniFile;
2063             Data32   MaxTriggers;
2064             v1718   *VME;
2065             int       nTDCs;
2066             v1190a *TDCs;
2067             RAWData TDCData;
2068
2069         public:
2070             DataReader();
2071             virtual ~DataReader();
2072             void      SetIniFile(string inifilename);
2073             void      SetMaxTriggers();
2074             Data32 GetMaxTriggers();
2075             void      SetVME();
2076             void      SetTDC();
2077             int       GetQFlag(UInt it);
2078             void      Init(string inifilename);
2079             void      FlushBuffer();
2080             void      Update();
2081             string GetFileName();
2082             void      WriteRunRegistry(string filename);
2083             void      Run();
2084     };

```

2059 *Source Code A.3: Description of C++ object `DataReader`.*

2060 Each event is transferred from `TDCData` and saved into branches of a ROOT `TTree` as 3 integers
 2061 that represent the event ID (`EventCount`), the number of hits read from the TDCs (`nHits`), and the
 2062 quality flag that provides information for any problem in the data transfer (`qflag`), and 2 lists of
 2063 `nHits` elements containing the fired TDC channels (`TDCCh`) and their respective time stamps (`TDCTS`),
 2064 as presented in Source Code A.4. The ROOT file file is named using information contained into
 2065 the configuration file, presented in section A.5.2. The needed information is extracted using method
 2066 `DataReader::GetFileName()` and allow to build the output filename format `ScanXXXXXX_HVX_DAQ.root`

2067 where ScanXXXXXX is a 6 digit number representing the scan number into GIFT++ database and HVX
 2068 the HV step within the scan that can be more than a single digit. An example of ROOT data file is
 2069 provided with Figure A.3.

```
2070
2071 RAWData TDCData;
TFile *outputFile = new TFile(outputFileName.c_str(),"recreate");
TTree *RAWDataTree = new TTree("RAWData","RAWData");

int EventCount = -9;
int nHits = -8;
int qflag = -7;
vector<int> TDCCh;
vector<float> TDCTS;

RAWDataTree->Branch("EventNumber",&EventCount, "EventNumber/I");
RAWDataTree->Branch("number_of_hits",&nHits,"number_of_hits/I");
RAWDataTree->Branch("Quality_flag",&qflag,"Quality_flag/I");
RAWDataTree->Branch("TDC_channel",&TDCCh);
RAWDataTree->Branch("TDC_TimeStamp",&TDCTS);

2072 //...
//Here read the TDC data using v1190a::Read() and place it into
//TDCData for as long as you didn't collect the requested amount
//of data.
//...

for(Uint i=0; i<TDCData.EventList->size(); i++){
    EventCount = TDCData.EventList->at(i);
    nHits = TDCData.NHitsList->at(i);
    qflag = TDCData.QFlagList->at(i);
    TDCCh = TDCData.ChannelList->at(i);
    TDCTS = TDCData.TimeStampList->at(i);
    RAWDataTree->Fill();
}
```

2072 *Source Code A.4: Highlight of the data transfer and organisation within DataReader::Run() after the data has been collected into TDCData.*

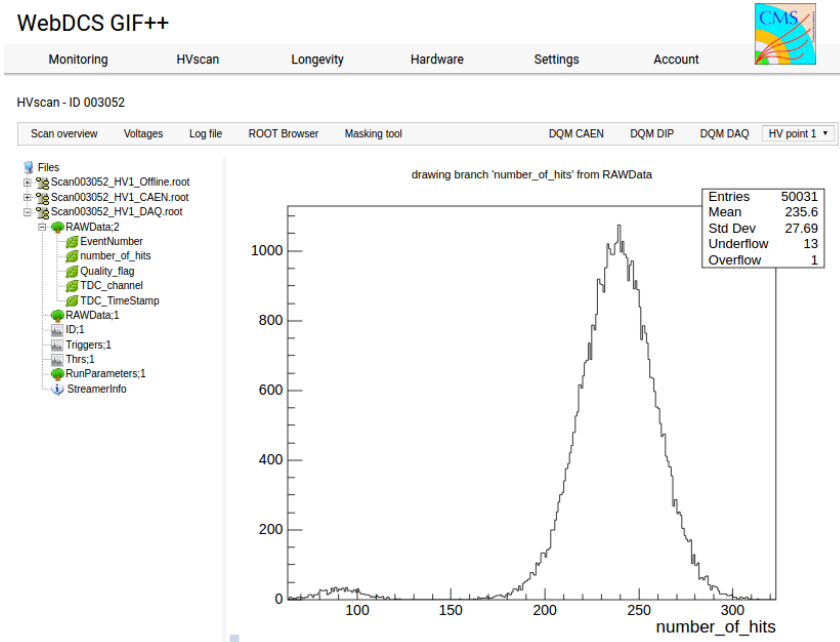


Figure A.3: Structure of the ROOT output file generated by the DAQ. The 5 branches (EventNumber, number_of_hits, Quality_flag, TDC_channel and TDC_TimeStamp) are visible on the left panel of the ROOT browser. On the right panel is visible the histogram corresponding to the variable nHits. In this specific example, there were approximately 50k events recorded to measure the gamma irradiation rate on the detectors. Each event is stored as a single entry in the TTree.

2073 A.4.3 Data quality flag

2074 Among the parameters that are recorded for each event, the quality flag, defined in Source Code A.5,
 2075 is determined on the fly by checking the data recorded by every single TDC. From method `v1190a::Read()`,
 2076 it can be understood that the content of each TDC buffer is readout one TDC at a time. Entries are
 2077 created in the data list for the first TDC and then, when the second buffer is readout, events corre-
 2078 sponding to entries that have already been created to store data for the previous TDC are added to
 2079 the existing list element. On the contrary, when an event entry has not been yet created in the data
 2080 list, a new entry is created.

```
2081    typedef enum _QualityFlag {
 2082     GOOD      = 1,
 2083     CORRUPTED = 0
 2084 } QualityFlag;
```

2083 *Source Code A.5: Definition of the quality flag `enum`.*

2084 It is possible that each TDC buffer contains a different number of events. In cases where the first
 2085 element in the buffer list is an event for corresponds to a new entry, the difference in between the
 2086 entry from the buffer and the last entry in the data list is recorded and checked. If it is greater than 1,
 2087 what should never be the case, the quality flag is set to CORRUPTED for this TDC and an empty entry
 2088 is created in the place of the missing ones. Missing entries are believe to be the result of a bad hold

2089 on the TDC buffers at the moment of the readout. Indeed, the software hold is effective only on 1
 2090 TDC at a time and no solution as been found yet to completely block the writting in the buffers when
 2091 an IRQ is received.

2092 At the end of each BLT cycle, the ID of the last entry stored for each TDC buffer is not recorded.
 2093 When starting the next cycle, if the first entry in the pile corresponds to an event already existing
 2094 in the list, the readout will start from this list element and will not be able to check the difference
 2095 in between this entry's ID and the one of the last entry that was recorded for this TDC buffer in
 2096 the previous cycle. In the case events were missing, the flag stays at its initial value of 0, which is
 2097 similar to CORRUPTED and it is assumed that then this TDC will not contribute to `number_of_hits`,
 2098 `TDC_channel` or `TDC_TimeStamp`.

2099 Finally, since there will be 1 `RAWData` entry per TDC for each event (meaning `nTDCs` entries,
 2100 referring to `DataReader` private attribute), the individual flags of each TDC will be added together.
 2101 The final format is an integer composed `nTDCs` digits where each digit is the flag of a specific TDC.
 2102 This is constructed using powers of 10 like follows:

```
2103 TDC 0: QFlag = 100 × _QualityFlag
2104 TDC 1: QFlag = 101 × _QualityFlag
2105 ...
2106 TDC N: QFlag = 10N × _QualityFlag
```

2107 and the final flag to be with N digits:

```
2108 QFlag = n....3210
```

2109 each digit being 1 or 0. Below is given an example with a 4 TDCs setup.

2110 If all TDCs were good : `QFlag = 1111`,

2111 but if TDC 2 was corrupted : `QFlag = 1011`.

2112 When data taking is over and the data contained in the dynamical `RAWData` structure is transferred
 2113 to the ROOT file, all the 0s are changed into 2s by calling the method `DataReader::GetQFlag()`.
 2114 This will help translating the flag without knowing the number of TDCs beforehand. Indeed, a flag
 2115 111 could be due to a 3 TDC setup with 3 good individual TDC flags or to a more than 3 TDC setup
 2116 with TDCs those ID is greater than 2 being CORRUPTED, thus giving a 0.

2117 The quality flag has been introduced quite late, in October 2017 only, to the list of GIFT++ DAQ
 2118 parameters to be recorded into the output ROOT file. Before this addition, the missing data, corrupting
 2119 the quality for the offline analysis, was contributing to artificially fill data with lower multiplicity.
 2120 Looking at `TBranch number_of_hits` provides an information about the data of the full GIFT++
 2121 setup. When a TDC is not able to transfer data for a specific event, the effect is a reduction of the
 2122 total number of hits recorded in the full setup, this is what can be seen from Figure A.4. After offline
 2123 reconstruction detector by detector, the effect of missing events can be seen in the artificially filled
 2124 bin at multiplicity 0 shown in Figure A.5. Nonetheless, for data with high irradiation levels, as it is
 2125 the case for Figure A.5a, discarding the fake multiplicity 0 data can be done easily during the offline
 2126 analysis. At lower radiation, the missing events contribution becomes more problematic as the mul-
 2127 tiplicity distribution overlaps the multiplicity 0 and that in the same time the proportion of missing

2128 events decreases. Attempts to fit the distribution with a Poisson or skew distribution function were
 2129 not conclusive and this very problem has been at the origin of the quality flag that allows to give a
 2130 non ambiguous information about each event quality.

2131

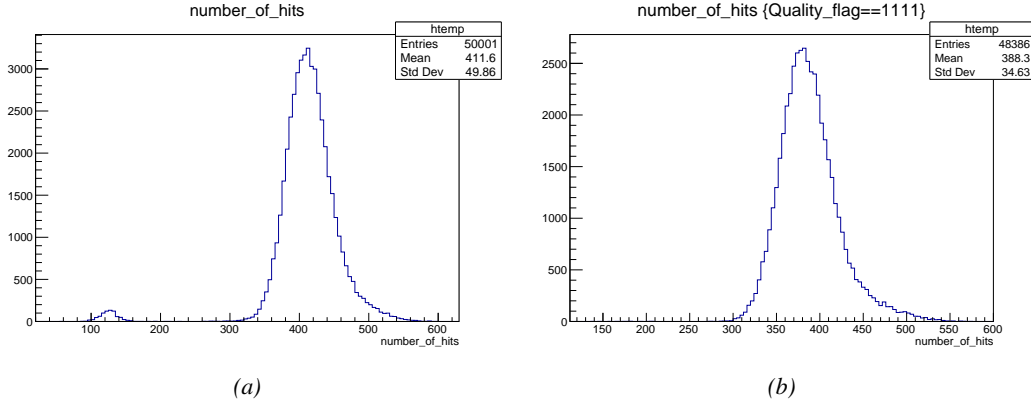


Figure A.4: The effect of the quality flag is explained by presenting the content of TBranch `number_of_hits` of a data file without `Quality_flag` in Figure A.4a and the content of the same TBranch for data corresponding to a `Quality_flag` where all TDCs were labelled as `GOOD` in Figure A.4b taken with similar conditions. It can be noted that the number of entries in Figure A.4b is slightly lower than in Figure A.4a due to the excluded events.

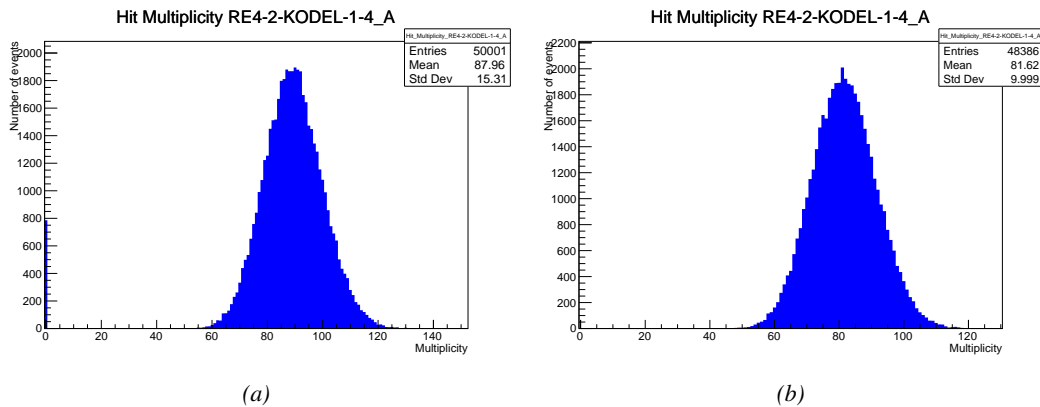


Figure A.5: Using the same data as previously showed in Figure A.4, the effect of the quality flag is explained by presenting the reconstructed hit multiplicity of a data file without `Quality_flag` in Figure A.5a and the reconstructed content of the same RPC partition for data corresponding to a `Quality_flag` where all TDCs were labelled as `GOOD` in Figure A.5b taken with similar conditions. The artificial high content of bin 0 is completely suppressed.

A.5 Communications

2132 To ensure data readout and dialog in between the machine and the TDCs or in between the webDCS
 2133 and the DAQ, different communication solutions were used. First of all, it is important to have a

2134

2135 module to allow the communication in between the TDCs and the computer from which the DAQ
 2136 operates. When this communication is effective, shifters using the webDCS to control data taking
 2137 can thus send instructions to the DAQ.

2138

2139 A.5.1 V1718 USB Bridge

2140 In the previous section, the data transfer has been discussed. The importance of the `v1718` object
 2141 (Source Code A.6), used as private member of `DataReader`, was not explicated. VME master
 2142 modules are used for communication purposes as they host the USB port that connects the pow-
 2143 ered crate buffer to the computer where the DAQ is installed. From the source code point of view,
 2144 this object is used to control the communication status, by reading the returned error codes with
 2145 `v1718::CheckStatus()`, or to check for IRQs coming from the TDCs through `v1718::CheckIRQ()`.
 2146 Finally, to ensure that triggers are blocked at the hardware level, a NIM pulse is sent out of one of the
 2147 5 programmable outputs (`v1718::SendBUSY()`) to the VETO of the coincidence module where the
 2148 trigger signals originate from. As long as this signal is ON, no trigger can reach the TDCs anymore.
 2149

```
2149
class v1718{
    private:
        int             Handle;
        Data32          Data;           // Data
        CVIRQLevels    Level;         // Interrupt level
        CVAddressModifier AM;          // Addressing Mode
        CVDataWidth     DataSize;      // Data Format
        Data32          BaseAddress;   // Base Address

    public:
        v1718(IniFile *inifile);
        ~v1718();
        long            GetHandle(void) const;
        int             SetData(Data16 data);
        Data16          GetData(void);
        int             SetLevel(CVIRQLevels level);
        CVIRQLevels    GetLevel(void);
        int             SetAM(CVAddressModifier am);
        CVAddressModifier GetAM(void);
        int             SetDatasize(CVDataWidth datasize);
        CVDataWidth     GetDataSize(void);
        int             SetBaseAddress(Data16 baseaddress);
        Data16          GetBaseAddress(void);
        void            CheckStatus(CVErrorCodes status) const;
        void            CheckIRQ();
        void            SetPulsers();
        void            SendBUSY(BusyLevel level);
};
```

2151 *Source Code A.6: Description of C++ object v1718.*

2152 A.5.2 Configuration file

2153 The DAQ software takes as input a configuration file written using INI standard [61]. This file is
 2154 partly filled with the information provided by the shifters when starting data acquisition using the
 2155 webDCS, as shown by Figure A.6. This information is written in section [`General`] and will later

2156 be stored in the ROOT file that contains the DAQ data as can be seen from Figure A.3. Indeed,
 2157 another `TTree` called `RunParameters` as well as the 2 histograms `ID`, containing the scan number,
 2158 start and stop time stamps, and `Triggers`, containing the number of triggers requested by the shifter,
 2159 are available in the data files. Moreover, `ScanID` and `HV` are then used to construct the file name
 2160 thanks to the method `DataReader::GetFileName()`.

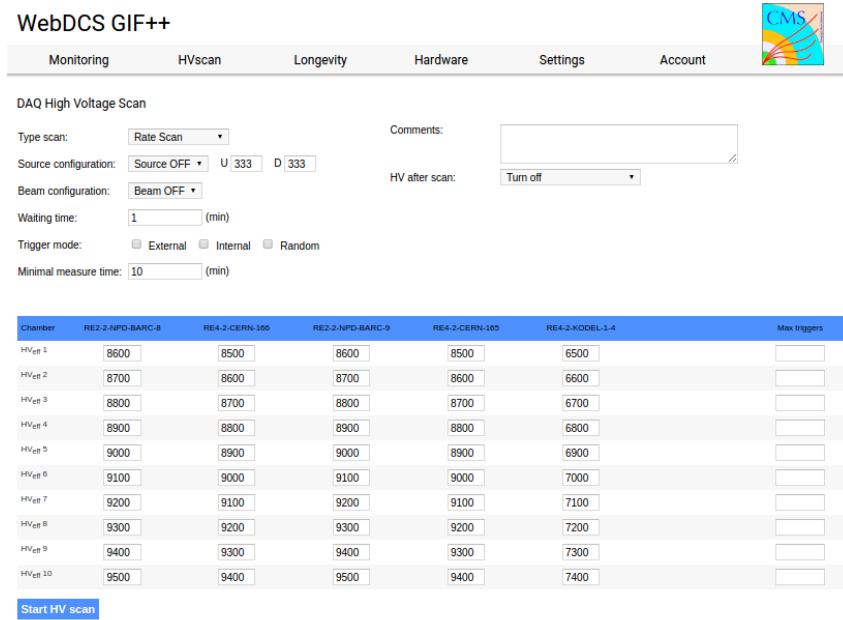


Figure A.6: WebDCS DAQ scan page. On this page, shifters need to choose the type of scan (Rate, Efficiency or Noise Reference scan), the gamma source configuration at the moment of data taking, the beam configuration, and the trigger mode. These information will be stored in the DAQ ROOT output. Are also given the minimal measurement time and waiting time after ramping up of the detectors is over before starting the data acquisition. Then, the list of HV points to scan and the number of triggers for each run of the scan are given in the table underneath.

2161 The rest of the information is written beforehand in the configuration file template, as explicated
 2162 in Source Code A.7, and contains the hardware addresses to the different VME modules in the
 2163 setup as well as settings for the TDCs. As the TDC settings available in the configuration file are not
 2164 supposed to be modified, an improvement would be to remove them from the configuration file and
 2165 to hardcode them inside of the DAQ code itself or to place them into a different INI file that would
 2166 host only the TDC settings to lower the probability for a bad manipulation of the configuration file
 2167 that can be modified from one of webDCS' menus.

2168

```

[General]
TdcS=4
ScanID=$scanid
HV=$HV
RunType=$runtype
MaxTriggers=$maxtriggers
Beam=$beam
[VMEInterface]
Type=V1718
BaseAddress=0xFF0000
Name=VmeInterface
[TDC0]
Type=V1190A
BaseAddress=0x00000000
Name=Tdc0
StatusA00-15=1
StatusA16-31=1
StatusB00-15=1
StatusB16-31=1
StatusC00-15=1
StatusC16-31=1
StatusD00-15=1
StatusD16-31=1
[TDC1]
Type=V1190A
BaseAddress=0x11110000
Name=Tdc1
StatusA00-15=1
StatusA16-31=1
StatusB00-15=1
StatusB16-31=1
StatusC00-15=1
StatusC16-31=1
StatusD00-15=1
StatusD16-31=1
[TDC2]
Type=V1190A
BaseAddress=0x22220000
Name=Tdc2
StatusA00-15=1
StatusA16-31=1
StatusB00-15=1
StatusB16-31=1
StatusC00-15=1
StatusC16-31=1
StatusD00-15=1
StatusD16-31=1
[TDC3]
Type=V1190A
BaseAddress=0x44440000
Name=Tdc3
StatusA00-15=1
StatusA16-31=1
StatusB00-15=1
StatusB16-31=1
StatusC00-15=1
StatusC16-31=1
StatusD00-15=1
StatusD16-31=1
[TDCSettings]
TriggerExtraSearchMargin=0
TriggerRejectMargin=0
TriggerTimeSubtraction=0b1
TdcDetectionMode=0b01
TdcResolution=0b10
TdcDeadTime=0b00
TdcHeadTrailer=0b1
TdcEventSize=0b1001
TdcTestMode=0b0
BLTMode=1

```

Source Code A.7: INI configuration file template for 4 TDCs. In section [**General**], the number of TDCs is explicitated and information about the ongoing run is given. Then, there are sections for each and every VME modules. There buffer addresses are given and for the TDCs, the list of channels to enable is given. Finally, in section [**TDCSettings**], a part of the TDC settings are given.

In order to retrieve the information of the configuration file, the object `IniFile` has been developed to provide an INI parser, presented in Source Code A.8. It contains private methods returning a boolean to check the type of line written in the file, whether a comment, a group header or a key line (`IniFile::CheckIfComment()`, `IniFile::CheckIfGroup()` and `IniFile::CheckIfToken()`). The key may sometimes be referred to as *token* in the source code. Moreover, the private element `FileData` is a map of `const string` to `string` that allows to store the data contained inside the configuration file via the public method `IniFile::GetFileData()` following the formatting (see method `IniFile::Read()`):

```
2179     string group, token, value;
2180     // Get the field values for the 3 strings.
2181     // Then concatenate group and token together as a single string
2182     // with a dot separation.
2183     token = group + "." + token;
2184     FileData[token] = value;
```

More methods have been written to translate the different keys into the right variable format when used by the DAQ. For example, to get a `float` value out of the configuration file data, knowing the group and the key needed, the method `IniFile::floatType()` can be used. It takes 3 arguments being the group name and key name (both `string`), and a default `float` value used as exception in the case the expected combination of group and key cannot be found in the configuration file. This default value is then used and the DAQ continues on working after sending an alert in the log file for further debugging.

```

2188 typedef map< const string, string > IniFileData;
2189
class IniFile{
    private:
        bool          CheckIfComment (string line);
        bool          CheckIfGroup(string line, string& group);
        bool          CheckIfToken(string line, string& key, string& value);
        string         FileName;
        IniFileData   FileData;
        int           Error;

    public:
        IniFile();
        IniFile(string filename);
        virtual      ~IniFile();

        // Basic file operations
        void          SetFileName(string filename);
        int           Read();
        int           Write();
        IniFileData GetFileData();

        // Data readout methods
        Data32         addressType (string groupname, string keyname, Data32
→     defaultvalue);
        long          intType     (string groupname, string keyname, long
→     defaultvalue);
        long long    longType    (string groupname, string keyname, long long
→     defaultvalue );
        string         stringType  (string groupname, string keyname, string
→     defaultvalue );
        float         floatType   (string groupname, string keyname, float
→     defaultvalue );

        // Error methods
        string         GetErrorMsg();
    };

```

2190 *Source Code A.8: Description of C++ object `IniFile` used as a parser for INI file format.*

2191 A.5.3 WebDCS/DAQ intercommunication

2192 When shifters send instructions to the DAQ via the configuration file, it is the webDCS itself that
 2193 gives the start command to the DAQ and then the 2 softwares use inter-process communication
 2194 through file to synchronise themselves. This communication file is represented by the variable **const**
 2195 string __runstatuspath.

2196 On one side, the webDCS sends commands or status that are readout by the DAQ:

- 2197 • INIT, status sent when launching a scan and read via function `CtrlRunStatus(...)`,
- 2198 • START, command to start data taking and read via function `CheckSTART()`,
- 2199 • STOP, command to stop data taking at the end of the scan and read via function `CheckSTOP()`,
 2200 and
- 2201 • KILL, command to kill data taking sent by user and read via function `CheckKILL()`

2202 and on the other, the DAQ sends status that are controled by the webDCS:

- 2203 ● `DAQ_RDY`, sent with `SendDAQReady()` to signify that the DAQ is ready to receive commands
2204 from the webDCS,
- 2205 ● `RUNNING`, sent with `SendDAQRunning()` to signify that the DAQ is taking data,
- 2206 ● `DAQ_ERR`, sent with `SendDAQError()` to signify that the DAQ didn't receive the expected com-
2207 mand from the webDCS or that the launch command didn't have the right number of argu-
2208 ments,
- 2209 ● `RD_ERR`, sent when the DAQ wasn't able to read the communication file, and
- 2210 ● `WR_ERR`, sent when the DAQ wasn't able to write into the communication file.

2211 **A.5.4 Example of inter-process communication cycle**

2212 Under normal conditions, the webDCS and the DAQ processes exchange commands and status via
2213 the file hosted at the address `__runstatuspath`, as explained in subsection A.5.3. An example of
2214 cycle is given in Table A.1. In this example, the steps 3 to 5 are repeated as long as the webDCS tells
2215 the DAQ to take data. A data taking cycle is the equivalent as what is called a *Scan* in GIFT++ jargon,
2216 referring to a set a runs with several HV steps. Each repetition of steps 3 to 5 is then equivalent to a
2217 single *Run*.

2218

2219 At any moment during the data taking, for any reason, the shifter can decide that the data taking
2220 needs to be stopped before it reached the end of the scheduled cycle. Thus at any moment on the
2221 cycle, the content of the inter-process communication file will be changed to `KILL` and the DAQ will
2222 shut down right away. The DAQ checks for `KILL` signals every 5s after the TDCs configuration is
2223 over. So far, the function `CheckKILL()` has been used only inside of the data taking loop of method
2224 `DataReader::Run()` and thus, if the shifter decides to KILL the data taking during the TDC con-
2225 figuration phase or the HV ramping in between 2 HV steps, the DAQ will not be stopped smoothly
2226 and a *force kill* command will be sent to stop the DAQ process that is still awake on the computer.
2227 Improvements can be brought on this part of the software to make sure that the DAQ can safely
2228 shutdown at any moment.

2229

2230 **A.6 Software export**

2231 In section A.2 was discussed the fact that the DAQ as written in its last version is not a standalone
2232 software. It is possible to make it a standalone program that could be adapted to any VME setup
2233 using V1190A and V1718 modules by creating a GUI for the software or by printing the log mes-
2234 sages that are normally printed in the webDCS through the log file, directly into the terminal. This
2235 method was used by the DAQ up to version 3.0 moment where the webDCS was completed. Also, it
2236 is possible to check branches of DAQ v2.X to have example of communication through a terminal.

2237

2238 DAQ v2.X is nonetheless limited in it's possibilities and requires a lot of offline manual interven-
2239 tions from the users. Indeed, there is no communication of the software with the detectors' power
2240 supply system that would allow for a user a predefine a list of voltages to operate the detectors at

step	actions of webDCS	status of DAQ	<code>__runstatuspath</code>
1	launch DAQ ramp voltages ramping over wait for currents stabilization	readout of IniFile configuration of TDCs	INIT
2		configuration done send DAQ ready wait for START signal	DAQ_RDY
3	waiting time over send START		START
4	wait for run to end monitor DAQ run status	data taking ongoing check for KILL signal	RUNNING
5		run over send DAQ_RDY wait for next DCS signal	DAQ_RDY
6	ramp voltages ramping over wait for currents stabilization		DAQ_RDY
3	waiting time over send START		START
4	wait for run to end monitor DAQ run status	update IniFile information data taking ongoing check for KILL signal	RUNNING
5		run over send DAQ_RDY wait for next DCS signal	DAQ_RDY
7	send command STOP	DAQ shuts down	STOP

Table A.1: Inter-process communication cycles in between the webDCS and the DAQ through file string signals.

2241 and loop over to take data without any further manual intervention. In v2.X, the data is taken for a
2242 single detector setting and at the end of each run, the softwares asks the user if he intends on taking
2243 more runs. If so, the software invites the user to set the operating voltages accordingly to what is
2244 necessary and to manual update the configuration file in consequence. This working mode can be a
2245 very first approach before an evolution and has been successfully used by colleagues from different
2246 collaborations.

2247

2248 For a more robust operation, it is recommended to develop a GUI or a web application to inter-
2249 face the DAQ. Moreover, to limit the amount of manual interventions, and thus the probability to
2250 make mistakes, it is also recommended to add an extra feature into the DAQ by installing the HV
2251 Wrapper library provided by CAEN of which an example of use in a similar DAQ software devel-
2252 opped by a master student of UGent, and called TinyDAQ, is provided on UGent's github. Then, this
2253 HV Wrapper will help you communicating with and give instructions to a CAEN HV powered crate
2254 and can be added into the DAQ at the same level where the communication with the user was made
2255 in DAQ v2.X. In case you are using another kind of power system for your detectors, it is stringly
2256 adviced to use HV modules or crates that can be remotely controled via a using C++ libraries.

2257

B

2258

2259

Details on the offline analysis package

2260 The data collected in GIF++ thanks to the DAQ described in Appendix A is difficult to interpret by
2261 a human user that doesn't have a clear idea of the raw data architecture of the ROOT data files. In
2262 order to render the data human readable, a C++ offline analysis tool was designed to provide users
2263 with detector by detector histograms that give a clear overview of the parameters monitored during
2264 the data acquisition [62]. In this appendix, details about this software in the context of GIF++, as of
2265 how the software was written and how it functions will be given.

2266 B.1 GIF++ Offline Analysis file tree

2267 GIF++ Offline Analysis source code is fully available on github at https://github.com/afagot/GIF_OfflineAnalysis. The software requires ROOT as non-optionnal dependency
2268 as it takes ROOT files in input and write an output ROOT file containing histograms. To compile the
2269 GIF++ Offline Analysis project is compiled with cmake. To compile, first a build/ directory must
2270 be created to compile from there:

```
2272 mkdir build
2273 cd build
2274 cmake ..
2275 make
2276 make install
```

2274 To clean the directory and create a new build directory, the bash script cleandir.sh can be used:

```
2275
2276 ./cleandir.sh
```

2277 The source code tree is provided below along with comments to give an overview of the files' con-
2278 tent. The different objects created for this project (`Infrastructure`, `Trolley`, `RPC`, `Mapping`, `RPCHit`,
2279 `RPCCluster` and `Inifile`) will be described in details in the following sections.

2280

```

GIF_OfflineAnalysis
├── bin
│   └── offlineanalysis ..... EXECUTABLE
├── build..... CMAKE COMPILATION DIRECTORY
└── ...
    ├── include..... LIST OF C++ HEADER FILES
    │   ├── Cluster.h..... DECLARATION OF OBJECT RPCCLUSTER
    │   ├── Current.h..... DECLARATION OF GETCURRENT ANALYSIS MACRO
    │   ├── GIFTrolley.h..... DECLARATION OF OBJECT TROLLEY
    │   ├── Infrastructure.h..... DECLARATION OF OBJECT INFRASTRUCTURE
    │   ├── IniFile.h..... DECLARATION OF OBJECT INI FILE FORINI PARSER
    │   ├── Mapping.h..... DECLARATION OF OBJECT MAPPING
    │   ├── MsgSvc.h..... DECLARATION OF OFFLINE LOG MESSAGES
    │   ├── OfflineAnalysis.h..... DECLARATION OF DATA ANALYSIS MACRO
    │   ├── RPCDetector.h..... DECLARATION OF OBJECT RPC
    │   ├── RPCHit.h..... DECLARARION OF OBJECT RPCHIT
    │   ├── types.h..... DEFINITION OF USEFUL VARIABLE TYPES
    │   └── utils.h..... DECLARATION OF USEFUL FUNCTIONS
    ├── obj..... BINARY FILES CREATED BY COMPILER
    └── ...
        ├── src..... LIST OF C++ SOURCE FILES
        │   ├── Cluster.cc..... DEFINITION OF OBJECT RPCCLUSTER
        │   ├── Current.cc ..... DEFINITION OF GETCURRENT ANALYSIS MACRO
        │   ├── GIFTrolley.cc..... DEFINITION OF OBJECT TROLLEY
        │   ├── Infrastructure.cc..... DEFINITION OF OBJECT INFRASTRUCTURE
        │   ├── IniFile.cc..... DEFINITION OF OBJECT INI FILE FORINI PARSER
        │   ├── main.cc..... MAIN FILE
        │   ├── Mapping.cc..... DEFINITION OF OBJECT MAPPING
        │   ├── MsgSvc.cc..... DEFINITION OF OFFLINE LOG MESSAGES
        │   ├── OfflineAnalysis.cc..... DEFINITION OF DATA ANALYSIS MACRO
        │   ├── RPCDetector.cc..... DEFINITION OF OBJECT RPC
        │   ├── RPCHit.cc..... DEFINITION OF OBJECT RPCHIT
        │   └── utils.cc..... DEFINITION OF USEFUL FUNCTIONS
        ├── cleandir.sh..... BASH SCRIPT TO CLEAN BUILD DIRECTORY
        ├── CMakeLists.txt..... SET OF INSTRUCTIONS FOR CMAKE
        ├── config.h.in..... DEFINITION OF VERSION NUMBER
        └── README.md..... REAMDE FILE FOR GITHUB

```

2281

B.2 Usage of the Offline Analysis

2282

In order to use the Offline Analysis tool, it is necessary to know the Scan number and the HV Step of the run that needs to be analysed. This information needs to be written in the following format:

2284

2285

```
Scan00XXXX_HVY
```

2286

where XXXX is the scan ID and y is the high voltage step (in case of a high voltage scan, data will be taken for several HV steps). This format corresponds to the base name of data files in the database

2287

2288 of the GIF++ webDCS. Usually, the offline analysis tool is automatically called by the webDCS at
 2289 the end of data taking or by a user from the webDCS panel if an update of the tool was brought.
 2290 Nonetheless, an expert can locally launch the analysis for tests on the GIF++ computer, or a user can
 2291 get the code on its local machine from github and download data from the webDCS for its own anal-
 2292 ysis. To launch the code, the following command can be used from the `GIF_OfflineAnalysis` folder:

2293
 2294 `bin/offlineanalysis /path/to/Scan00XXXX_HVY`

2295 where, `/path/to/Scan00XXXX_HVY` refers to the local data files. Then, the offline tool will by itself
 2296 take care of finding all available ROOT data files present in the folder, as listed below:

- 2297
 - 2298 ● `Scan00XXXX_HVY_DAQ.root` containing the TDC data as described in Appendix ?? (events, hit
 and timestamp lists), and
 - 2299 ● `Scan00XXXX_HVY_CAEN.root` containing the CAEN mainframe data recorded by the monitor-
 ing tool webDCS during data taking (HVs and currents of every HV channels). This file is
 created independently of the DAQ.

2302 **B.2.1 Output of the offline tool**

2303 **B.2.1.1 ROOT file**

2304 The analysis gives in output ROOT datafiles that are saved into the data folder and called using the
 2305 naming convention `Scan00XXXX_HVY_Offline.root`. Inside those, a list of `TH1` histograms can be
 2306 found. Its size will vary as a function of the number of detectors in the setup as each set of histograms
 2307 is produced detector by detector. For each partition of each chamber, can be found:

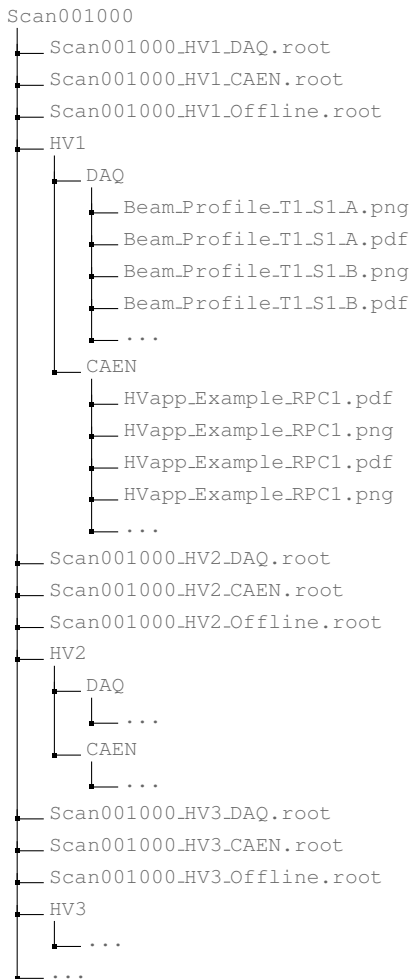
- 2308
 - 2309 ● `Time_Profile_Tt_Sc_p` shows the time profile of all recorded events (number of events per
 time bin),
 - 2310 ● `Hit_Profile_Tt_Sc_p` shows the hit profile of all recorded events (number of events per chan-
 nel),
 - 2312 ● `Hit_Multiplicity_Tt_Sc_p` shows the hit multiplicity (number of hits per event) of all recorded
 events (number of occurrences per multiplicity bin),
 - 2314 ● `Strip_Mean_Noise_Tt_Sc_p` shows noise/gamma rate per unit area for each strip in a se-
 lected time range. After filters are applied on `Time_Profile_Tt_Sc_p`, the filtered version
 of `Hit_Profile_Tt_Sc_p` is normalised to the total integrated time and active detection area
 of a single channel,
 - 2318 ● `Strip_Activity_Tt_Sc_p` shows noise/gamma activity for each strip (normalised version of
 previous histogram - strip activity = strip rate / average partition rate),
 - 2320 ● `Strip_Homogeneity_Tt_Sc_p` shows the *homogeneity* of a given partition ($\text{homogeneity} = \exp(-\text{strip rates standard deviation(strip rates in partition/average partition rate)})$),
 - 2322 ● `mask_Strip_Mean_Noise_Tt_Sc_p` shows noise/gamma rate per unit area for each masked
 strip in a selected time range. Offline, the user can control the noise/gamma rate and decide to
 mask the strips that are judged to be noisy or dead. This is done via the *Masking Tool* provided
 by the webDCS,

- 2326 ● `mask_Strip_Activity_Tt_Sc_p` shows noise/gamma activity per unit area for each masked
2327 strip with respect to the average rate of active strips,
- 2328 ● `NoiseCSize_H_Tt_Sc_p` shows noise/gamma cluster size, a cluster being constructed out of
2329 adjacent strips giving a signal at the *same time* (hits within a time window of 25 ns),
- 2330 ● `NoiseCMult_H_Tt_Sc_p` shows noise/gamma cluster multiplicity (number of reconstructed
2331 clusters per event),
- 2332 ● `Chip_Mean_Noise_Tt_Sc_p` shows the same information than `Strip_Mean_Noise_Tt_Scp` us-
2333 ing a different binning (1 chip corresponds to 8 strips),
- 2334 ● `Chip_Activity_Tt_Sc_p` shows the same information than `Strip_Activity_Tt_Scp` using
2335 chip binning,
- 2336 ● `Chip_Homogeneity_Tt_Sc_p` shows the homogeneity of a given partition using chip binning,
- 2337 ● `Beam_Profile_Tt_Sc_p` shows the estimated beam profile when taking efficiency scan. This
2338 is obtained by filtering `Time_Profile_Tt_Sc_p` to only consider the muon peak where the
2339 noise/gamma background has been subtracted. The resulting hit profile corresponds to the
2340 beam profile on the detector channels,
- 2341 ● `L0_Efficiency_Tt_Sc_p` shows the level 0 efficiency that was estimated **without** muon track-
2342 ing,
- 2343 ● `MuonCSize_H_Tt_Sc_p` shows the level 0 muon cluster size that was estimated **without** muon
2344 tracking, and
- 2345 ● `MuonCMult_H_Tt_Sc_p` shows the level 0 muon cluster multiplicity that was estimated **without**
2346 muon tracking.

2347 In the histogram labels, t stands for the trolley number (1 or 3), c for the chamber slot label in
2348 trolley t and p for the partition label (A, B, C or D depending on the chamber layout) as explained
2349 in Chapter ??.

2350 In the context of GIF++, an extra script called by the webDCS is called to extract the histograms
2351 from the ROOT files. The histograms are then stored in PNG and PDF formats into the correspond-
2352 ing folder (a single folder per HV step, so per ROOT file). the goal is to then display the histograms
2353 on the Data Quality Monitoring (DQM) page of the webDCS in order for the users to control the
2354 quality of the data taking at the end of data taking. An example of histogram organisation is given
2355 below:

2356



2358 Here can put some screens from the webDCS to show the DQM and the plots available to users.

2359

2360 B.2.1.2 CSV files

2361 Moreover, up to 3 CSV files can be created depending on which ones of the 3 input files were in the

2362 data folder:

- 2363 • Offline-Corrupted.csv , is used to keep track of the amount of data that was corrupted and**
- 2364 removed from old data format files that don't contain any data quality flag.**
- 2365 • Offline-Current.csv , contains the summary of the currents and voltages applied on each**
- 2366 RPC HV channel.**
- 2367 • Offline-L0-EffC1.csv , is used to write the efficiencies, cluster size and cluster multiplicity**
- 2368 of efficiency runs. Note that L0 refers here to *Level 0* and means that the results of efficiency and**
- 2369 clusterization are a first approximation calculated without performing any muon tracking in**

2370 between the different detectors. This offline tool provides the user with a preliminar calculation
 2371 of the efficiency and of the muon event parameters. Another analysis software especially
 2372 dedicated to muon tracking is called on selected data to retrieve the results of efficiency and
 2373 muon clusterization using a tracking algorithm to discriminate noise or gamma from muons
 2374 as muons are the only particles that pass through the full setup, leaving hits than can be used
 2375 to reconstruct their tracks.

- 2376 • `Offline-Rate.csv`, is used to write the noise or gamma rates measured in the detector readout
 2377 partitions.

2378 Note that these 4 CSV files are created along with their *headers* (`Offline-[...]-Header.csv`
 2379 containing the names of each data columns) and are automatically merged together when the offline
 2380 analysis tool is called from the webDCS, contrary to the case where the tool is runned locally from
 2381 the terminal as the merging bash script is then not called. Thus, the resulting files, used to make
 2382 official plots, are:

- 2383 • `Corrupted.csv`,
 2384 • `Current.csv`,
 2385 • `L0-EffCl.csv`.
 2386 • `Rate.csv`.

2387 B.3 Analysis inputs and information handling

2388 The usage of the Offline Analysis tool as well as its output have been presented in the previous section.
 2389 It is now important to dig further and start looking at the source code and the inputs necessary
 2390 for the tool to work. Indeed, other than the raw ROOT data files that are analysed, more information
 2391 needs to be imported inside of the program to perform the analysis such as the description of the
 2392 setup inside of GIFT++ at the time of data taking (number of trolleys, of RPCs, dimensions of the
 2393 detectors, etc...) or the mapping that links the TDC channels to the coresponding RPC channels in
 2394 order to translate the TDC information into human readable data. 2 files are used to transmit all this
 2395 information:
 2396

- 2397 • `Dimensions.ini`, that provides the necessary setup and RPC information, and
 2398 • `ChannelsMapping.csv`, that gives the link between the TDC and RPC channels as well as the
 2399 *mask* for each channel (masked or not?).

2400 B.3.1 Dimensions file and InFile parser

2401 This input file, present in every data folder, allows the analysis tool to know of the number of active
 2402 trolleys, the number of active RPCs in those trolleys, and the details about each RPCs such as
 2403 the number of RPC gaps, the number of pseudo-rapidity partitions (for CMS-like prototypes), the
 2404 number of strips per partion or the dimensions. To do so, there are 3 types of groups in the INI file
 2405 architecture. A first general group, appearing only once at the head of the document, gives information
 2406 about the number of active trolleys as well as their IDs, as presented in Source Code B.1. For

2407 each active trolley, a group similar to Source Code B.2 can be found containing information about
 2408 the number of active detectors in the trolley and their IDs. Each trolley group as a `Tt` name format,
 2409 where `t` is the trolley ID. Finally, for each detector stored in slots of an active trolley, there is a group
 2410 providing information about their names and dimensions, as shown in Source Code B.3. Each slot
 2411 group as a `TtSs` name format, where `s` is the slot ID of trolley `t` where the active RPC is hosted.

```
2412 [General]
2413 nTrolleys=2
  TrolleysID=13
```

2414 *Source Code B.1: Example of `[General]` group as might be found in `Dimensions.ini`. In Gif++, only 2 trolleys are available to hold RPCs and place them inside of the bunker for irradiation. The IDs of the trolleys are written in a single string as "13" and then read character by character by the program.*

```
2415 [T1]
  nSlots=4
  SlotsID=1234
```

2416 *Source Code B.2: Example of trolley group as might be found in `Dimensions.ini`. In this example, the file tells that there are 4 detectors placed in the holding slots of the trolley `T1` and that their IDs, written as a single string variable, are 1, 2, 3 and 4.*

```
2417 [T1S1]
  Name=RE2-2-NPD-BARC-8
  Partitions=3
  Gaps=3
  Gap1=BOT
  Gap2=TN
  Gap3=TW
  AreaGap1=11694.25
  AreaGap2=6432
  AreaGap3=4582.82
  Strips=32
  ActiveArea-A=157.8
  ActiveArea-B=121.69
  ActiveArea-C=93.03
```

2418 *Source Code B.3: Example of slot group as might be found in `Dimensions.ini`. In this example, the file provides information about a detector named `RE2-2-NPD-BARC-8`, having 3 pseudo-rapidity readout partitions and stored in slot `S1` of trolley `T1`. This is a CMS RE2-2 type of detector. This information will then be used for example to compute the rate per unit area calculation.*

2419 This information is readout and stored in a C++ object called `IniFile`, that parses the information
 2420 in the INI input file and stores it into a local buffer for later use. This INI parser is the exact same
 2421 one that was previously developed for the Gif++ DAQ and described in Appendix A.5.2.

2422 B.3.2 TDC to RPC link file and Mapping

2423 The same way the INI dimension file information is stored using `map`, the channel mapping and mask
 2424 information is stored and accessed through `map`. First of all, the mapping CSV file is organised into
 2425 3 columns separated by tabulations (and not by commas, as expected for CSV files as it is easier using
 2426 streams to read tab or space separated data using C++):

2427

2428 RPC_channel TDC_channel mask

2429 using as formatting for each field:

2430

2431	TSCCC	TCCC	M
------	-------	------	---

2432 TSCCC is a 5-digit integer where τ is the trolley ID, s the slot ID in which the RPC is held insite
 2433 the trolley τ and ccc is the RPC channel number, or *strip* number, that can take values up to
 2434 3-digits depending on the detector,

2435 TCCC is a 4 digit integer where τ is the TDC ID, ccc is the TDC channel number that can take values
 2436 in between 0 and 127, and

2437 M is a 1-digit integer indicating if the channel should be considered ($M = 1$) or discarded ($M = 0$)
 2438 during analysis.

2439 This mapping and masking information is readout and stored thanks to the object `Mapping`, pre-
 2440 sented in Source Code B.4. Similarly to `IniFile` objects, this class has private methods. The first
 2441 one, `Mapping::CheckIfNewLine()` is used to find the newline character '`\n`' or return character
 2442 '`\r`' (depending on which kind of operating system interacted with the file). This is used for the
 2443 simple reason that the masking information has been introduced only during the year 2017 but the
 2444 channel mapping files exist since 2015 and the very beginning of data taking at GIF++. This means
 2445 that in the older data folders, before the upgrade, the channel mapping file only had 2 columns, the
 2446 RPC channel and the TDC channel. For compatibility reasons, this method helps controling the
 2447 character following the readout of the 2 first fields of a line. In case any end of line character is
 2448 found, no mask information is present in the file and the default $M = 1$ is used. On the contrary, if
 2449 the next character was a tabulation or a space, the mask information is present.

2450 Once the 3 fields have been readout, the second private method `Mapping::CheckIfTDCCh()` is
 2451 used to control that the TDC channel is an existing TDC channel. Finally, the information is stored
 2452 into 3 different maps (`Link`, `ReverseLink` and `Mask`) thanks to the public method `Mapping::Read()`.
 2453 `Link` allows to get the RPC channel by knowing the TDC channel while `ReverseLink` does the op-
 2454 posite by returning the TDC channel by knowing the RPC channel. Finally, `Mask` returns the mask
 2455 associated to a given RPC channel.

```

2456 typedef map<Uint,Uint> MappingData;

2457 class Mapping {
2458     private:
2459         bool          CheckIfNewLine(char next);
2460         bool          CheckIfTDCCh(Uint channel);
2461         string        FileName;
2462         MappingData  Link;
2463         MappingData  ReverseLink;
2464         MappingData  Mask;
2465         int           Error;
2466
2467     public:
2468         Mapping();
2469         Mapping(string baseName);
2470         ~Mapping();
2471
2472         void SetFileName(const string filename);
2473         int  Read();
2474         Uint GetLink(Uint tdcchannel);
2475         Uint GetReverse(Uint rpcchannel);
2476         Uint GetMask(Uint rpcchannel);
2477     };

```

2458 *Source Code B.4: Description of C++ object Mapping used as a parser for the channel mapping and mask file.*

2459 B.4 Description of GIF++ setup within the Offline Analysis tool

2460 In the previous section, the tool input files have been discussed. The dimension file information is
 2461 stored in a map hosted by the `IniFile` object. But this information is then used to create a series of
 2462 new objects that helps defining the GIF++ infrastructure directly into the Offline Analysis. Indeed,
 2463 from the `RPC`, to the more general `Infrastructure`, every element of the GIF++ infrastrucutre is
 2464 recreated for each data analysis based on the information provided in input. All this information
 2465 about the infrastructure will be used to assign each hit signal to a specific strip channel of a specific
 2466 detector, and having a specific active area. This way, rate per unit area calculation is possible.
 2467

2468 B.4.1 RPC objects

2469 `RPC` objects have been developped to represent physical active detectors in GIF++ at the moment
 2470 of data taking. Thus, there are as many `RPC` objects created during the analysis than there were
 2471 active RPCs tested during a run. Each `RPC` hosts the information present in the corresponding INI
 2472 slot group, as shown in B.3, and organises it using a similar architecture. This can be seen from
 2473 Source B.5.

2474 To make the object more compact, the lists of gap labels, of gap active areas and strip active
 2475 areas are stored into `vector` dynamical containers. `RPC` objects are always contructed thanks to the
 2476 dimension file information stored into the `IniFILE` and their ID, using the format `TtSs`. Using the
 2477 `RPC` ID, the constructor calls the methods of `IniFILE` to initialise the `RPC`. The other constructors
 2478 are not used but exist in case of need. Finally, some getters have been written to access the different
 2479 private parameters storing the detector information.

```

2480
class RPC{
    private:
        string      name;           //RPC name as in webDCS database
        Uint        nGaps;          //Number of gaps in the RPC
        Uint        nPartitions;    //Number of partitions in the RPC
        Uint        nStrips;         //Number of strips per partition
        vector<string> gaps;       //List of gap labels (BOT, TOP, etc...)
        vector<float>  gapGeo;        //List of gap active areas
        vector<float>  stripGeo;      //List of strip active areas

    public:
        RPC();
        RPC(string ID, IniFile* geofile);
        RPC(const RPC& other);
        ~RPC();
        RPC& operator=(const RPC& other);

        string GetName();
        Uint GetNGaps();
        Uint GetNPartitions();
        Uint GetNStrips();
        string GetGap(Uint g);
        float GetGapGeo(Uint g);
        float GetStripGeo(Uint p);
};

```

2482 *Source Code B.5: Description of C++ objects RPC that describe each active detectors used during data taking.*

2483 B.4.2 Trolley objects

2484 Trolley objects have been developped to represent physical active trolleys in GIFT++ at the moment
 2485 of data taking. Thus, there are as many trolley objects created during the analysis than there were
 2486 active trolleys hosting tested RPCs during a run. Each Trolley hosts the information present in the
 2487 corresponding INI trolley group, as shown in B.2, and organises it using a similar architecture. In
 2488 addition to the information hosted in the INI file, these object have a dynamical container of RPC
 2489 objects, representing the active detectors the active trolley was hosting at the time of data taking.
 2490 This can been seen from Source Code B.6.

2491 Trolley objects are always contructed thanks to the dimension file information stored into the
 2492 IniFILE and their ID, using the format Tt. Using the Trolley ID, the constructor calls the methods
 2493 of IniFILE to initialise the Trolley. Retrieving the information of the RPC IDs via SlotsID, a new
 2494 RPC is constructed and added to the container RPCs for each character in the ID string. The other
 2495 constructors are not used but exist in case of need. Finally, some getters have been written to access
 2496 the different private parameters storing the trolley and detectors information.

```

2497
class Trolley{
    private:
        Uint          nSlots; //Number of active RPCs in the considered trolley
        string        SlotsID; //Active RPC IDs written into a string
        vector<RPC*> RPCs;   //List of active RPCs

    public:
        //Constructors, destructor and operator =
        Trolley();
        Trolley(string ID, IniFile* geofile);
        Trolley(const Trolley& other);
        ~Trolley();
        Trolley& operator=(const Trolley& other);

        //Get GIFTrolley members
        Uint  GetNSlots();
        string GetSlotsID();
        Uint   GetSlotID(Uint s);

        //Manage RPC list
        RPC*  GetRPC(Uint r);
        void  DeleteRPC(Uint r);

        //Methods to get members of RPC objects stored in RPCs
        string GetName(Uint r);
        Uint   GetNGaps(Uint r);
        Uint   GetNPartitions(Uint r);
        Uint   GetNStrips(Uint r);
        string GetGap(Uint r, Uint g);
        float  GetGapGeo(Uint r, Uint g);
        float  GetStripGeo(Uint r, Uint p);
    };

```

Source Code B.6: Description of C++ objects `Trolley` that describe each active trolley used during data taking.

2500 B.4.3 Infrastructure object

2501 The `Infrastructure` object has been developped to represent the GIFT++ bunker area dedicated to
 2502 CMS RPC experiments. With this very specific object, all the information about the CMS RPC
 2503 setup within GIFT++ at the moment of data taking is stored. It hosts the information present in the
 2504 corresponding INI general group, as shown in B.1, and organises it using a similar architecture. In
 2505 addition to the information hosted in the INI file, this object have a dynamical container of `Trolley`
 2506 objects, representing the active tolleys in GIFT++ area. This can be seen from Source Code B.7.

2507 The `Infrastructure` object is always contructed thanks to the dimension file information stored
 2508 into the `IniFILE`. Retrieving the information of the trolley IDs via `TrolleysID`, a new `Trolley` is
 2509 constructed and added to the container `Trolleys` for each character in the ID `string`. By extension,
 2510 it is easy to understand that the process described in Section B.4.2 for the construction of RPCs
 2511 takes place when a trolley is constructed. The other constructors are not used but exist in case of
 2512 need. Finally, some getters have been written to access the different private parameters storing the
 2513 infrastructure, tolleys and detectors information.

```

2514
class Infrastructure {
    private:
        Uint             nTrolleys;   //Number of active Trolleys in the run
        string          TrolleysID;  //Active trolley IDs written into a string
        vector<Trolley*> Trolleys;  //List of active Trolleys (struct)

    public:
        //Constructors and destructor
        Infrastructure();
        Infrastructure(IniFile* geofile);
        Infrastructure(const Infrastructure& other);
        ~Infrastructure();
        Infrastructure& operator=(const Infrastructure& other);

        //Get Infrastructure members
        Uint  GetNTrolleys();
        string GetTrolleysID();
        Uint   GetTrolleyID(Uint t);

2515
        //Manage Trolleys
        Trolley* GetTrolley(Uint t);
        void     DeleteTrolley(Uint t);

        //Methods to get members of GIFTrolley objects stored in Trolleys
        Uint  GetNSlots(Uint t);
        string GetSlotsID(Uint t);
        Uint   GetSlotID(Uint t, Uint s);
        RPC*  GetRPC(Uint t, Uint r);

        //Methods to get members of RPC objects stored in RPCs
        string GetName(Uint t, Uint r);
        Uint   GetNGaps(Uint t, Uint r);
        Uint   GetNPartitions(Uint t, Uint r);
        Uint   GetNStrips(Uint t, Uint r);
        string GetGap(Uint t, Uint r, Uint g);
        float  GetGapGeo(Uint t, Uint r, Uint g);
        float  GetStripGeo(Uint t, Uint r, Uint p);
};


```

Source Code B.7: Description of C++ object *Infrastructure* that contains the full information about CMS RPC experiment in GIF++.

2517 B.5 Handeling of data

2518 As discussed in Appendix A.4.2, the raw data as a `TTree` architecture where every entry is related to
 2519 a trigger signal provided by a muon or a random pulse, whether the goal of the data taking was to
 2520 measure the performance of the detector or the noise/gamma background respectively. Each of these
 2521 entries, referred also as events, contain a more or less full list of hits in the TDC channels to which
 2522 the detectors are connected. To this list of hits corresponds a list of time stamps, marking the arrival
 2523 of the hits within the TDC channel.

2524 The infrastructure of the CMS RPC experiment within GIF++ being defined, combining the
 2525 information about the raw data with the information provided by both the mapping/mask file and the
 2526 dimension file allows to build new physical objects that will help in computing efficiency or rates.

2527 B.5.1 RPC hits

2528 The raw data stored in the ROOT file as output of the GIFT++ DAQ, is readout by the analysis tool
 2529 using the structure `RAWData` presented in Source Code B.9 that differs from the structure presented
 2530 in Appendix A.4.2 as it is not meant to hold all of the data contained in the ROOT file. In this sense,
 2531 this structure is in the case of the offline analysis tool not a dynamical object and will only be storing
 2532 a single event contained in a single entry of the `TTree`.

```
2533
class RPCHit {
    private:
        Uint Channel;      //RPC channel according to mapping (5 digits)
        Uint Trolley;     //0, 1 or 3 (1st digit of the RPC channel)
        Uint Station;     //Slot where is held the RPC in Trolley (2nd digit)
        Uint Strip;       //Physical RPC strip where the hit occurred (last 3
    →   digits)
        Uint Partition;   //Readout partition along eta segmentation
        float TimeStamp; //Time stamp of the arrival in TDC

    public:
        //Constructors, destructor & operator =
        RPCHit();
        RPCHit(Uint channel, float time, Infrastructure* Infra);
        RPCHit(const RPCHit& other);
        ~RPCHit();
        RPCHit& operator=(const RPCHit& other);

        //Get RPCHit members
        Uint GetChannel();
        Uint GetTrolley();
        Uint GetStation();
        Uint GetStrip();
        Uint GetPartition();
        float GetTime();
    };

    typedef vector<RPCHit> HitList;
    typedef struct GIFHitList { HitList rpc[NTROLLEYS][NSLOTS][NPARTITIONS]; }
    →   GIFHitList;

    bool SortHitbyStrip(RPCHit h1, RPCHit h2);
    bool SortHitbyTime(RPCHit h1, RPCHit h2);
}
```

2535 *Source Code B.8: Description of C++ object `RPCHit`.*

```
2536
struct RAWData{
    int iEvent;           //Event i
    int iTDCNHits;        //Number of hits in event i
    int iQFlag;           //Quality flag list (1 flag digit per TDC)
    vector<Uint> *TDCCh; //List of channels giving hits per event
    vector<float> *TDCTS; //List of the corresponding time stamps
};
```

2537 *Source Code B.9: Description of C++ structure `RAWData`.*

2538 Each member of the structure is then linked to the corresponding branch of the ROOT data tree,
 2539 as shown in the example of Source Code B.10, and using the method `GetEntry(int i)` of the ROOT
 2540 class `TTree` will update the state of the members of `RAWData`.

```

2541 TTree* dataTree = (TTree*)dataFile.Get("RAWData");
2542 RAWData data;
2543
2544 dataTree->SetBranchAddress("EventNumber", &data.iEvent);
2545 dataTree->SetBranchAddress("number_of_hits", &data.TDCNHits);
2546 dataTree->SetBranchAddress("Quality_flag", &data.QFlag);
2547 dataTree->SetBranchAddress("TDC_channel", &data.TDCCh);
2548 dataTree->SetBranchAddress("TDC_TimeStamp", &data.TDCTS);

```

2543 *Source Code B.10: Example of link in between RAWData and TTree.*

2544 The data is then analysed entry by entry and to each element of the TDC channel list, a `RPCHit` is
 2545 constructed by linking each TDC channel to the corresponding RPC channel thanks to the `Mapping`
 2546 object. The information carried by the RPC channel format allows to easily retrieve the trolley and
 2547 slot from which the hit was recorded (see section B.3.2). Using these 2 values, the readout partition
 2548 can be found by knowing the strip channel and comparing it with the number of partitions and strips
 2549 per partition stored into the `Infrastructure` object.

2550 Thus `RPCHit` objects are then stored into 3D dynamical list called `GIFHitList` (Source Code B.9)
 2551 where the 3 dimensions refer to the 3 layers of the readout in `GIF++` : in the bunker there are *trolleys*
 2552 (τ) holding detectors in *slots* (s) and each detector readout is divided into 1 or more pseudo-rapidity
 2553 *partitions* (p). Using these 3 information allows to assign an address to each readout partition and
 2554 this address will point to a specific hit list.

2555

2556 B.5.2 Clusters of hits

2557 All the hits contained in the ROOT file have been sorted into the different hit lists through the
 2558 `GIFHitList`. At this point, it is possible to start looking for clusters. A cluster is a group of adjacent
 2559 strips getting hits within a time window of 25 ns. These strips are then assumed to be part of the same
 2560 physical avalanche signal generated by a muon passing through the chamber or by the interaction of
 2561 a gamma stopping into the electrodes of the RPCs.

2562 To keep the cluster information, `RPCCluster` objects have been defined as shown in Source
 2563 Code B.11. Using the information of each individual `RPCHit` taken out of the hit list, it stores
 2564 the cluster size (number of adjacent strips composing the cluster), the first and last hit, the center for
 2565 spatial reconstruction and finally the start and stop time stamps as well as te time spread in between
 2566 the first and last hit.

```

2567
class RPCCluster{
    private:
        Uint ClusterSize; //Size of cluster #ID
        Uint FirstStrip; //First strip of cluster #ID
        Uint LastStrip; //Last strip of cluster #ID
        float Center; //Center of cluster #ID ((first+last)/2)
        float StartStamp; //Time stamp of the earliest hit of cluster #ID
        float StopStamp; //Time stamp of the latest hit of cluster #ID
        float TimeSpread; //Time difference between earliest and latest hits
                           //of cluster #ID
    public:
        //Constructors, destructor & operator =
        RPCCluster();
        RPCCluster(HitList List, Uint cID, Uint cSize, Uint first, Uint firstID);
        RPCCluster(const RPCCluster& other);
        ~RPCCluster();
        RPCCluster& operator=(const RPCCluster& other);

        //Get Cluster members
        Uint GetID();
        Uint GetSize();
        Uint GetFirstStrip();
        Uint GetLastStrip();
        float GetCenter();
        float GetStart();
        float GetStop();
        float GetSpread();
    };

typedef vector<RPCCluster> ClusterList;

//Other functions to build cluster lists out of hit lists
void BuildClusters(HitList &cluster, ClusterList &clusterList);
void Clusterization(HitList &hits, TH1 *hcSize, TH1 *hcMult);

```

2569 *Source Code B.11: Description of C++ object Cluster.*

2570 To investigate the hit list of a given detector partition, the function `Clusterization()` defined
 2571 in `include/Cluster.h` needs the hits in the list to be time sorted. This is achieved by calling func-
 2572 tion `sort()` of library `<algorithm>` using the comparator `SortHitbyTime(RPCHit h1, RPCHit h2)`
 2573 defined in `include/RPCHit.h` that returns `true` if the time stamp of hit `h1` is lower than that of `h2`.
 2574 A first isolation of strips is made only based on time information. All the hits within the 25 ns win-
 2575 dow are taken separately from the rest. Then, this sub-list of hits is sorted this time by ascending
 2576 strip number, using this time the comparator `SortHitbyStrip(RPCHit h1, RPCHit h2)`. Finally, the
 2577 groups of adjacent strips are used to construct `RPCCluster` objects that are then stored in a temporary
 2578 list of clusters that is at the end of the process used to know how many clusters were reconstructed
 2579 and to fill their sizes into an histogram that will allows to know the mean size of muon or gamma
 2580 clusters.

2581

2582 **B.6 DAQ data Analysis**

2583 All the ingredients to analyse GIF++ data have been defined. This section will focus on the different
 2584 part of the analysis performed on the data, from determining the type of data the tool is dealing with

2585 to calculating the rate in each detector or reconstructing muon or gamma clusters.

2586 B.6.1 Determination of the run type

2587 In GIF++, both the performance of the detectors in detecting muons in an irradiated environment and
 2588 the gamma background can be independantly measured. These corresponds to different run types
 2589 and thus, to different TDC settings giving different data to look at.

2590

2591 In the case of performance measurements, the trigger for data taking is provided by the coïncidence
 2592 of several scintillators when muons from the beam passing through the area are detected. Data
 2593 is collected in a 600 ns wide window around the arrival of muons in the RPCs. The expected time
 2594 distribution of hits is shown in Figure B.1a. The muon peak is clearly visible in the center of the
 2595 distribution and is to be extracted from the gamma background that composes the flat part of the
 2596 distribution.

2597 On the other hand, gamma background or noise measurements are focussed on the non muon
 2598 related physics and the trigger needs to be independant from the muons to give a good measurement
 2599 of the gamma/noise distribution as seen by the detectors. The trigger is then provided by a pulse
 2600 generator at a frequency of 300 Hz whose pulse is not likely to be on time with a muon. In order
 2601 to increase the integrated time without increasing the acquisition time too much, the width of the
 2602 acquisition windows are increased to 10 μ s. The time distribution of the hits is expected to be flat, as
 2603 shown by Figure B.1b.

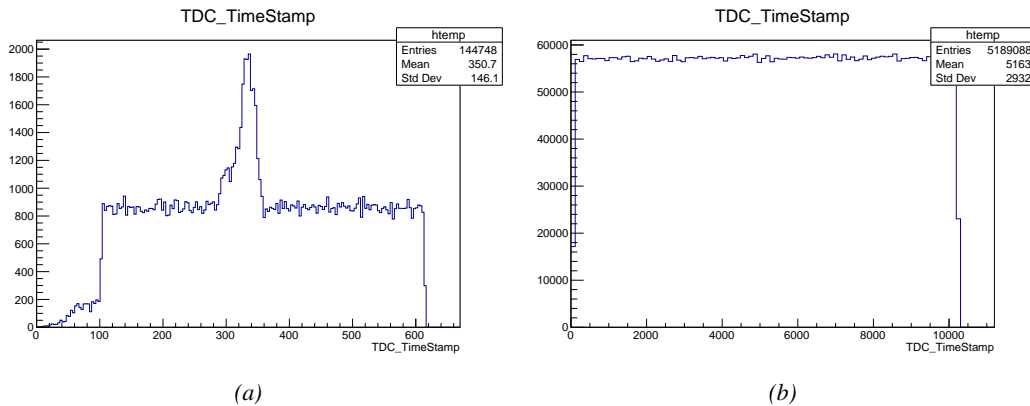


Figure B.1: Example of expected hit time distributions in the cases of efficiency (Figure B.1a) and noise/gamma rate per unit area (Figure B.1b) measurements as extracted from the raw ROOT files. The unit along the x-axis corresponds to ns. The fact that "the" muon peak is not well defined in Figure B.1a is due to the contribution of all the RPCs being tested at the same time that don't necessarily have the same signal arrival time. Each individual peak can have an offset with the ones of other detectors. The inconsistency in the first 100 ns of both time distributions is an artefact of the TDCs and are systematically rejected during the analysis.

2604 The ROOT files include a TTree called RunParameters containing, among other things, the in-
 2605 formation related to the type of run. The run type can then be accessed as described by Source
 2606 Code B.12 and the function IsEfficiencyRun() is then used to determine if the run file is an effi-
 2607 ciency run or, on the contrary, another type of run (noise or gamma measurement).

```

2608
2609     TTree* RunParameters = (TTree*)dataFile.Get("RunParameters");
2610     TString* RunType = new TString();
2611     RunParameters->SetBranchAddress("RunType", &RunType);
2612     RunParameters->GetEntry(0);

```

2610 *Source Code B.12: Access to the run type contained in TTree* RunParameters.*

2611 Finally, the data files will have a slightly different content whether it was collected before or after
2612 October 2017 and the upgrade of the DAQ software that brought a new information into the ROOT
2613 output. This is discussed in Appendix A.4.3 and implies that the analysis will differ a little depending
2614 on the data format. Indeed, as no information on the data quality is stored, in older data files, the cor-
2615 rections for missing events has to be done at the end of the analysis. The information about the type
2616 of data format is stored in the variable **bool** `isNewFormat` by checking the list of branches contained
2617 in the data tree via the methods `TTree::GetListOfBranches()` and `TCollection::Contains()`.

2618 **B.6.2 Beam time window calculation for efficiency runs**

2619 Knowing the run type is important first of all to know the width of the acquisition window to be used
2620 for the rate calculation and finally to be able to seek for muons. Indeed, the peak that appears in the
2621 time distribution for each detectors is then fitted to extract the most probable time window in which
2622 the tool should look for muon hits. The data outside of this time window is then used to evaluate the
2623 noise or gamma background the detector was subjected to during the data taking. Computing the
2624 position of the peak is done calling the function `SetBeamWindow()` defined in file `src/RPCHit.cc` that
2625 loops a first time on the data. The data is first sorted in a 3D array of 1D histograms (`GIFH1Array`, see
2626 `include/types.h`). Then the location of the highest bin is determined using `TH1::GetMaximumBin()`
2627 and is used to define a window in which a gaussian fit will be applied to compute the peak width.
2628 This window is a 80 ns defined by Formula B.1 around the central bin.

$$t_{center}(ns) = bin \times width_{bin}(ns) \quad (\text{B.1a})$$

$$[t_{low}; t_{high}] = [t_{center} - 40; t_{center} + 40] \quad (\text{B.1b})$$

2629 Before the fit is performed, the average number of noise/gamma hits per bin is evaluated using
2630 the data outside of the fit window. Excluding the first 100 ns, the average number of hits per bin
2631 due to the noise or gamma is defined by Formula B.2 after extracting the amount of hits in the time
2632 windows $[100; t_{low}]$ and $[t_{high}; 600]$ thanks to the method `TH1::Integral()`. This average number
2633 of hits is then subtracted to every bin of the 1D histogram, in order to *clean* it from the noise or
2634 gamma contribution as much as possible to improve the fit quality. Bins where $\langle n_{hits} \rangle$ is greater
2635 than the actual bin content are set to 0.

$$\Delta t_{noise}(ns) = 600 \overbrace{-t_{high} + t_{low}}^{-80ns} - 100 = 420ns \quad (\text{B.2a})$$

$$\langle n_{hits} \rangle = width_{bin}(ns) \times \frac{\sum_{t=100}^{t_{low}} + \sum_{t=t_{high}}^{600}}{\Delta t_{noise}(ns)} \quad (\text{B.2b})$$

2636 Finally, the fit parameters are extracted and saved for each detector in 3D arrays of **float**
2637 (`muonPeak`, see `include/types.h`), a first one for the mean arrival time of the muons, `PeakTime`,

2638 and a second one for the width of the peak, `PeakWidth`. The width is defined as 6σ of the gaussian
 2639 fit. The same settings are applied to every partitions of the same detector. To determine which one
 2640 of the detector's partitions is directly illuminated by the beam, the peak height of each partition is
 2641 compared and the highest one is then used to define the peak settings.

2642 **B.6.3 Data loop and histogram filling**

2643 3D arrays of histogram are created to store the data and display it on the DQM of G4F++ webDCS
 2644 for the use of shifters. These histograms, presented in section B.2.1.1, are filled while looping on
 2645 the data. Before starting the analysis loop, it is necessary to control the entry quality for the new
 2646 file formats featuring `QFlag`. If the `QFlag` value for this entry shows that 1 TDC or more have a
 2647 CORRUPTED flag, then this event is discarded. The loss of statistics is low enough to be neglected.
 2648 `QFlag` is controlled using the function `IsCorruptedEvent()` defined in `src/utils.cc`. As explained
 2649 in Appendix A.4.3, each digit of this integer represent a TDC flag that can be 1 or 2. Each 2 is
 2650 the sign of a CORRUPTED state. Then, the data is accessed entry by entry in the ROOT `TTree` using
 2651 `RAWData` and each hit in the hit list is assigned to a detector channel and saved in the corresponding
 2652 histograms. In the first part of the analysis, in which the loop over the ROOT file's content is
 2653 performed, the different steps are:

2654 **1- RPC channel assignment and control:** a check is done on the RPC channel extracted thanks
 2655 to the mapping via the method `Mapping::GetLink()`. If the channel is not initialised and is 0, or if
 2656 the TDC channel was greater than 5127, the hit is discarded. This means there was a problem in the
 2657 mapping. Often a mapping problem leads to the crash of the offline tool.

2658 **2- Creation of a `RPCHit` object:** to easily get the trolley, slot and partition in which the hit has
 2659 been assigned, this object is particularly helpful.

2660 **3- General histograms are filled:** the hit is filled into the time distribution and the general hit
 2661 distribution histograms, and if the arrival time is within the first 100 ns, it is discarded and nothing
 2662 else happens and the loop proceeds with the next hit in the list.

2663 **4- Multiplicity counter:** the hit multiplicity counter of the corresponding detectors incremented.

2664 **5-a- Efficiency runs - Is the hit within the peak window? :** if the peak is contained in the peak
 2665 window previously defined in section B.6.2, the hit is filled into the beam hit profile histogram of
 2666 the corresponding chamber, added into the list of muon hits and increments the counter of *in time*
 2667 hits. The term *in time* here refers to the hits that are likely to be muons by arriving in the expected
 2668 time window. If the hit is outside of the peak window, it is filled into the noise profile histogram
 2669 of the corresponding detector, added into the list of noise/gamma hits and increments the counter of
 2670 noise/gamma hits.

2671 **5-b- Noise/gamma rate runs - Noise histograms are filled:** the hit is filled into the noise profile
 2672 histogram of the corresponding detector, added into the list of noise/gamma hits and increments the
 2673 counter of noise/gamma hits.

2675 After the loop on the hit list of the entry is over, the next step is to clusterize the 3D lists filled
 2676 in the previous steps. A 3D loop is then started over the active trolley, slot and RPC partitions to
 2677 access these objects. Each `NoiseHitList` and `MuonHitList`, in case of efficiency run, are clusterized
 2678 as described in section B.5.2. There corresponding cluster size and multiplicity histograms are filled
 2679 at the end of the clustering process. Then, the efficiency histogram is filled in case of efficiency run.
 2680 The selection is simply made by checking whether the RPC detected signals in the peak window
 2681 during this event. Nevertheless, it is useful to highlight that at this level, it is not possible yet to
 2682 discriminate in between a muon hit and noise or gamma hit. Thus, `MuonCSize_H`, `MuonCMult_H`
 2683 and `Efficiency0_H` are subjected to noise and gamma contamination. This contamination will be
 2684 estimated and corrected at the moment the results will be written into output CSV files. Finally, the
 2685 loop ends on the filling of the general hit multiplicity histogram.

2686 **B.6.4 Results calculation**

2687 As mentioned in section B.2.1, the analysis of DAQ data provides the user with 3 CSV files and
 2688 a ROOT file associated to each and every ROOT data file. The fourth CSV file is provided by the
 2689 extraction of the CEAN main frame data monitored during data taking and will be discussed later.
 2690 After looping on the data in the previous part of the analysis macro, the output files are created and a
 2691 3D loop on each RPC readout partitions is started to extract the histograms parameters and compute
 2692 the final results.

2693

2694 **B.6.4.1 Rate normalisation**

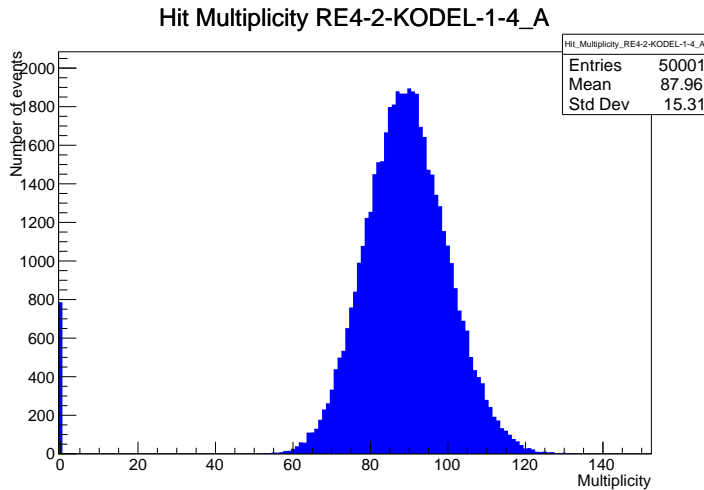


Figure B.2: The effect of the quality flag is explained by presenting the reconstructed hit multiplicity of a data file without `Quality_flag`. The artificial high content of bin 0 is the effect of corrupted data.

2695 To analyse old data format files, not containing any quality flag, it is needed to estimate the amount
 2696 of corrupted data via a fit as the corrupted data will always fill events with a fake "0 multiplicity".
 2697 Indeed, as no hits were stored in the DAQ ROOT files, these events artificially contribute to fill
 2698 the bin corresponding to a null multiplicity, as shown in Figure B.2. In the case the mean of the

hit multiplicity distribution is high, the contribution of the corrupted data can easily be evaluated for later correction by comparing the level of the bin at multiplicity 0 and of a skew fit curve that should indicate a value consistent with 0. A skew fit has been chosen over a Poisson fit as it was giving better results for lower mean multiplicity values. Nevertheless, for low irradiation cases, as explained in Appendix A.4.3, the hit multiplicity distribution mean is, on the contrary, rather small and the probability to record events without hits can't be considered small anymore, leading to a difficult and non-reliable estimation of the corruption. As can be seen in Source Code B.13, conditions have been applied to prevent bad fits and wrong corruption estimation in cases where :

- The difference in between the data for multiplicity 1 and the corresponding fit value should be lower than 1% of the total amount of data : $\frac{|n_{m=1} - sk(1)|}{N_{tot}} < 0.01$ where $n_{m=1}$ is the number of entries with multiplicity 1, $sk(1)$ the value of the skew fit, as defined by Formula 4.3, for multiplicity 1 and N_{tot} the total number of entries.

- The amount of data contained in the multiplicity 0 bin should not exceed 40% : $\frac{n_{m=0}}{N_{tot}} \leq 0.4$ where $n_{m=0}$ is the number of entries with multiplicity 0. This number has been determined to be the maximum to be able to separate the excess of data due to corruption from the hit multiplicity distribution.

Those 2 conditions need to be fulfilled to estimate the corruption of old data format files. If the fit was successful, the level of corruption is written in `Offline-Corrupted.csv` and the number of corrupted entries, refered as the integer `nEmptyEvent`, is subtracted from the total number of entries when the rate normalisation factor is computed as explicit in Source Code B.13. Note that for new data format files, the number of corrupted entries being set to 0, the definition of `rate_norm` stays valid.

```

2721
if(!isNewFormat){
    TF1* GaussFit = new TF1("gaussfit","[0]*exp(-0.5*((x-[1])/[2])**2)",0,Xmax);
    GaussFit->SetParameter(0,100);
    GaussFit->SetParameter(1,10);
    GaussFit->SetParameter(2,1);
    HitMultiplicity_H.rpc[T][S][p]->Fit(GaussFit,"LIQR","",0.5,Xmax);

    TF1* SkewFit = new TF1("skewfit","[0]*exp(-0.5*((x-[1])/[2])**2) / (1 +
→ exp(-[3]*(x-[4])))",0,Xmax);
    SkewFit->SetParameter(0,GaussFit->GetParameter(0));
    SkewFit->SetParameter(1,GaussFit->GetParameter(1));
    SkewFit->SetParameter(2,GaussFit->GetParameter(2));
    SkewFit->SetParameter(3,1);
    SkewFit->SetParameter(4,1);
    HitMultiplicity_H.rpc[T][S][p]->Fit(SkewFit,"LIQR","",0.5,Xmax);

    double fitValue = SkewFit->Eval(1,0,0,0);
    double dataValue = (double)HitMultiplicity_H.rpc[T][S][p]->GetBinContent(2);
    double difference = TMath::Abs(dataValue - fitValue);
    double fitTOdataVSentries_ratio = difference / (double)nEntries;
    bool isFitGOOD = fitTOdataVSentries_ratio < 0.01;

2722
    double nSinglehit = (double)HitMultiplicity_H.rpc[T][S][p]->GetBinContent(1);
    double lowMultRatio = nSinglehit / (double)nEntries;
    bool isMultLOW = lowMultRatio > 0.4;

    if(isFitGOOD && !isMultLOW){
        nEmptyEvent = HitMultiplicity_H.rpc[T][S][p]->GetBinContent(1);
        nPhysics = (int)SkewFit->Eval(0,0,0,0);
        if(nPhysics < nEmptyEvent)
            nEmptyEvent = nEmptyEvent-nPhysics;
    }
}

double corrupt_ratio = 100.*(double)nEmptyEvent / (double)nEntries;
outputCorrCSV << corrupt_ratio << '\t';

float rate_norm = 0.;
float stripArea = GIFIInfra->GetStripGeo(tr,sl,p);

if(IsEfficiencyRun(RunType)){
    float noiseWindow = BMTDCWINDOW - TIMEREJECT - 2*PeakWidth.rpc[T][S][p];
    rate_norm = (nEntries-nEmptyEvent)*noiseWindow*1e-9*stripArea;
} else
    rate_norm = (nEntries-nEmptyEvent)*RDMNOISEWDW*1e-9*stripArea;

```

Source Code B.13: Definition of the rate normalisation variable. It takes into account the number of non corrupted entries and the time window used for noise calculation, to estimate the total integrated time, and the strip active area to express the result as rate per unit area.

2724 B.6.4.2 Rate and activity

2725 At this point, the strip rate histograms, StripNoiseProfile_H.rpc[T][S][p], only contain an in-
2726 formation about the total number of noise or rate hits each channel received during the data taking.
2727 As described in Source Code B.14, a loop on the strip channels will be used to normalise the content
2728 of the rate distribution histogram for each detector partitions. The initial number of hits recorded for
2729 a given bin will be extracted and 2 values will be computed:

- 2730 ● the strip rate, defined as the number of hits recorded in the bin normalised like described in
 2731 the previous section, using the variable `rate_norm`, and

- 2732 ● the strip activity, defined as the number of hits recorded in the bin normalised to the average
 2733 number of hits per bin contained in the partition histogram, using the variable `averageNhit`.
 2734 This value provides an information on the homogeneity of the detector response to the gamma
 2735 background or of the detector noise. An activity of 1 corresponds to an average response.
 2736 Above 1, the channel is more active than the average and bellow 1, the channel is less active.

```

int nNoise = StripNoiseProfile_H.rpc[T][S][p]->GetEntries();
float averageNhit = (nNoise>0) ? (float)(nNoise/nStripsPart) : 1.;

for(Uint st = 1; st <= nStripsPart; st++) {
    float stripRate =
        StripNoiseProfile_H.rpc[T][S][p]->GetBinContent(st)/rate_norm;
    float stripAct =
        StripNoiseProfile_H.rpc[T][S][p]->GetBinContent(st)/averageNhit;

    StripNoiseProfile_H.rpc[T][S][p]->SetBinContent(st,stripRate);
    StripActivity_H.rpc[T][S][p]->SetBinContent(st,stripAct);
}

```

2738 *Source Code B.14: Description of the loop that allows to set the content of each strip rate and strip activity
 channel for each detector partition.*

2739 On each detector partitions, which are readout by a single FEE, all the channels are not processed
 2740 by the same chip. Each chip can give a different noise response and thus, histograms using a chip
 2741 binning are used to investigate chip related noise behaviours. The average values of the strip rate
 2742 or activity grouped into a given chip are extracted using the using the function `GetChipBin()` and
 2743 stored in dedicated histograms as described in Source Codes B.15 and B.16 respectively.

```

float GetChipBin(TH1* H, Uint chip){
    Uint start = 1 + chip*NSTRIPSCHIP;
    int nActive = NSTRIPSCHIP;
    float mean = 0.;

    for(Uint b = start; b <= (chip+1)*NSTRIPSCHIP; b++) {
        float value = H->GetBinContent(b);
        mean += value;
        if(value == 0.) nActive--;
    }

    if(nActive != 0) mean /= (float)nActive;
    else mean = 0.;

    return mean;
}

```

2746 *Source Code B.15: Function used to compute the content of a bin for an histogram using chip binning.*

```

2747   for(UInt ch = 0; ch < (nStripsPart/NSTRIPSCHIP); ch++) {
2748     ChipMeanNoiseProf_H.rpc[T][S][p]->
2749       SetBinContent(ch+1,GetChipBin(StripNoiseProfile_H.rpc[T][S][p],ch));
2750     ChipActivity_H.rpc[T][S][p]->
2751       SetBinContent(ch+1,GetChipBin(StripActivity_H.rpc[T][S][p],ch));
2752   }

```

Source Code B.16: Description of the loop that allows to set the content of each chip rate and chip activity bins for each detector partition knowing the information contained in the corresponding strip distribution histograms.

The activity variable is used to evaluate the homogeneity of the detector response to background or of the detector noise. The homogeneity h_p of each detector partition can be evaluated using the formula $h_p = \exp(-\sigma_p^R / \langle R \rangle_p)$, where $\langle R \rangle_p$ is the partition mean rate and σ_p^R is the rate standard deviation calculated over the partition channels. The more homogeneously the rates are distributed and the smaller will σ_p^R be, and the closer to 1 will h_p get. On the contrary, if the standard deviation of the channel's rates is large, h_p will rapidly get to 0. This value is saved into histograms as shown in Source Code B.17 and could in the future be used to monitor through time, once extracted, the evolution of every partition homogeneity. This could be of great help to understand the apparition of eventual hot spots due to ageing of the chambers subjected to high radiation levels. The monitored homogeneity information could then be combined with a monitoring of the activity of each individual channel in order to have a finer information. Monitoring tools have been suggested and need to be developed for this purpose.

```

2761   float MeanPartSDev = GetTH1StdDev(StripNoiseProfile_H.rpc[T][S][p]);
2762   float strip_homog = (MeanPartRate==0)
2763     ? 0.
2764     : exp(-MeanPartSDev/MeanPartRate);
2765   StripHomogeneity_H.rpc[T][S][p]->Fill("exp -#left(#frac{\#sigma_{Strip}
2766     \rightarrow Rate}{\#mu_{Strip Rate}}\#right)",strip_homog);
2767   StripHomogeneity_H.rpc[T][S][p]->GetYaxis()->SetRangeUser(0.,1.);
2768
2769   float ChipStDevMean = GetTH1StdDev(ChipMeanNoiseProf_H.rpc[T][S][p]);
2770   float chip_homog = (MeanPartRate==0)
2771     ? 0.
2772     : exp(-ChipStDevMean/MeanPartRate);
2773   ChipHomogeneity_H.rpc[T][S][p]->Fill("exp -#left(#frac{\#sigma_{Chip}
2774     \rightarrow Rate}{\#mu_{Chip Rate}}\#right)",chip_homog);
2775   ChipHomogeneity_H.rpc[T][S][p]->GetYaxis()->SetRangeUser(0.,1.);

```

Source Code B.17: Storage of the homogeneity into dedicated histograms.

B.6.4.3 Strip masking tool

The offline tool is automatically called at the end of each data taking to analyse the data and offer the shifter DQM histograms to control the data quality. After the histograms have been published online in the DQM page, the shifter can decide to mask noisy or dead channels that will contribute to bias the final rate calculation by editing the mask column of `ChannelsMapping.csv` as can be seen in Figure B.3.

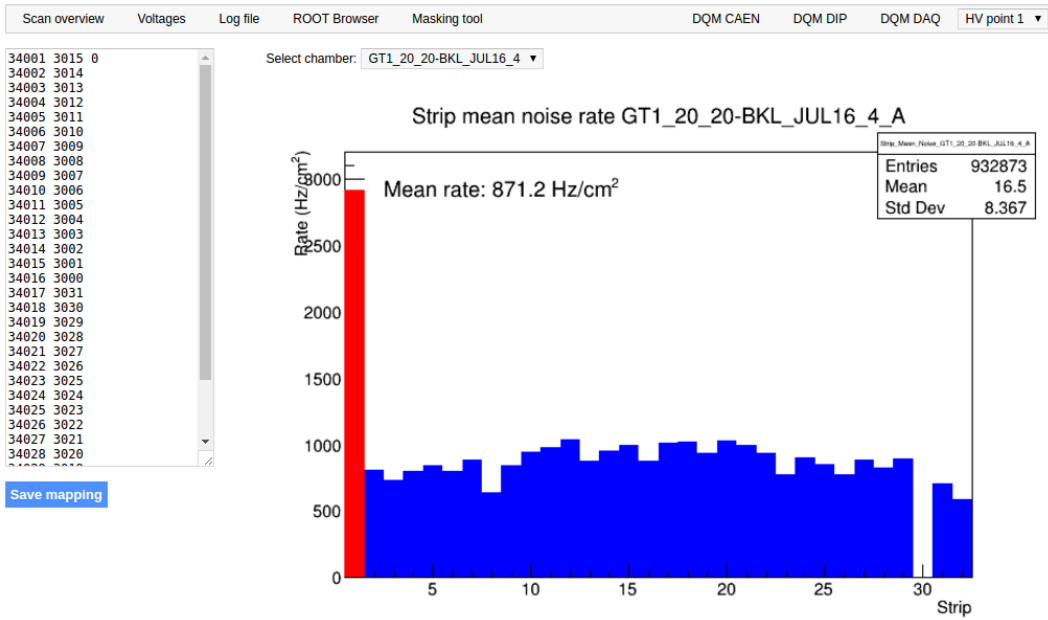


Figure B.3: Display of the masking tool page on the webDCS. The window on the left allows the shifter to edit ChannelsMapping.csv. To mask a channel, it only is needed to set the 3rd field corresponding to the strip to mask to 0. It is not necessary for older mapping file formats to add a 1 for each strip that is not masked as the code is versatile and the default behaviour is to consider missing mask fields as active strips. The effect of the mask is directly visible for noisy channels as the corresponding bin turns red. The global effect of masking strips will be an update of the rate value showed on the histogram that will take into consideration the rejected channels.

2770 From the code point of view, the function `GetTH1Mean()` is used to retrieve the mean rate par-
 2771 tition by partition after the rates have been calculated strip by strip and filled into the histograms
 2772 `StripNoiseProfile_H.rpc[T][S][p]`, as described through Source Code B.18.

2773 Once the mask for each rejected channel has been updated, the shifter can manually run the of-
 2774 fline tool again to update the DQM plots, now including the masked strips, as well the rate results
 2775 written in the output CSV file `Offline-Rate.csv`. If not done during the shifts, the strip masking
 2776 procedure needs to be carefully done by the person in charge of data analysis on the scans that were
 2777 selected to produce the final results.

```

2778
2779     float GetTH1Mean(TH1* H) {
2780         int nBins = H->GetNbinsX();
2781         int nActive = nBins;
2782         float mean = 0.;
2783
2784         for(int b = 1; b <= nBins; b++) {
2785             float value = H->GetBinContent(b);
2786             mean += value;
2787             if(value == 0.) nActive--;
2788         }
2789
2790         if(nActive != 0) mean /= (float)nActive;
2791         else mean = 0.;
2792
2793         return mean;
2794     }

```

Source Code B.18: The function `GetTH1Mean()` is used to return the mean along the y-axis of `TH1` histograms containing rate information. In order to take into account masked strips whose rate is set to 0, the function looks for masked channels and decrement the number of active channels for each null value found.

2781 B.6.4.4 Output CSV files filling

2782 All the histograms have been filled. Parameters will then be extracted from them to compute the
 2783 final results that will later be used to produce plots. Once the results have been computed, the very
 2784 last step of the offline macro is to write these values into the corresponding CSV outputs. Aside of
 2785 the file `Offline-Corrupted.csv`, 2 CSV files are being written by the macro `offlineAnalysis()`,
 2786 `Offline-Rates.csv` and `Offline-L0-EffCl.csv` that respectively contain information about noise
 2787 or gamma rates, cluster size and multiplicity, and about level 0 reconstruction of the detector effi-
 2788 ciency, muon cluster size and multiplicity. Details on the computation and file writing are respec-
 2789 tively given in Sources Codes B.19 and B.20.

2790 **Noise/gamma background variables** are computed and written in the output file for each detector
 2791 partitions. A detector average of the hit and cluster rate is also provided, as shown through Sources
 2792 Code B.19. The variables that are written for each partition are:

- 2793 • The mean partition hit rate per unit area, `MeanPartRate`, that is extracted from the histogram
 2794 `StripNoiseProfile_H` as the mean value along the y-axis, as described in section B.6.4.3. No
 2795 error is recorded for the hit rate as this is considered a single measurement. No statistical error
 2796 can be associated to it and the systematics are unknown.
- 2797 • The mean cluster size, `cSizePart`, is extracted from the histogram `NoiseCSize_H` and it's
 2798 statistical error, `cSizePartErr`, is taken to be 2σ of the total distribution.
- 2799 • The mean cluster multiplicity per trigger, `cMultPart`, is extracted from the histogram `NoiseCMult_H`
 2800 and it's statistical error, `cMultPartErr`, is taken to be 2σ of the total distribution. It is impor-
 2801 tant to point to the fact that this variable gives an information that is dependent on the buffer
 2802 window width used for each trigger for the calculation.
- 2803 • The mean cluster rate per unit area, `ClustPartRate`, is defined as the mean hit rate normalised

2804 to the mean cluster size and it's statistical error, `ClustPartRateErr`, is then obtained using the
 2805 relative statistical error on the mean cluster size.

```

for (UInt tr = 0; tr < GIFInfra->GetNTrolleys(); tr++) {
  UInt T = GIFInfra->GetTrolleyID(tr);

  for (UInt sl = 0; sl < GIFInfra->GetNSlots(tr); sl++) {
    UInt S = GIFInfra->GetSlotID(tr,sl) - 1;

    float MeanNoiseRate = 0.;
    float ClusterRate = 0.;
    float ClusterSDev = 0.;

    for (UInt p = 0; p < GIFInfra->GetNPartitions(tr,sl); p++) {
      float MeanPartRate = GetTH1Mean(StripNoiseProfile_H.rpc[T][S][p]);
      float cSizePart = NoiseCSIZE_H.rpc[T][S][p]->GetMean();
      float cSizePartErr = (NoiseCSIZE_H.rpc[T][S][p]->GetEntries()==0)
        ? 0.
        : 2*NoiseCSIZE_H.rpc[T][S][p]->GetStdDev() /
          sqrt(NoiseCSIZE_H.rpc[T][S][p]->GetEntries());
      float cMultPart = NoiseCMult_H.rpc[T][S][p]->GetMean();
      float cMultPartErr = (NoiseCMult_H.rpc[T][S][p]->GetEntries()==0)
        ? 0.
        : 2*NoiseCMult_H.rpc[T][S][p]->GetStdDev() /
          sqrt(NoiseCMult_H.rpc[T][S][p]->GetEntries());
      float ClustPartRate = (cSizePart==0) ? 0.
        : MeanPartRate/cSizePart;
      float ClustPartRateErr = (cSizePart==0) ? 0.
        : ClustPartRate * cSizePartErr/cSizePart;

      outputRateCSV << MeanPartRate << '\t'
        << cSizePart << '\t' << cSizePartErr << '\t'
        << cMultPart << '\t' << cMultPartErr << '\t'
        << ClustPartRate << '\t' << ClustPartRateErr << '\t';

      RPCarea += stripArea * nStripsPart;
      MeanNoiseRate += MeanPartRate * stripArea * nStripsPart;
      ClusterRate += ClustPartRate * stripArea * nStripsPart;
      ClusterSDev += (cSizePart==0)
        ? 0.
        : ClusterRate*cSizePartErr/cSizePart;
    }

    MeanNoiseRate /= RPCarea;
    ClusterRate /= RPCarea;
    ClusterSDev /= RPCarea;

    outputRateCSV << MeanNoiseRate << '\t'
      << ClusterRate << '\t' << ClusterSDev << '\t';
  }
}

```

Source Code B.19: Description of rate result calculation and writing into the CSV output `Offline-Rate.csv`. Are saved into the file for each detector, the mean partition rate, cluster size and cluster mutiplicity, along with their errors, for each partition and as well as a detector average.

2808 **Muon performance variables** are computed and written in the output file for each detector parti-
 2809 tions as shown through Sources Code B.20. The variables that are written for each partition are:

2810 ● The muon efficiency, `eff`, extracted from the histogram `Efficiency0_H`. It is reminded that
2811 this offline tool doesn't include any tracking algorithm to identify muons from the beam and
2812 only relies on the hits arriving in the time window corresponding to the beam time. The con-
2813 tent of the efficiency histogram is thus biased by the noise/gamma background contribution
2814 into this window and is thus corrected by estimating the muon data content in the peak re-
2815 gion knowing the noise/gamma content in the rate calculation region. Both time windows
2816 being different, the choice was made to normalise the noise/gamma background calculation
2817 window to it's equivalent beam window in order to have comparable values using the variable
2818 `windowRatio`. Finally, to estimate the data ratio in the peak region, the variable `DataRatio`
2819 is defined as the ratio in between the estimated mean cluster multiplicity of the muons in the
2820 peak region, `MuonCM`, and of the total mean cluster multiplicity in the peak region, `PeakCM`.
2821 `MuonCM` is itself defined as the difference in between the total mean cluster multiplicity in the
2822 peak region and the normalised mean noise/gamma cluster multiplicity calculated outside of
2823 the peak region. The statistical error related to the efficiency, `eff_err`, is computed using a
2824 binomial distribution, as the efficiency measure the probability of "success" and "failure" to
2825 detect muons.

2826 ● The mean muon cluster size, `MuonCS`, is calculated using the total mean cluster size and multi-
2827 plicity in the peak region, respectively extracted from histograms `MuonCSize_H` and `MuonCMult_H`,
2828 the noise/gamma background mean cluster size and normalised multiplicity, extracted from
2829 `NoiseCSize_H` and `NoiseCMult_H`, and of the estimated muon cluster multiplicity `MuonCM` pre-
2830 viously explicated. The associated statistical error, `MuonCM_err`, is calculated using the propa-
2831 gation of errors of the mentioned variables.

2832 ● The mean muon cluster multiplicity in the peak region, `MuonCM`, explicated above whose sta-
2833 tistical error, `MuonCM_err`, is the sum of statistical error associated to the total mean clus-
2834 ter multiplicity in the peak reagion, `PeakCM_err`, and of the mean noise/gamma cluster size,
2835 `NoiseCM_err`.

2836 In addition to these 2 CSV files, the histograms are saved in ROOT file `Scan00XXXX_HVY_Offline.root`
2837 as explained in section B.2.1.1.

2838

```

for (UInt tr = 0; tr < GIFInfra->GetNTrolleys(); tr++) {
    UInt T = GIFInfra->GetTrolleyID(tr);
    for (UInt sl = 0; sl < GIFInfra->GetNSlots(tr); sl++) {
        UInt S = GIFInfra->GetSlotID(tr,sl) - 1;
        for (UInt p = 0; p < GIFInfra->GetNPartitions(tr,sl); p++) {
            float noiseWindow =
                BMTDCWINDOW - TIMEREJECT - 2*PeakWidth.rpc[T][S][p];
            float peakWindow = 2*PeakWidth.rpc[T][S][p];
            float windowRatio = peakWindow/noiseWindow;

            float PeakCM = MuonCMult_H.rpc[T][S][p]->GetMean();
            float PeakCS = MuonCSize_H.rpc[T][S][p]->GetMean();
            float NoiseCM = NoiseCMult_H.rpc[T][S][p]->GetMean() *windowRatio;
            float NoiseCS = NoiseCSize_H.rpc[T][S][p]->GetMean();
            float MuonCM = (PeakCM<NoiseCM) ? 0. : PeakCM-NoiseCM;
            float MuonCS = (MuonCM==0 || PeakCM*PeakCS<NoiseCM*NoiseCS)
                ? 0.
                : (PeakCM*PeakCS-NoiseCM*NoiseCS) / MuonCM;
            float PeakCM_err = (MuonCMult_H.rpc[T][S][p]->GetEntries()==0.)
                ? 0.
                : 2*MuonCMult_H.rpc[T][S][p]->GetStdDev() /
                    sqrt(MuonCMult_H.rpc[T][S][p]->GetEntries());
            float PeakCS_err = (MuonCSize_H.rpc[T][S][p]->GetEntries()==0.)
                ? 0.
                : 2*MuonCSize_H.rpc[T][S][p]->GetStdDev() /
                    sqrt(MuonCSize_H.rpc[T][S][p]->GetEntries());
            float NoiseCM_err = (NoiseCMult_H.rpc[T][S][p]->GetEntries()==0.)
                ? 0.
                : windowRatio*2*NoiseCMult_H.rpc[T][S][p]->GetStdDev() /
                    sqrt(NoiseCMult_H.rpc[T][S][p]->GetEntries());
            float NoiseCS_err = (NoiseCSize_H.rpc[T][S][p]->GetEntries()==0.)
                ? 0.
                : 2*NoiseCSize_H.rpc[T][S][p]->GetStdDev() /
                    sqrt(NoiseCSize_H.rpc[T][S][p]->GetEntries());
            float MuonCM_err = (MuonCM==0) ? 0. : PeakCM_err+NoiseCM_err;
            float MuonCS_err = (MuonCS==0 || MuonCM==0) ? 0.
                : (PeakCS*PeakCM_err + PeakCM*PeakCS_err +
                    NoiseCS*NoiseCM_err + NoiseCM*NoiseCS_err +
                    MuonCS*MuonCM_err) / MuonCM;

            float DataRatio = MuonCM/PeakCM;
            float DataRatio_err = (MuonCM==0) ? 0.
                : DataRatio*(MuonCM_err/MuonCM + PeakCM_err/PeakCM);
            float eff = DataRatio*Efficiency0_H.rpc[T][S][p]->GetMean();
            float eff_err = DataRatio*2*Efficiency0_H.rpc[T][S][p]->GetStdDev() /
                sqrt(Efficiency0_H.rpc[T][S][p]->GetEntries()) +
                Efficiency0_H.rpc[T][S][p]->GetMean()*DataRatio_err;

            outputEffCSV << eff << '\t' << eff_err << '\t'
                << MuonCS << '\t' << MuonCS_err << '\t'
                << MuonCM << '\t' << MuonCM_err << '\t';
        }
    }
}

```

2839

Source Code B.20: Description of efficiency result calculation and writing into the CSV output Offline-L0-EffCl.csv. Are saved into the file for each detector, the efficiency, corrected taking into account the background in the peak window of the time profile, muon cluster size and muon cluster multiplicity, along with their errors, for each partition and as well as a detector average.

2840

B.7 Current data Analysis

Detectors under test at GIF++ are connected both to a CAEN HV power supply and to a CAEN ADC that reads the currents inside of the RPC gaps bypassing the supply cable. During data taking, the webDCS records into a ROOT file called `Scan00XXXX_HVY_CAEN.root` histograms with the monitored parameters of both CAEN devices. Are recorded for each RPC channels (in most cases, a channel corresponds to an RPC gap):

- the effective voltage, HV_{eff} , set by the webDCS using the PT correction on the CAEN power supply,
- the applied voltage, HV_{app} , monitored by the CAEN power supply, and the statistical error related to the variations of this value through time to follow the variation of the environmental parameters defined as the RMS of the histogram divided by the square root of the number of recorded points,
- the monitored current, I_{mon} , monitored by the CAEN power supply, and the statistical error related to the variations of this value through time to follow the variation of the environmental parameters defined as the RMS of the histogram divided by the square root of the number of recorded points,
- the corresponding current density, J_{mon} , defined as the monitored current per unit area, $J_{mon} = I_{mon}/A$, where A is the active area of the corresponding gap,
- the ADC current, I_{ADC} , recorded through the CAEN ADC module that monitors the dark current in the gap itself. First of all, the resolution of such a module is better than that of CAEN power supplies and moreover, the current is not read-out through the HV supply line but directly at the chamber level giving the real current inside of the detector. The statistical error is defined as the RMS of the histogram distribution divided by the square root of the number of recorded points.

Once extracted through a loop over the element of GIF++ infrastructure via the C++ macro `GetCurrent()`, these parameters, organised in 9 columns per detector HV supply line, are written in the output CSV file `Offline-Current.csv`. The macro can be found in the file `Current.cc`.

References

- [1] T. Massam et al. “Experimental observation of antideuteron production”. In: *Il Nuovo Cimento A* 63 (1965), pp. 10–14.
- [2] UA1 Collaboration. “Experimental observation of isolated large transverse energy electrons with associated missing energy at $s = 540 \text{ GeV}$ ”. In: *Physics Letters B* 122 (1983), pp. 103–116.
- [3] UA2 Collaboration. “Observation of single isolated electrons of high transverse momentum in events with missing transverse energy at the CERN pp collider”. In: *Physics Letters B* 122 (1983), pp. 476–485.
- [4] UA1 Collaboration. “Experimental observation of lepton pairs of invariant mass around $95 \text{ GeV}/c^2$ at the CERN SPS collider”. In: *Physics Letters B* 126 (1983), pp. 398–410.
- [5] UA2 Collaboration. “Evidence for $Z_0 \rightarrow e^+e^-$ at the CERN pp collider”. In: *Physics Letters B* 129 (1983), pp. 130–140.
- [6] ALEPH Collaboration. “Determination of the number of light neutrino species”. In: *Physics Letters B* 231 (1989), pp. 519–529.
- [7] CERN, ed. (1985).
- [8] CERN, ed. (1986).
- [9] CERN, ed. (1994).
- [10] CERN, ed. (1998).
- [11] CERN, ed. (1999).
- [12] CERN. Geneva. LHC Experiments Committee. *Letter of Intent for A Large Ion Collider Experiment [ALICE]*, note = CERN-LHCC-93-016. Tech. rep. ALICE Collaboration, 1993.
- [13] CERN. Geneva. LHC Experiments Committee. *ATLAS : technical proposal for a general-purpose pp experiment at the Large Hadron Collider at CERN*, note = CERN-LHCC-94-43. Tech. rep. ATLAS Collaboration, 1994.
- [14] CERN. Geneva. LHC Experiments Committee. *CMS : letter of intent by the CMS Collaboration for a general purpose detector at LHC*, note = CERN-LHCC-92-003. Tech. rep. CMS Collaboration, 1992.
- [15] CERN. Geneva. LHC Experiments Committee. *LHCb : letter of intent*. Tech. rep. CERN-LHCC-95-5. LHCb Collaboration, 1995.
- [16] L. Evans and P. Bryant. “LHC Machine”. In: *JINST* 3 (2008). S08001.
- [17] CMS Collaboration ATLAS Collaboration. “Combined Measurement of the Higgs Boson Mass in pp Collisions at $\sqrt{s} = 7$ and 8 TeV with the ATLAS and CMS Experiments”. In: *Physical Review Letters* 114 (2015). 191803.
- [18] LHCb Collaboration. “Observation of $J/\psi p$ Resonances Consistent with Pentaquark States in $\Lambda_b^0 \rightarrow J/\psi K^- p$ Decays”. In: *Physical Review Letters* 115 (2015). 072001.

- 2904 [19] LHCb Collaboration. “Observation of $J/\psi\phi$ Structures Consistent with Exotic States from
2905 Amplitude Analysis of $B^+ \rightarrow J/\psi\phi K^+$ Decays”. In: *Physical Review Letters* 118 (2017).
2906 022003.
- 2907 [20] CERN. Geneva. *High-Luminosity Large Hadron Collider (HL-LHC) Technical Design Re-*
2908 *port V. 0.1*. Tech. rep. CERN-2017-007-M. 2017.
- 2909 [21] CERN. Geneva. LHC Experiments Committee. *The CMS muon project : Technical Design*
2910 *Report*. Tech. rep. CERN-LHCC-97-032. CMS Collaboration, 1997.
- 2911 [22] CERN. Geneva. LHC Experiments Committee. *The Phase-2 Upgrade of the CMS Muon*
2912 *Detectors*. Tech. rep. CERN-LHCC-2017-012, CMS-TDR-016. CMS Collaboration, 2017.
- 2913 [23] CERN. Geneva. LHC Experiments Committee. *CMS, the Compact Muon Solenoid : technical*
2914 *proposal*. Tech. rep. CERN-LHCC-94-38. CMS Collaboration, 1994.
- 2915 [24] R. Santonico and R. Cardarelli. “Development of resistive plate counters”. In: *Nucl. Instr.*
2916 *Meth. Phys. Res.* 187 (1981), pp. 377–380.
- 2917 [25] Yu.N. Pestov and G.V. Fedotovich. *A picosecond time-of-flight spectrometer for the VEPP-2M*
2918 *based on local-discharge spark counter*. Tech. rep. SLAC-TRANS-0184. SLAC, 1978.
- 2919 [26] W.W. Ash, ed. *Spark Counter With A Localized Discharge*. Vol. SLAC-R-250. 1982, pp. 127–
2920 131.
- 2921 [27] I. Crotty et al. “The non-spark mode and high rate operation of resistive parallel plate cham-
2922 bers”. In: *NIMA* 337 (1993), pp. 370–381.
- 2923 [28] I. Crotty et al. “Further studies of avalanche mode operation of resistive parallel plate cham-
2924 bers”. In: *NIMA* 346 (1994), pp. 107–113.
- 2925 [29] R. Cardarelli et al. “Avalanche and streamer mode operation of resistive plate chambers”. In:
2926 *NIMA* 382 (1996), pp. 470–474.
- 2927 [30] E. Cerron Zeballos et al. “A new type of resistive plate chamber: The multigap RPC”. In:
2928 *NIMA* 374 (1996), pp. 132–135.
- 2929 [31] M.C.S. Williams. “The development of the multigap resistive plate chamber”. In: *Nucl. Phys.*
2930 *B* 61 (1998), pp. 250–257.
- 2931 [32] H. Czyrkowski et al. “New developments on resistive plate chambers for high rate operation”.
2932 In: *NIMA* 419 (1998), pp. 490–496.
- 2933 [33] P. Camarri et al. “Streamer suppression with SF6 in RPCs operated in avalanche mode”. In:
2934 *NIMA* 414 (1998), pp. 317–324.
- 2935 [34] E. Cerron Zeballos et al. “Effect of adding SF6 to the gas mixture in a multigap resistive plate
2936 chamber”. In: *NIMA* 419 (1998), pp. 475–478.
- 2937 [35] CERN. Geneva. LHC Experiments Committee. *ATLAS muon spectrometer: Technical design*
2938 *report*. Tech. rep. CERN-LHCC-97-22. ATLAS Collaboration, 1997.
- 2939 [36] CERN. Geneva. LHC Experiments Committee. *ALICE Time-Of-Flight system (TOF) : Tech-*
2940 *nical Design Report*. Tech. rep. CERN-LHCC-2000-012. ALICE Collaboration, 2000.
- 2941 [37] The CALICE collaboration. “First results of the CALICE SDHCAL technological proto-
2942 type”. In: *JINST* 11 (2016).
- 2943 [38] PoS, ed. *Density Imaging of Volcanoes with Atmospheric Muons using GRPCs*. International
2944 Europhysics Conference on High Energy Physics - HEP 2011. 2011.
- 2945 [39] C. Lippmann. “Detector Physics of Resistive Plate Chambers”. PhD thesis. Johann Wolfgang
2946 Goethe-Universität, 2003.

BIBLIOGRAPHY

- [40] M. Abbrescia et al. “Properties of C₂H₂F₄-based gas mixture for avalanche mode operation of resistive plate chambers”. In: *NIMA* 398 (1997), pp. 173–179.
- [41] G. Battistoni et al. “Sensitivity of streamer mode to single ionization electrons”. In: *NIMA* 235 (1985), pp. 91–97.
- [42] W. Riegler. “Induced signals in resistive plate chambers”. In: *NIMA* 491 (2002), pp. 258–271.
- [43] E. Cerron Zeballos et al. “A comparison of the wide gap and narrow gap resistive plate chamber”. In: *NIMA* 373 (1996), pp. 35–42.
- [44] M. Abbrescia et al. “Cosmic ray tests of double-gap resistive plate chambers for the CMS experiment”. In: *NIMA* 550 (2005), pp. 116–126.
- [45] ALICE Collaboration. “A study of the multigap RPC at the gamma irradiation facility at CERN”. In: *NIMA* 490 (2002), pp. 58–70.
- [46] B. Bonner et al. “A multigap resistive plate chamber prototype for time-of-flight for the STAR experiment at RHIC”. In: *NIMA* 478 (2002), pp. 176–179.
- [47] S. Yang et al. “Test of high time resolution MRPC with different readout modes for the BESIII upgrade”. In: *NIMA* 763 (2014), pp. 190–196.
- [48] A. Akindinov et al. “RPC with low-resistive phosphate glass electrodes as a candidate for the CBM TOF”. In: *NIMA* 572 (2007), pp. 676–681.
- [49] JINST, ed. *Development of the MRPC for the TOF system of the MultiPurpose Detector*. RPC2016: XII Workshop on Resistive Plate Chambers and Related Detectors. 2016.
- [50] M.C.S. Williams. “Particle identification using time of flight”. In: *Journal of Physics G* 39 (2012).
- [51] A. Alici et al. “Aging and rate effects of the Multigap RPC studied at the Gamma Irradiation Facility at CERN”. In: *NIMA* 579 (2007), pp. 979–988.
- [52] M. Abbrescia et al. “The simulation of resistive plate chambers in avalanche mode: charge spectra and efficiency”. In: *NIMA* 431 (1999), pp. 413–427.
- [53] M. Abbrescia et al. “Study of long-term performance of CMS RPC under irradiation at the CERN GIF”. In: *NIMA* 533 (2004), pp. 102–106.
- [54] H.C. Kim et al. “Quantitative aging study with intense irradiation tests for the CMS forward RPCs”. In: *NIMA* 602 (2009), pp. 771–774.
- [55] S. Agosteo et al. “A facility for the test of large-area muon chambers at high rates”. In: *NIMA* 452 (2000), pp. 94–104.
- [56] PoS, ed. *CERN GIF ++ : A new irradiation facility to test large-area particle detectors for the high-luminosity LHC program*. Vol. TIPP2014. 2014, pp. 102–109.
- [57] A. Fagot. *GIF++ DAQ v4.0*. 2017. URL: https://github.com/afagot/GIF_DAQ.
- [58] CAEN. *Mod. V1190-VX1190 A/B, 128/64 Ch Multihit TDC*. 14th ed. 2016.
- [59] CAEN. *Mod. V1718 VME USB Bridge*. 9th ed. 2009.
- [60] W-Ie-Ne-R. *VME 6021-23 VXI*. 5th ed. 2016.
- [61] Wikipedia. *INI file*. 2017. URL: https://en.wikipedia.org/wiki/INI_file.
- [62] S. Carrillo A. Fagot. *GIF++ Offline Analysis v6*. 2017. URL: https://github.com/afagot/GIF_OfflineAnalysis.